Characterization of Shrinkage Porosity and Fatigue Properties of Cast CA-6NM Low Carbon Martensitic Stainless Steels

by

Shilan MEIMANDI

THESIS PRESENTED TO ÉCOLE DE TECHNOLOGIE SUPÉRIEURE IN
PARTIAL FULFILLMENT FOR THE DEGREE OF
DOCTOR OF PHILOSOPHY
Ph. D.

MONTREAL, DECEMBER 16TH, 2021

ÉCOLE DE TECHNOLOGIE SUPÉRIEURE
UNIVERSITÉ DU QUÉBEC

BOARD OF EXAMINERS

THIS THESIS HAS BEEN EVALUATED

BY THE FOLLOWING BOARD OF EXAMINERS

Mr. Martin Viens, Thesis Supervisor
Departement of Mechanical Engineering, École de technologie supérieure

Mr. Lotfi Guizani, Chair, Board of Examiners
Departement of Construction Enginering, École de technologie supérieure

Mr. Henri Champliaud, Member of the jury
Departement of Mechanical Engineering, École de technologie supérieure

Mr. Martin D. Pugh, External Evaluator
Department of Mechanical, Industrial and Aerospace Engineering, Concordia university

THIS THESIS WAS PRESENTED AND DEFENDED

IN THE PRESENCE OF A BOARD OF EXAMINERS AND THE PUBLIC

NOVEMBER 4TH, 2021

AT ÉCOLE DE TECHNOLOGIE SUPÉRIEURE

ACKNOWLEDGMENT

This project has been made possible by the support, help and facilities from the Institut de recherche d’Hydro-Québec (IREQ) and Alstom Canada Inc. The research was accomplished at the Departement of Mechanical Engineering at École de technologie supérieure (ÉTS).

First and foremost, I would like to express my deep sense of gratitude to my supervisor, Professor Martin Viens whose overall sights, fruitful scientific discussions, guidance, moral support and encouragement have been invaluable in this study. Without his help, I would never have been able to give my best.

In addition, I am obliged to express my sincere thanks to Dr. Denis Thibault (IREQ) for being a great source of support and taking a keen interest in my research. I learned a lot from him.

Thanks should also be given to Dr. Demartonne Ramos Franca (ÉTS) for his helpful discussions and valuable revisions of my article. The useful counsel by Professor Antoine Tahan (ÉTS) is gratefully appreciated as well.

Furthermore, the precious technical assistance by Etienne Dallaire (IREQ) is thankfully acknowledged. Also, I would appreciate Mr. Benoit Papillon and Mr. Michel Sabourin from Alstom for their helpful counsel.

This project was financially supported by Alstom Canada; Hydro-Québec; Mitacs; Consortium de recherche en fabrication et réparation des roues d’eau (CReFaRRE); and the Natural Sciences and Engineering Research Council of Canada (NSERC).

CARACTÉRISATION DE LA POROSITÉ PAR RETRAIT ET DES PROPRIÉTÉS EN FATIGUE DES ACIERS INOXYDABLES MARTENSITIQUES À FAIBLE TENEUR EN CARBONE

Shilan MEIMANDI

RÉSUMÉ

L’acier inoxydable martensitique à faible teneur en carbone CA-6NM est utilisé pour le moulage de pales de turbines hydrauliques depuis les années 60 en raison de sa ténacité et de sa résistance mécanique, à la cavitation, à l’érosion et à la corrosion. Il est utilisé pour supporter grandes charges opératoires cycliques sur une longue durée de vie. C'est un revenu approprié qui donne à ces aciers leur microstructure idéale à savoir une matrice martensitique dans laquelle des ilots d'austénite sont dispersés. Cependant, ces pièces moulées contiennent plusieurs types de défauts qui peuvent avoir des effets néfastes sur les performances des pièces produites. Or, plusieurs aspects de la caractérisation des défauts de coulée dans ces aciers n’ont pas fait l’objet d’études approfondies. Les principaux objectifs des travaux décrits dans le présent document comprennent donc la caractérisation des défauts de coulée dans l'acier CA-6NM.

Dans le premier article, la relation entre la cartographie radiographique et la morphologie réelle des macro-défauts, classés selon différents niveaux de gravité, a été étudiée de façon destructive à l’aide de coupes transversales (tranches de salami). Cette étude démontre que la presque totalité des défauts observés consistent en des macroretassures comportant des terminaisons extrêmement effilées. La distribution de la taille de ces défauts a été mesurée grâce au paramètre géométrique de Murakami ($\sqrt{aire}$) et au diamètre de Feret. Des niveaux de gravité plus élevés ont montré des défauts avec des terminaisons plus fines et de plus grands paramètres de Murakami. Une caractérisation métallographique de la microstructure coulée a également été effectuée pour étudier la composition chimique et la microstructure autour des macro-défauts.

Dans la deuxième partie, des essais en fatigue oligocyclique (LCF) tension-tension uniaxiale ont été effectués sur des éprouvettes de fatigue moulées en CA-6NM. L’impact de la position des défauts et de leur taille (i.e., le paramètre géométrique de Murakami ($\sqrt{aire}$) sur la durée de vie des éprouvettes en fatigue a été étudié. À cette fin, un examen fractographique bidimensionnel (2D) a été effectué sur les faciès de rupture grâce à un MEB. La durée de vie en fatigue diminuait généralement lorsque la taille du défaut augmentait. Toutefois, la position du défaut était également d’une importance critique. De plus, l’évolution des défauts pendant la propagation des fissures de fatigue et la variation du facteur géométrique *Y(a)* (paramètre issu de la mécanique de la rupture élastique linéaire - LEFM) ont été étudiées.

Dans la troisième partie, une évaluation tomographique tridimensionnelle (3D) par rayons X a été effectuée avant (i.e., échantillon vierge) et après (i.e., échantillon brisé) la rupture par fatigue. Ces résultats ont été comparés à l'observation fractographique bidimensionnelle (2D) sur les faciès de rupture. L'analyse 3D a fourni la distribution des macroretassures avec précision et rigueur. Les défauts possédaient une morphologie tortueuse et complexe. Les résultats des essais en fatigue ont démontré que, dans le processus d'initiation de la fatigue, la position de la macroretassure était plus déterminante que sa taille.

Mots-clés: Turbine hydraulique, Macroretassures, Acier inoxydable martensitique moulé, Caractérisation, Coupe transversale (tranche de salami), Fractographie, Tomographie à rayons X, Fatigue.

CHARACTERIZATION OF SHRINKAGE POROSITY AND FATIGUE PROPERTIES OF CAST CA-6NM LOW CARBON MARTENSITIC STAINLESS

Shilan MEIMANDI

ABSTRACT

Cast CA-6NM low carbon martensitic stainless steel is used for hydraulic turbine runner manufacturing since the sixties of the last century owing to its high strength, toughness, cavitation-erosion resistance and corrosion to withstand high cycle loads in long lifetime operation. The ideal microstructure consists of a martensitic matrix with some dispersed austenite after appropriate tempering which gives these steels their unique properties. However, these castings contain several types of defects which may have detrimental effects on the performance of the produced parts. Several aspects of the casting defect characterization in these steels have not been extensively studied in particular. The main objectives of this investigation include the characterization of the casting defects described in the following three sections.

In the first article, the relation between radiography mapping and actual macro-defect morphologies in several severity levels was studied destructively using the "Salami" cross-sectioning to document the real shape and morphology of defects. Results of these experiments represented defects as macro-shrinkage porosities with extremely sharp endings. The distribution of porosity size was measured via Murakami's geometrical parameter ($\sqrt{area}$) and Feret's diameter. Higher severity levels of macro-shrinkage porosities demonstrated defects with sharper endings and larger Murakami's parameter. Metallographic characterization of cast microstructure was also performed to study both chemical composition and microstructure around macro-defects.

In the second part, uniaxial tension-tension low cycle fatigue testing (LCF) was conducted on the cast CA-6NM fatigue samples. The impact of defects position and sizing parameter (i.e., Murakami's geometrical parameter ($\sqrt{area}$) on the fatigue life was studied. To this end, a two-dimensional (2D) SEM fractographic examination was performed on the fracture surfaces. The fatigue life generally diminished when the defect size increased. However, the position of the defect was also of critical importance. Moreover, the evolution of the shrinkage porosities during fatigue crack propagation and variation of geometrical factor $Y(a)$ (considering linear elastic fracture mechanics (LEFM)) were investigated.

In the third part, non-destructive three-dimensional (3D) X-ray tomographic evaluation was performed before (i.e., pristine sample) and after (i.e., broken sample) fatigue failure. The results were compared with the two-dimensional (2D) fractographic observations. The 3D analysis provided the distribution of shrinkage porosities precisely and thoroughly. The defects possessed a tortuous and intricate morphology. Results after fatigue testing displayed that the position of shrinkage porosity was more effective than the size in initiating the fatigue crack.

Keywords: Hydraulic-turbine, Macro-shrinkage porosities, Cast martensitic stainless steel, Characterization, "Salami" cross-sectioning, Fractography, X-ray computed tomography, Fatigue.

TABLE OF CONTENTS

Page

LIST OF TABLES

LIST OF FIGURES

Page

LIST OF ABBREVIATIONS

2D	Two-Dimensional
3D	Three-Dimensional
AOD	Argon Oxygen Decarburization
ASM	American Society for Metals
ASTM	American Society for Testing and Materials
EDX	Energy Dispersive X-ray Spectroscopy
HCF	High cycle fatigue
IQI	Image Quality Indicators
LCF	Low Cycle Fatigue
LEFM	Linear Elastic Fracture Mechanics
MEB	Microscope électronique à balayage
NDE	Non-Destructive Evaluation
NDT	Non-Destructive Testing
PSBs	Persistent Slip Bands
POD	Probability of Detection
ROI	Region Of Interest
SEM	Scanning Electron Microscope
TEM	Transmission Electron Microscopy
XCT	X-ray Computed Tomography

LIST OF SYMBOLS

K_t	Stress concentration factor
σ_{max}	Maximum local stress
σ_n	Nominal applied stress
D	Notch length / Fatigue sample diameter
ρ	Notch radius
l	Distance from the discontinuity
K	Stress intensity factor
Y	Geometrical factor
a	Crack length
K_I	Stress intensity factor (Opening loading mode (Mode I))
θ	Crack tip angle
X, Y, Z	Axes of the coordinate system
σ_x	Transverse stress
σ_y	Longitudinal stress
σ_z	Stress along Z-axis
v	Poisson’s ratio
σ_0	Tensile yield strength
r_p	Plastic zone size
a_1	Distance between the crack tip and any of the other fatigue sample’s surfaces
ΔK	Stress intensity factor range
$\Delta\sigma$	Stress range

N	Number of fatigue cycles
C	Constant in Paris law
m	The exponent in Paris law
ΔK_{th}	Threshold stress intensity factor range
$\Delta \sigma_{fl}$	Fatigue limit
L	Feret's diameter
α	Shape parameter (3-parameter Weibull distribution & Double parameter Weibull distribution)
β	Scale parameter (3-parameter Weibull distribution & Double parameter Weibull distribution)
γ	Threshold parameter (3-parameter Weibull distribution)
μ	Location parameter (Lognormal distribution)
σ	Scale parameter (Lognormal distribution)
Φ	Laplace integral (Lognormal distribution)
N_f	Cycles to fatigue fracture

INTRODUCTION

High toughness together with excellent resistance to cavitation and erosion makes CA-6NM low carbon soft martensitic stainless steels an attractive choice for manufacturing cast hydraulic turbine runners (Iwabuchi, 1987; Thibault, Gagnon & Godin 2015; Ferreño et al., 2011; Tokuda, Kumada & Nakagawa, 1970; Iwabuchi & Sawada, 1982; Larson & Fisher R, 1979). CA-6NM has a maximum carbon content of 0.06 percent. This low carbon content results in an alloy that is easier to process in casting when compared with other martensitic stainless steels (Behal & Melilli, 1982).

Casting is used to fabricate large and heavy metal objects with an intricate shape (e.g., turbine blades) that needs high accuracy, at a relatively lower cost compared to other methods (Moore, 1981). However, casting defects are frequently the main causes of cracks when the part is put in operation and sometimes result in complete component failure. To anticipate the remaining life of hydraulic turbines and improve their performance, it is important to understand defects characteristics (i.e., type, size, morphology and positions) and later on, determine their effect on fatigue properties to establish adequate conditions for operation.

Among all types of defects, shrinkage porosity is the most common one found in this investigation. In steel casting components, shrinkage porosities are highly detrimental due to their three-dimensional (3D) complex nature. They are weakening structures by reducing the continuity of load-bearing material and raising stress concentration in the remaining material. The effect of shrinkage porosities on the reliability and fatigue performance of cast steels is of significant importance and has been pursued in some studies (Kim, Lee & Nahm, 2006; Sigl, Hardin, Stephens & Beckermann, 2004; Briggs, 1969; Briggs, 1966). However, various aspects of such investigations in cast CA-6NM martensitic stainless steels are not self-evident and well understood in detail.

In the present study, non-destructive X-ray radiography, metallography (using an optical microscope), destructive "Salami" cross-sectioning and fractography (using a scanning electron microscope (SEM)) were applied to evaluate defects in the planar sections of cast structures. However, these characterizations only provide two-dimensional (2D) information of shrinkage porosities which may underestimate their actual equivalent size and not be adequate to describe their complete tortuous morphology. Based on that, a non-destructive three-dimensional (3D) evaluation of the shrinkage porosities characteristics before (i.e., pristine sample) and after (i.e., broken sample) fatigue failure was acquired by laboratory X-ray computed tomography. This 3D porosity analysis provided complementary information alongside the interpreted analysis acquired by two-dimensional (2D) examinations mentioned above.

In short, the primary goals of this research are: (1) to study the type of defects present in the cast turbine blade made of CA-6NM martensitic stainless steel, (2) to peruse the two-dimensional (2D) and three-dimensional (3D) characterization of shrinkage porosities and investigate their discrepancies, (3) to detect the fatigue crack nucleation site(s) and discover how detrimental are the porosities to the fatigue life of the studied material, and eventually (4) to verify the main characteristics of shrinkage porosities responsible for the failure and illustrate which individual characteristics of the shrinkage porosities could be dominant for the cause of the failure.

Collecting all this detailed information might give a better understanding of the role of the shrinkage porosity in the fatigue behavior of the cast CA-6NM material.

CHAPTER 1

LITERATURE REVIEW

1.1 Francis turbine runners

Francis turbine runners (Figure 1.1) are one of the main parts of hydraulic turbines and are widely used in hydroelectric facilities. They are known to be highly efficient convertors of hydraulic energy from water flow to electrical energy. The Francis turbine runner can be manufactured of cast steel and a welded structure where the blades are joined to the crown (hub) and the cast band by welding (Huth, 2005; Kjølle, 2001).

Higher power in hydraulic turbines imposes higher mechanical and hydraulic loads on the turbine. Major stresses and vibrations provided by the aforementioned conditions could cause blade fracture due to fatigue (Flores, Urquiza & Rodríguez, 2012). Fatigue nucleation sites in turbine runners are mainly caused by cavitation, erosion, and material or manufacturing defects. Suitable properties of the material are essential to minimize the damage. Thus, turbine runners are made of specific stainless steel grades for their good corrosion-erosion resistance, high strength and high toughness (Iwabuchi & Sawada, 1982).

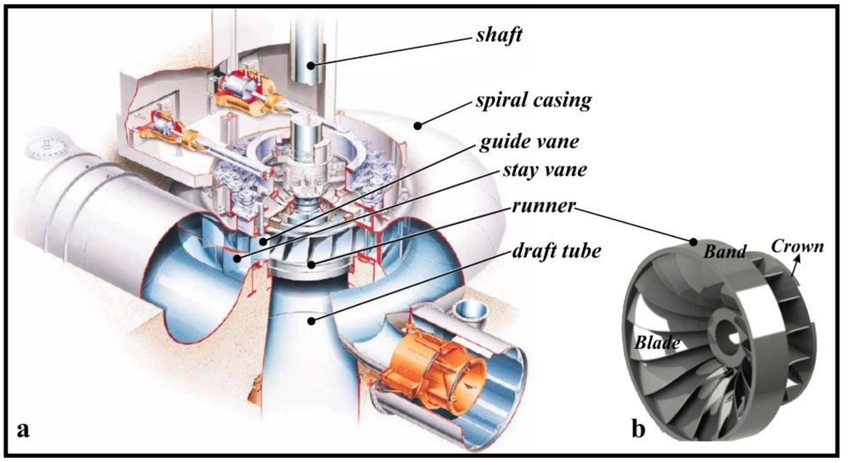

Figure 1.1 (a) Francis turbine, taken and adapted from Huth (2005, p. 3), (b) Francis turbine runner

1.2 Steels for turbine runner

In most cases, turbine runners are made of stainless steel to decrease the detriments from cavitations in high water flow velocities, erosion, and water corrosion (Kjølle, 2001). In stainless steel, increased resistance to water corrosion is given by a minimum chromium content of 10.5% - 12%. This amount of chromium results in the spontaneous formation of a thin protective oxide film on the surface called the passivation layer (Davis, 2000; Llewellyn & Hudd, 1998). The chemical composition of the alloy controls the stability of the different phases in the microstructure. Accordingly, stainless steel can be classified as martensitic, austenitic, ferritic, duplex (austenitic-ferritic), and precipitation-hardenable grades (Figure 1.2) (Davis, 2000).

Besides the main influence of chromium, there are additional alloying elements that improve other properties in steel. These alloying elements can be categorized into two groups. The first group promotes ferrite formation (e.g., chromium) while the second group involves austenite stabilizers. Some of these alloying elements are described in Table 1.1 (Outokumpu Stainless AB, 2013):

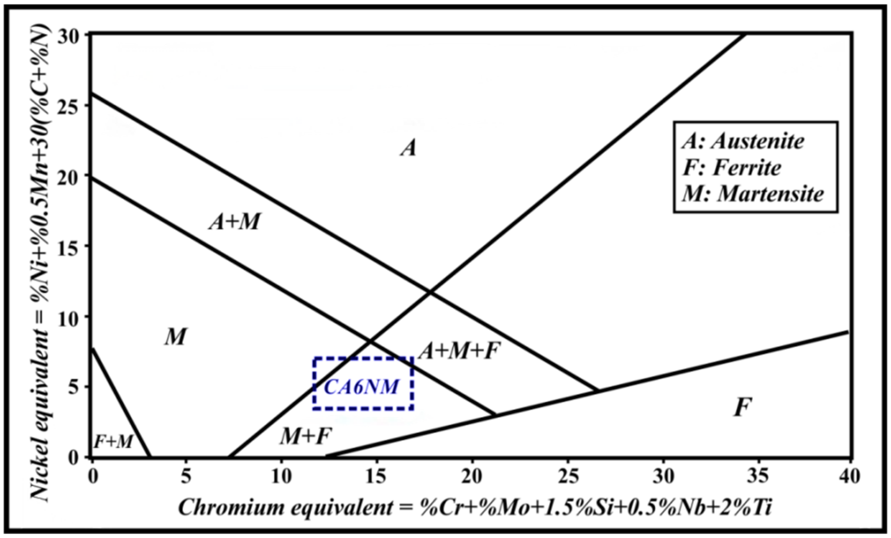

Figure 1.2 Stainless steel Schaeffler diagram showing the region corresponding to the CA-6NM stainless steel, Taken and adapted from Ferreño et al. (2011, p. 263)

Table 1.1 Austenite and ferrite stabilizers in stainless steels

Element	Stabilized phase	Properties
Nickel	austenite	• promotes ductility and toughness • with a reduced amount of carbon, improves weldability • forms intermetallic compounds and increases strength
Manganese	austenite	• increases hardenability
Carbon	austenite	• enhances the mechanical strength • with chromium forms chromium carbides at grain boundaries and decreases corrosion resistance
Molybdenum	ferrite	• increases corrosion resistance • improves the hardness at high tempering temperatures
Silicon	ferrite	• increases strength • improves resistance to oxidation

Austenitic stainless steel with excellent corrosion resistance cannot be used for all hydraulic runners because of their higher cost. The plain 13% chromium steel comprises good corrosion resistance and excellent toughness but poor weldability. However, low carbon soft martensitic stainless steels contain an increased amount of nickel (between 3 and 6%) (Iwabuchi, 2003; Iwabuchi & Sawada, 1982) that results in a good combination of strength, ductility, and toughness thanks to the formation of fine precipitates (carbides) and dispersed austenite (Song, Ping, Yin, Li & Li, 2010). Hence, low carbon soft martensitic stainless steels such as CA-6NM (13%Cr-4%Ni) are usually the favoured material for cast hydraulic turbine runners.

1.3 CA-6NM martensitic stainless steel

CA-6NM stainless steels are used in hydraulic turbine runners for their good corrosion resistance, weldability, together with high strength and toughness properties which are important for equipment operating in a water environment with high-stress fluctuations (Bilmes, Solari & Llorente, 2001; Iwabuchi, 2003; Tabatabae, Ashrafizadeh & Hassanli, 2011). The chemical composition and mechanical properties of CA-6NM stainless steel at room temperature are shown in Table 1.2 (ASTM-A743/A743M; ASTM-A487/A487M) and Table 1.3 respectively (ASTM-A487/A487M; Steel Casting Handbook, 2004). Representative properties in Table 1.3 demonstrate tensile properties for the standard cast CA-6NM martensitic stainless steel that is air-cooled from > 1900 °F (~ 1038 °C) and tempered in the range of 1100 °F (~ 594 °C) to 1150 °F (~ 621 °C) (Steel Casting Handbook, 2004).

Table 1.2 CA-6NM stainless steel chemical composition (wt. %)
(ASTM-A743/A743M; ASTM-A487/A487M)

Composition, %	**C**	**Cr**	**Ni**	**Mo**	**Mn**	**Si**	**P**	**S**	**Fe**
Minimum		11.5	3.5	0.4					Bal.
Maximum	0.06	14	4.5	1	1	1	0.04	0.03	Bal.

Table 1.3 Mechanical properties of CA-6NM stainless steel
(ASTM-A487/A487M; Steel Casting Handbook, 2004)

Properties	**Representative**	**Required (min)**
Tensile strength (MPa)	~ 827	~ 760
Yield strength at 0.2% (MPa)	~ 688	~ 550
Elongation (%)	24	15
Reduction of Area (%)	60	35

Referring to the Schaeffler diagram (cf. Figure 1.2), CA-6NM has a martensitic-ferritic microstructure. CA-6NM is generally used in the quenched and tempered state where the microstructure is mostly martensite which is the major strengthening component (Ferreño et al., 2011). In this regard, steel is hardened by heating to 1050 °C (austenitizing stage) followed by air cooling (95 °C or lower) or oil quenching. After the complete transformation of austenite to martensite, the alloy is tempered in the range of 565 °C to 620 °C followed by furnace-cooling. Figure 1.3 illustrates the heat treatment steps performed on the cast CA-6NM material which is the subject of the current research.

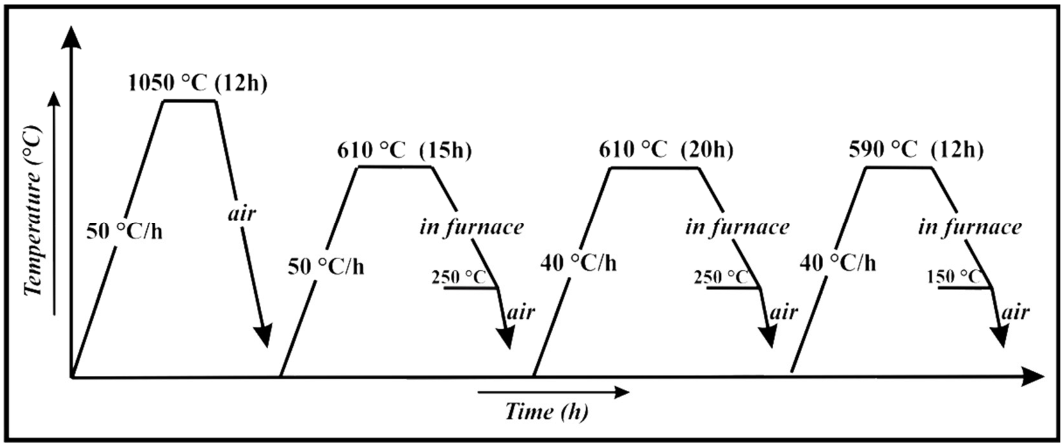

Figure 1.3 Thermal cycles of normalizing and tempering applied to the CA-6NM cast blade

Although the martensitic phase is the main component, small islands of delta ferrite and retained/reversed austenite can also be present in the quenched and tempered CA-6NM microstructure (Song et al., 2010; Bilmes et al., 2001). The presence of dispersed untransformed austenite in the microstructure after tempering provides the high toughness of the CA-6NM stainless steel (Bilmes et al., 2001).

Figure 1.4(a) illustrates the metallographic characterization of the normalized and tempered cast CA-6NM studied in this research. The microstructure consists of lath martensite with small islands of ferrite. Because the lamellae of austenite are too thin to be observed by optical microscopy (Thibault et al., 2011), they do not appear in Figure 1.4(a). In martensitic stainless steels, austenite commonly locates along the martensite interlath boundaries and prior austenite grain boundaries. Figure 1.4(b) exhibits an elongated shape of reversed austenite grown along the martensite interlath boundary in Fe–13%Cr–4%Ni–Mo martensitic stainless steel which is tempered at (680 + 600) °C for 4 h (Song et al., 2010).

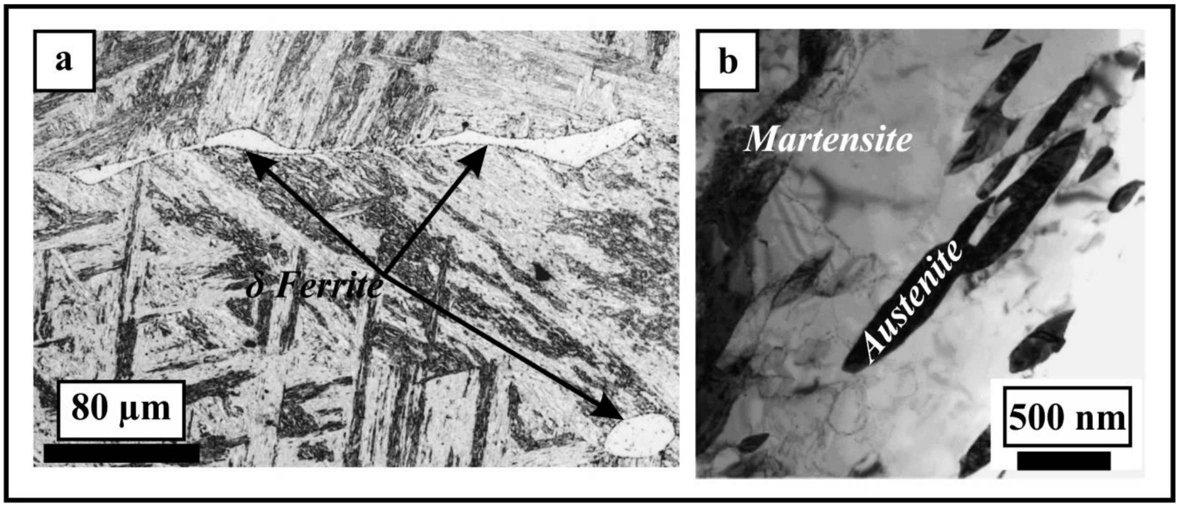

Figure 1.4 (a) Normalized and tempered cast CA-6NM microstructure, (b) Bright-field TEM images showing elongated austenite along martensitic interlath boundaries, Taken and adapted from Song et al. (2010, p. 616)

Delta ferrite can be the result of higher Chromium or lower Nickel content, as well as incorrect heat treatments where overheating increases the amount of delta ferrite. The presence of delta ferrite deteriorates the toughness properties and decreases crack nucleation and crack propagation energies as delta ferrite is not cohesively bounded to the surrounding matrix (Wang, Lu, Xiao, Li & Li, 2010).

1.4 Casting process

Turbine blades are often made by the casting process. In casting, molten metal fills a mould cavity and solidifies into a near-net shape. Hence, casting is used to fabricate large and heavy metal objects with an intricate shape that needs high accuracy, at a relatively lower cost compared to other manufacturing processes (Moore, 1981). Also, to obtain the final shape, casting components require fewer additional steps (e.g., machining, welding) that can introduce undesirable changes and discontinuities into the material. However, the complicated shape means sudden variation in dimensions, which results in a non-uniform flow of melt and cooling rate (Björkblad, 2008). Under such conditions, the shrinkage cavities and pores are easy to form (Dabayeh, 1998). Therefore, despite the aforementioned advantages, casting has a drawback which is the presence of different types of defects known to be detrimental to the mechanical properties and more importantly the fatigue resistance.

1.5 Casting defects

Cast materials often contain defects owing to a variety of causes such as improper control of solidification parameters, uneven flow of the melt, deficient melt, or metal contamination (Stefanescu, 2009). Casting defects are important to casting engineering and also to subsequent manufacturing processes and evaluation. Defects cause stress concentration in micro as well as in macro-scale that controls fatigue characteristics of cast components. Hence, they are responsible for imperfections in the final manufactured products and may be the cause of failures.

Generally, two different classifications exist for casting defects. Depending on the position, defects would be classified as surface defects (e.g., a hot tear, cold shut, blow, scar, and blister) and internal defects (e.g., inclusion entrapment, internal shrinkage cavity, internal gas porosity, and segregation) (Campbell, 2011; Stefanescu, 2009). Surface defects can be detected by the dye-penetrant method or even by naked eyes, and easily reworked by some industrial methods such as grinding and welding. However, casting defects such as internal shrinkage porosities cannot be revealed and eliminated easily. Therefore, their influence on the mechanical performance of castings should be considered up-front in the design of the cast products and shall be assessed upon the manufacturing of the castings (Cheng, Hort, Kainer & Kwak, 2013). Internal defects can be detected either by radiographic (cf. section 1.6) or ultrasonic techniques.

The second classification of casting defects relies on their size and distribution: micro and macro defects. Macro defects are large enough to be perceived on non-destructive inspection records, while micro ones are not visible without magnification (Cheng et al., 2013). Some important types of casting discontinuities are described in the following sections:

- **Shrinkage porosity**

Among all types of defects, macro-shrinkage porosity is the most common one found in this investigation (Figure 1.5). Shrinkage porosities could be considered as one of the most important defects that influence the reliability and mechanical performance of cast components. They are weakening structures by reducing the continuity of load-bearing material and raising stress concentration in the remaining material. The impact of shrinkage porosities on fatigue behavior can be more severe than inclusions and oxide films (Cao et al, 2014). It has been studied that a 1% volume fraction of porosity can cause a decrease of 50% of fatigue life and 20% of fatigue limit compared with the same material with similar microstructure but without porosity (Ødegard and Pedersen, 1984).

Shrinkage porosities are the result of volumetric changes in the solidification process. They appear at the final stage of solidification due to the poor feeding of liquid metal to the casting part. At this stage, because molten metal contracts (Sigl et al., 2004) and the flow of liquid metal becomes harder (Fredriksson and Åkerlind, 2006), internal porosities might occur. Thus, the formation of shrinkage porosity can be influenced by various factors such as the solidification temperature range of the alloy (Pehlke, 1988), the flow of molten metal through the dendritic zone, etc.

According to the size classification, shrinkage porosities are categorized into macro-shrinkage porosity and micro-shrinkage porosity. Macro-shrinkage porosities are larger and more localized than micro ones. Using a proper riser and gating system can prevent or reduce this kind of shrinkage porosity.

On a much smaller scale, shrinkage can happen as micro-shrinkage porosity. During the freezing process, dendrites grow and form a crystalline network with isolated liquid pockets. This dendritic zone can prevent complete feeding from the additional liquid remaining in the risers and plays a key role in the formation of this type of shrinkage porosity (Ammar, 2006).

Figure 1.6 demonstrates the effect of shrinkage porosities on the fatigue life of cast iron. The fatigue life decreases with an increase in the shrinkage porosity area on the fracture surface (Liu, Zhai & Zhao, 2016).

The shape of the shrinkage porosities also contributes to structural weakening. They typically follow the dendrite shape and display a tortuous three-dimensional (3D) morphology with a rough and uneven surface. This complex configuration can cause more stress concentration than round pores with smooth and even surfaces and make shrinkage porosities highly detrimental to the cast structures.

The distribution of shrinkage porosities is another factor that has an impact on fatigue performance. The susceptibility of nearby defects to merge as a larger one can affect the fatigue life more than an isolated defect (cf. section 1.9.4).

Shrinkage porosities are also classified depending on their position. In this category, they are divided into surface shrinkages that are open to the surface and internal shrinkages with no contact with the casting surface. When porosities are located at or near the free surface of the specimen, their impact on mechanical performance is more severe (Dabayeh, 1998). The surface is normally suffering from stress risers such as surface roughness and residual stress induced by machining. The surface may also be subjected to oxidation and corrosive environmental effects (Schijve, 1977). All these factors plus porosities which are found on the surface act like defects and therefore fatigue cracks initiate more easily at the surface when a part is exposed to loading. In brief, all characteristics of shrinkage porosities (shape, size, position, distribution) can affect the mechanical properties of the casting.

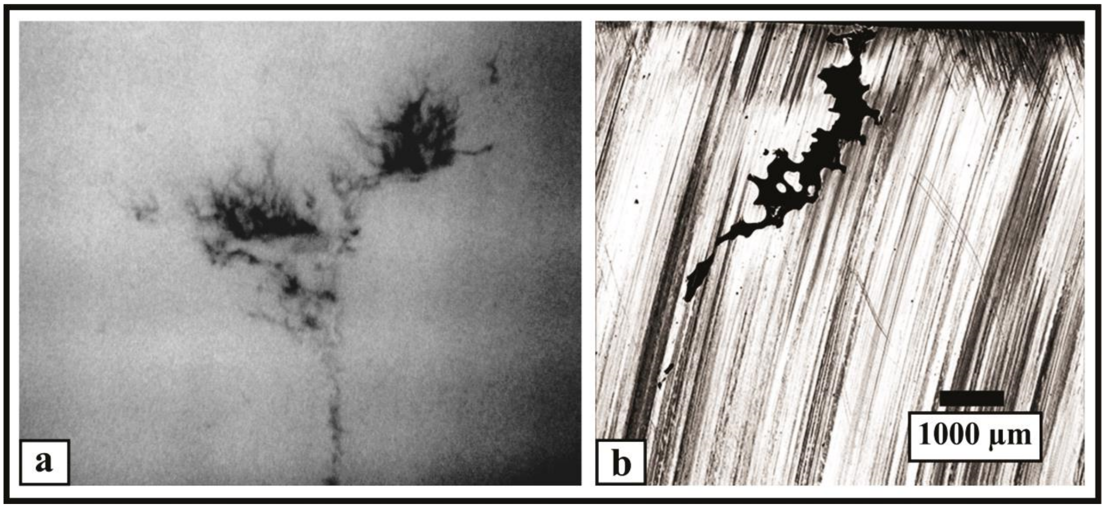

Figure 1.5 Shrinkage porosity of the studied cast CA-6NM turbine blade
(a) X-ray radiographic image, (b) optical image of a selected cross-section

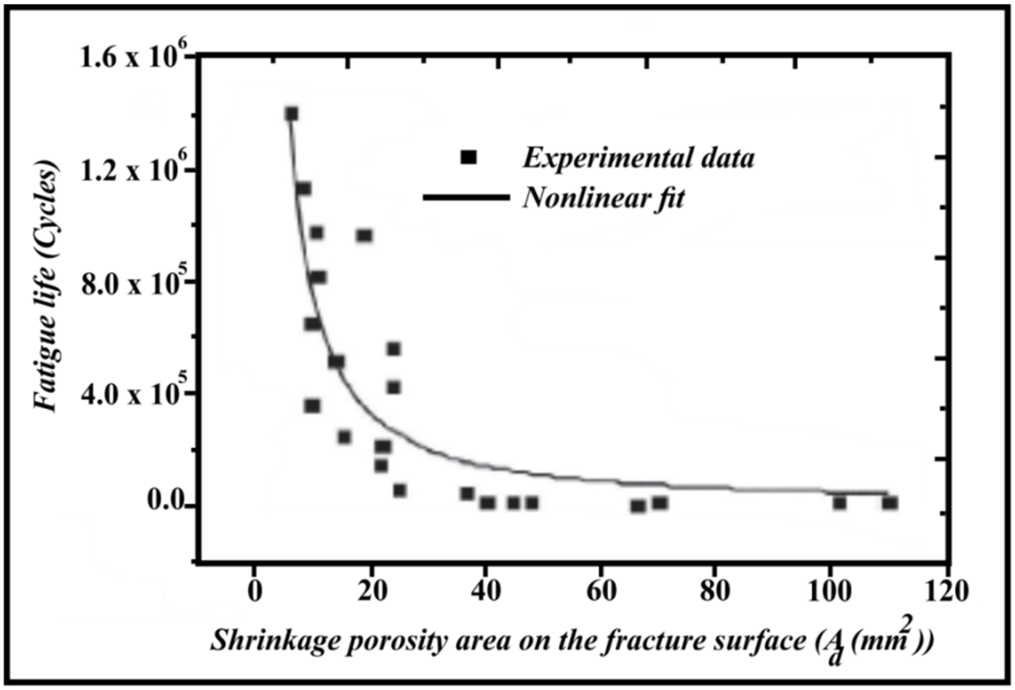

Figure 1.6 The effect of shrinkage porosity area on fatigue life in
QT400-18 cast iron (σ_{max}= 200 MPa, R= 0.06)
Taken and adapted from Liu et al. (2016, p. 51)

- **Gas porosity**

Gas porosity (Figure 1.7) is another common type of casting defect caused by dissolved gases trapped at the solid-liquid interface during solidification. It forms small, smooth, and round voids inside solidified alloy (Thomas, 2000). Thus, gas porosities, as discontinuities, can decrease the load-bearing capacity of the component and weaken the cast metal. Proper degassing procedures of liquid metal can reduce the presence and size of gas pores.

Entrapped gas originates from different sources (Campbell, 2011):

- Air bubbles can be entrained by the flow of the liquid metal filling the mould and then be trapped while the metal solidifies.

- Outgassing of a core or a mould surface when it is heated in contact with the molten metal can cause gaseous decomposition products to force their way into the solidifying metal.

- Gas solubility in liquid metal is higher than in the solid phase. During cooling and solidification, the solid section increases and the dissolved gas following the solidification front will be rejected into the molten metal; this circumstance might lead to the formation of gas porosity as the metal solidifies.

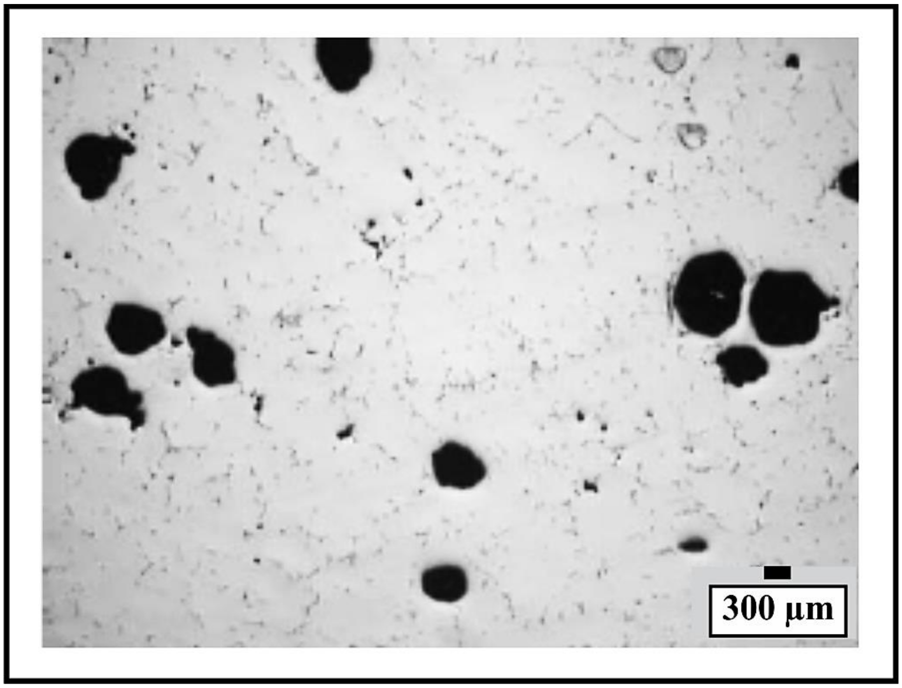

Figure 1.7 Gas porosity in an aluminum AA 5182 remelt secondary ingot
Taken and adapted from ASM Handbook Vol. 15 (2008, p. 370)

- **Segregation**

Segregation means the non-uniformity of chemical composition in the cast section. The deviations from the nominal composition are caused by the redistribution of alloying elements during solidification (ASM Handbook Vol. 15, 2008). Segregation occurs on macroscopic as well as microscopic levels and it can deteriorate material resistance to cyclic loading.

Micro-segregation results from the rejection of alloying elements from solid into the interdendritic liquid and it can be removed or decreased considerably by homogenizing heat treatments and hot working. Macro-segregation, nevertheless, is the consequence of localized micro-segregation areas moving over macroscopic distances. In other words, macro-segregation is the variation of chemical composition on a larger scale and it is more difficult to eliminate (Ghosh, 2001).

The microstructure of cracked areas in volute tongues of pump casing made of CA-6NM showed that a large number of chromium carbides segregated at grain boundaries are likely to cause failure by brittle intergranular cracking propagated along prior-austenite grain boundaries (Kim, Kim & Park, 2002).

- **Inclusion**

Inclusions are foreign materials embedded in a solid alloy matrix and originated from particles like impurities remaining in liquid metal after upstream refining (Thomas, 2000). They behave as stress risers owing to elastoplastic strain incompatibility between them and the surrounding matrix (Stiénon et al, 2009). Besides, they can be potential nucleation sites for porosity formation and increase the number of porosities in the casting. Accordingly, the presence of inclusions might result in degraded mechanical (e.g., fatigue) properties and casting quality.

Figure 1.8 represents corrosion fatigue crack in soft martensitic stainless steel (16%Cr-5%Ni) which initiates at the inclusion. The fatigue test has been performed under uniaxial tension stress (Mathis, 1987).

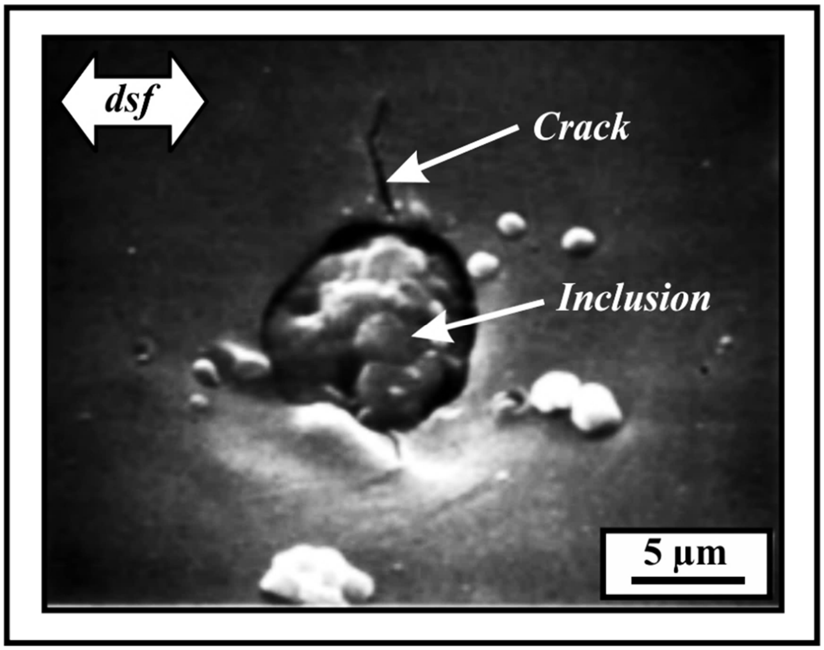

Figure 1.8 Showing soft martensitic steel (16%Cr-5%Ni):
Crack initiation originating from a debonded inclusion
(dsf = direction of uniaxial stress field)
Taken and adapted From Mathis (1987, p. 912)

1.6 Non-destructive testing

As has been mentioned in the former section, internal casting defects cannot be discovered or eliminated easily. Therefore, their effect on the mechanical performance of castings should be assessed in advance. In this regard, different testing methods exist, some destructive and some non-destructive.

Non-destructive testing (NDT) comprises different methods applied to detect, measure, and evaluate defects in various materials such as casting components. Non-destructive testing examines materials either during manufacturing or while in service, without impairing the subsequent serviceability of the component. X-ray radiography, X-ray computed tomography (XCT), ultrasonic, dye-penetrant and eddy-current are some of the non-destructive testing methods.

The non-destructive testing methods applied in the current research are described in the following sections.

1.6.1 X-ray radiography

X-ray radiography is a non-destructive evaluation (NDE) method that works almost on all materials. Radiography is useful for the identification of typical internal defects in various geometrical shapes (e.g., porosities, inclusions, and cracks) to help with the decision about the ability of the manufactured component to perform its function, or the need to repair or completely reject the component. The radiography technique provides a permanent result. It can be applied to casting, forging, weldments and other structural assemblies (Crane & Matikas, 1998).

X-ray radiography is based on the attenuation of X-ray beams as they go through the material under inspection. The projected beams are recorded as a two-dimensional (2D) image on a recording medium. Besides, only those indications that alter the attenuation of the X-ray beams along their path through the structure can be visualized on the recorded images. In this respect, defects parallel to the X-ray beam direction are more easily detected (see the crack in Figure 1.9).

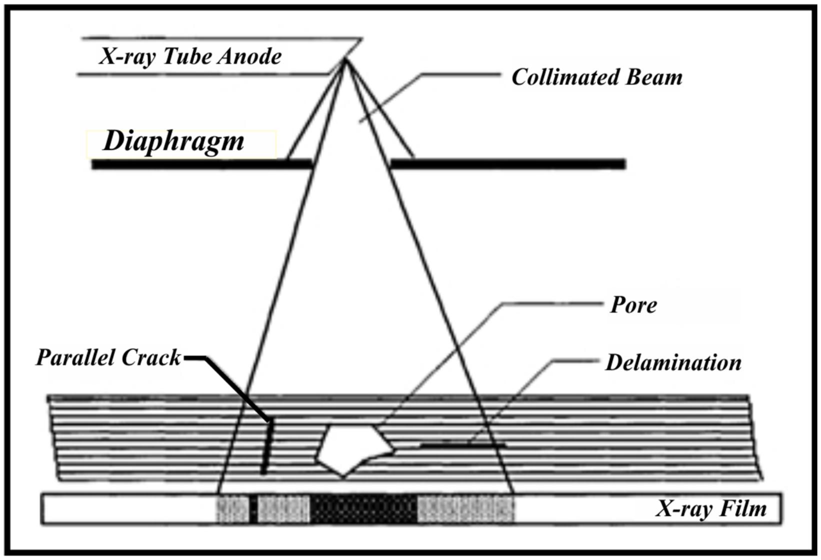

Figure 1.9 Schematic radiograph of a thin plate with different types of flaws
Taken and adapted from Crane & Matikas (1998)

However, X-ray radiography has some disadvantages:

- It is insensitive to thin laminar flaws such as tight fatigue cracks and delamination when they are not well-oriented to the X-ray beam (Figure 1.9).

- Because of the resolution limitation, radiography is limited to the detection of macro-defects. Micro-defects cannot be observed.

- Radiographs of castings contain only two-dimensional (2D) images of the defects. This 2D projection of the defects to a planar shape leads to difficulties in their recognition as it does not provide complete information of the size and morphology of defects with three-dimensional (3D) and complex geometries. Figure 1.10 represents the planar projection of a filamentary shrinkage porosity indication that belongs to the CA-6NM cast blade in the current research.

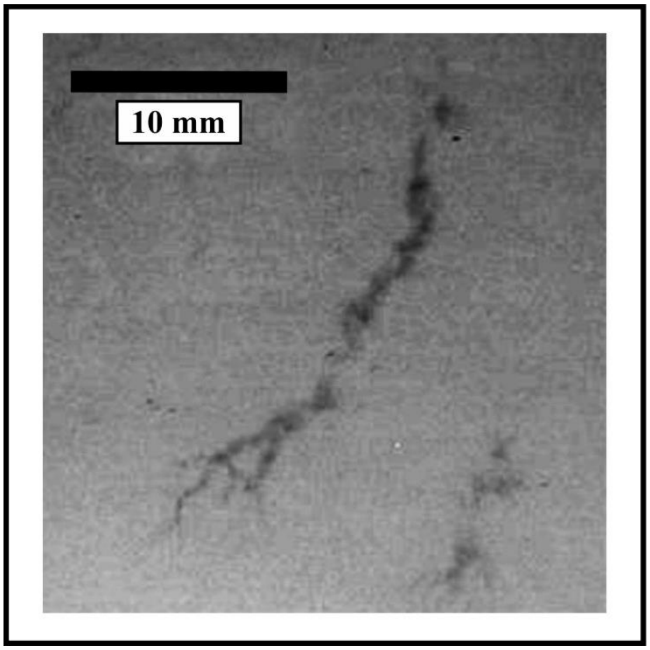

Figure 1.10 Filamentary shrinkage porosity
indication captured by X-ray radiography
(CA-6NM cast blade)

In X-ray radiography, the defect types are categorized by codes and levels of severity from 1 to 5 (ASTM E446). The standard assigns radiographic code to each specific shape of indication (ASTM E446; Meimandi, Vanderesse, Thibault, Bocher & Viens, 2017). Evaluation of indications by a certified technician is based on a comparison with a set of reference radiographic images. Accurate quantitative information about the actual size of inspected defects is hard to obtain which makes this method subjective and imprecise (Meimandi et al., 2017).

Higher energy X-rays are required to penetrate through denser (e.g., steels) or thicker materials. The required amount of energy depends on the geometry and the nature of the material.

1.6.2 X-ray computed tomography (XCT)

X-ray computed tomography (XCT) is a non-destructive and non-invasive inspection that provides spatial and three-dimensional (3D) geometric images of internal structures of opaque materials. Compared to X-ray radiography, XCT has a much higher resolution (in micrometres (µm)), detectability, and more reliable quantitative information.

Figure 1.11a represents an optical micrograph (2D image) of a cross-section of complex shrinkage porosity in Al-Si-Mg casting alloy provided by conventional metallographic techniques and Figure 1.11b displays a three-dimensional (3D) image of the same type of defect extracted from an XCT scan (Boromei et al., 2010).

In materials science (e.g., microstructure characterization and fatigue fields), the XCT is widely applied as it visualizes how the inside of the component is altered and damaged while mechanical deformation, cyclic loading, thermal cycling, etc. (Buffière, Maire, Adrien, Masse, & Boller, 2010). One of the applications of XCT in the fatigue field is using in-situ high-resolution X-ray tomography to monitor the early stages of nucleation and propagation of short fatigue cracks when porosities cause failure (Marrow, Buffière, Withers, Johnson & Engelberg, 2004). Characterization of casting defects namely shrinkage porosity and gas porosity is another area of interest. Using tomographic images, it is possible to analyze the distribution and main characteristics (e.g., size, location and morphology) of porosities from a 3D perspective.

In X-ray computed tomography, there is an X-ray source, an X-ray detector and a rotatory stage with the specimen mounted on it. These three sections are aligned and the rotator is fixed in the middle. In a tomography scan, the X-ray beam is sent through the specimen while the specimen rotates with a constant rotation step. At each angular view plane, an X-ray radiograph (2D image) is captured and recorded on the detector. It means that XCT visualizes a virtual cross-section through the material volume at a selected slice. The XCT non-destructive data acquisition can be performed over the 180° rotation angle of the bulk.

The number of radiographs is equal to the rotation angle divided by the rotation step. The 2D radiograph projections will then be processed and combined by a reconstruction software to generate the three-dimensional (3D) distribution of internal features such as porosities (Nicoletto, Anzelottia & Konečná, 2010). Using image rendering software, a precise quantitative analysis (3D or 2D) of the nature of internal casting defects, as well as their 3D meshes, can be extracted from tomographic images.

Figure 1.12 demonstrates a schematic view of the XCT imaging process. Tomography imaging comprises four steps. Steps 1 and 2 demonstrate a large number of XCT scans obtained through the material bulk over a 180° rotation. Step 3 displays the cross-section images through the volume acquired by a back-projection algorithm. Eventually, step 4 illustrates the 3D reconstruction provided by image analysis software from the stack of 2D images.

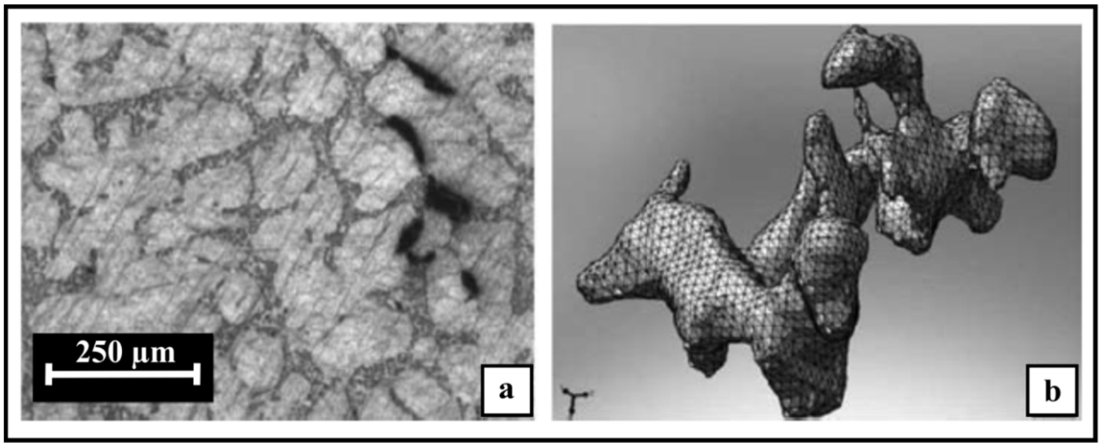

Figure 1.11 (a) Optical micrograph of shrinkage porosity after sample slicing,
(b) 3D image of the same shrinkage porosity obtained by XCT
Both taken and adapted from Boromei et al. (2010, p. 20)

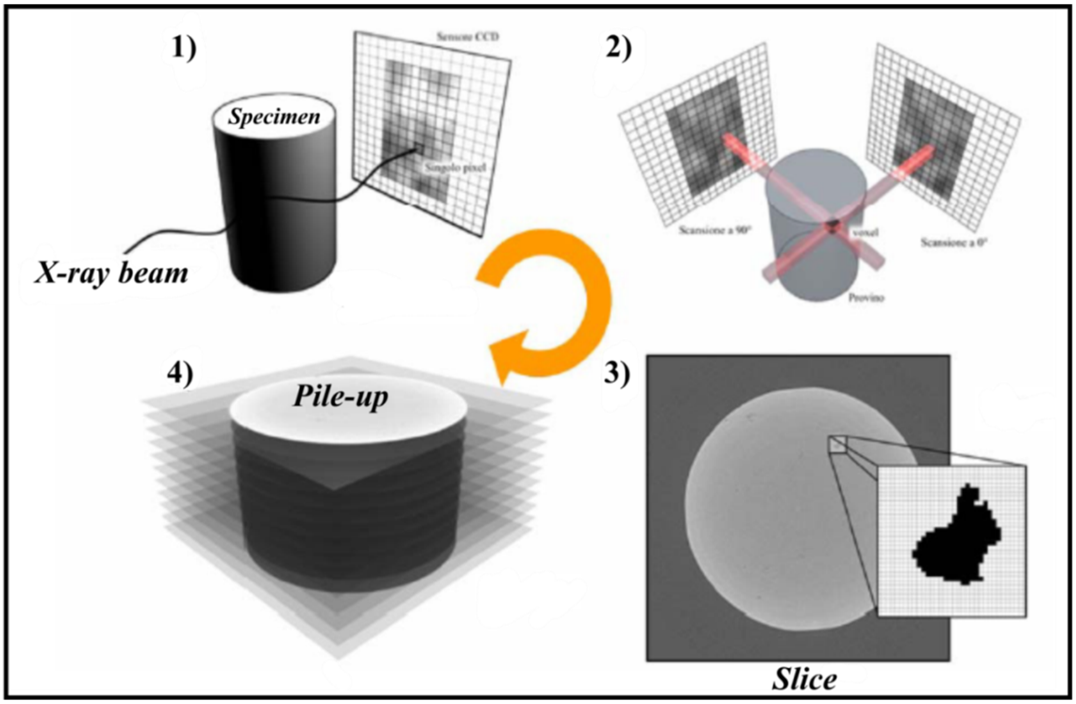

Figure 1.12 Schematic view of X-ray Computed Tomography (XCT) imaging process
Taken and adapted from Nicoletto et al. (2010, p. 549)

1.7 Destructive “Salami” cross-sectioning testing

Besides non-destructive testing, there are also destructive tests to quantify the 3D morphology of the defects. As one of them, “Salami” cross-sectioning is a procedure to establish the shape of defects by sequential sectioning. Standard DNV RP F-118 (Veritas, 2010) describes this destructive method which is based on sequential cross-sections taken at 2 or 4 mm intervals of potential flaws detected by radiography (cf. Chapter 2, Figure 2.4). The digital image of each cross-section enables the various morphological parameters of the defects to be characterized (Meimandi et al. 2017; Ginzel, Thomson & Ginzel, 2011; Veritas, 2010; Denys, 2008; Lozev, Spencer & Hodgkinson, 2005). Using “Salami” cross-sectioning, the radius of defect tips, the diameter and the surface area for different types of defects can be evaluated (Figure 1.13).

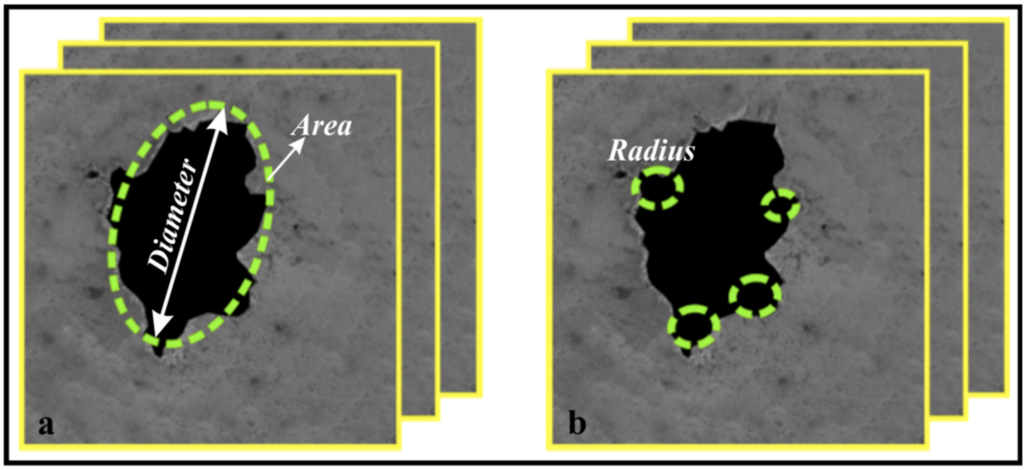

Figure 1.13 Schematic views of “Salami” cross-sections of a defect with characteristics such as (a) defect diameter, area, and (b) tip radius

1.8 Fatigue properties

Fatigue is a mechanism by which casting components fail under dynamic loading conditions. Failure in fatigue usually happens without evident warning, resulting in an abrupt fracture. Besides, fatigue is a cumulative and localized damage process that roughly consists of four stages: hardening/softening, fatigue crack nucleation, crack growth and final catastrophic fracture (Ammar, 2006).

In defect-containing alloys/metals, defects are considered as pre-existent cracks that are the frequent and immediate initiation sites of fatigue cracks while in nominally defect-free alloys/metals, persistent slip bands (PSBs) play the role of stress concentrators and initiate fatigue cracks. For defect-containing cast parts, the total fatigue life essentially consists of the number of cycles that are required to propagate the present crack to a critical size (Huth, 2005). Accordingly, crack propagation will be the controlling mechanism of the failure (Wang, Apelian & Lados, 2001). It was also studied that the presence of the defects like pores could make the fatigue crack initiation phase very short and negligible (Skallerud, Iveland, & Härkegård, 1993). However, if crack initiation is slowed down, the total fatigue life of cast structures might be extended considerably. In this regard, casting quality plays a key role in determining fatigue properties. A well-designed casting system and some methods such as shot blasting, filtering the liquid before casting can be useful for this purpose. By improving the casting quality, the degree of defects decreases and thereupon the fatigue properties improve (Campell. 2011).

1.8.1 Fatigue life assessment approaches

The common approaches for fatigue life assessment are (Stephens, Fatemi, Stephens & Fuchs, 2001):

- The safe life approach is based on the S-N/Ɛ-N curve showing the relation between applied stress/strain and the number of load cycles before rupture.
- The damage tolerance approach is based on fracture mechanics.

Fatigue testing usually includes S-N curve data to define fatigue properties. This approach assumes that components are primarily defect-free. Thus, the S-N curve does not separate the fatigue crack nucleation stage from crack propagation. The total fatigue life is then calculated as the number of cycles both to initiate a crack and afterwards propagate this crack until the final failure happens (Huth, 2005).

In commercial cast components where defects are unavoidable, the obtained properties from the S-N curve are valid for a certain distribution of the defects. In other words, as long as the defects have an equal size or smaller than the current microstructure (e.g., grain size), the specimens are supposed to show fatigue properties comparable to the pure material. Hence, using the S-N curve, it is possible to correlate the fatigue life of a single specimen to defect-free specimens. But, if the defects that initiate the fatigue cracks are larger than a critical size, the fatigue life of these alloys should be assessed using a defect-tolerant approach (LEFM analysis) (Wang et al., 2001). Such an approach relies on a correlation between initial defect (i.e., crack) size obtained through inspection and the remaining life of the part.

1.8.2 Linear elastic fracture mechanics (LEFM)

Linear Elastic Fracture Mechanics (LEFM) is a model to describe the behavior of cracks in solid components that act elastically under fatigue loading. The model is only applied to structures with an existing initial flaw (not applicable in the crack initiation stage) (Björkblad, 2008) and it is a suitable way to estimate the crack propagation rate in a material exposed to stress.

The LEFM model is capable of estimating the crack tip stress field by a parameter called stress intensity factor, K. However, there are some limitations to the application of the LEFM model. For instance, the model is not valid when crack size is less than a critical length. Under this condition, crack shows unusual growth behavior that cannot be explained by LEFM (Taylor, 1988). The size of the plastic zone at the crack tip can be pointed out as another limitation of LEFM.

1.8.2.1 Stress intensity factor

Structural defects commonly cause deviation of load-flow lines and therefore stress concentration. The ratio of the elastically maximum local stress caused by defect geometry to the reference stress of the flawless cross-section can be described as the stress concentration factor ($K_t = \sigma_{max}/\sigma_n$). Stress concentration is evaluated with an elliptical discontinuity which is defined by D (half of the major axis of the elliptical defect) and root radius (ρ) (Figure 1.14). Inglis found that for the elliptical hole, stress concentration is given by equation (1.1) (Inglis, 1913):

$$K_t = 1+2\sqrt{\frac{D}{\rho}} \tag{1.1}$$

Equation (1.1) demonstrates that K_t increases when defect length (D) increases and the defect's radius (ρ) decreases (Hertzberg, 1996). Therefore, stress concentration factor (K_t) generally depends on defect geometry, and (for a given geometry) it also depends on the type of loading (Nicholas, 2006).

Figure 1.14 demonstrates that the stress concentration decreases from a local structural defect as the distance from the discontinuity (l) increases. This decrease is described by the stress gradient.

Nevertheless, the stress concentration factor (K_t) cannot analyze the stress close to the crack tip. This is because at the crack tip, radius (ρ) tends to zero and therefore K_t becomes close to infinity. The LEFM model has solved this challenge by defining stress intensity factor (K):

After the work done by Inglis, Griffith developed an energy-based theory (Griffith, 1921). For a crack in a brittle component, he proposed that the crack propagates if the total energy decreases with crack propagation. This approach in which the material is treated elastically can also be extended to ductile materials with plastic deformation. Irwin discovered that the local stress close to a crack depends on the amount of the applied stress and the crack size

(Irwin, 1957). This correlation is described by a LEFM parameter called stress intensity factor, K:

$$K = Y\sigma\sqrt{\pi a} \tag{1.2}$$

Where σ is the nominal applied stress, a is the crack length, and Y is a geometrical factor that depends on the crack length (i.e., the geometry of the crack), the geometry of the sample and loading configuration.

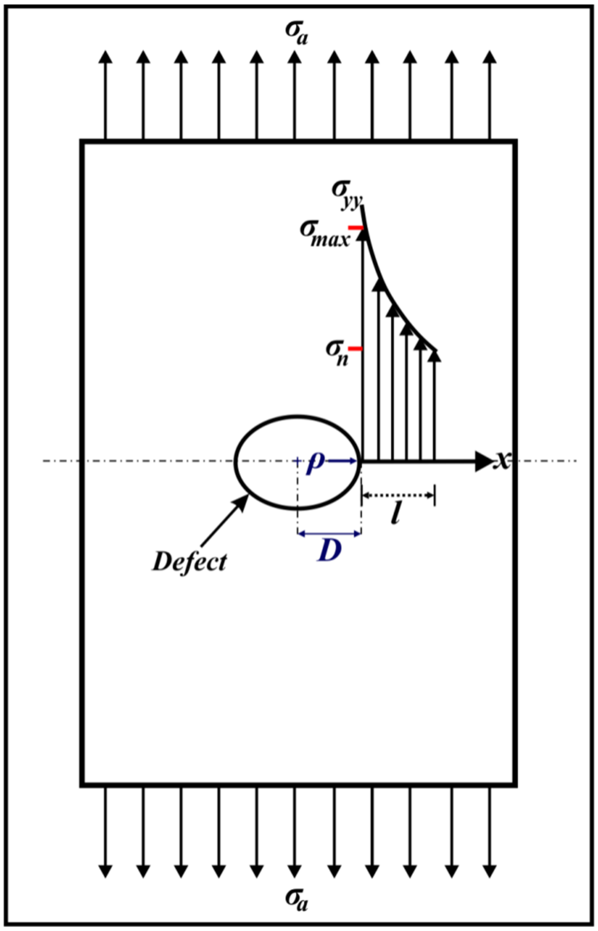

Figure 1.14 Showing stress concentration and stress gradient around an elliptical defect in a uniformly stressed plate

1.8.2.2 Plastic zone size

According to the stress intensity factor definition, the stress state in the immediate neighbourhood of the crack tip for the opening loading mode (*Mode I*) can be expressed by equations 1.3 and Figure 1.15 (Broek, 1988):

$$\left.\begin{aligned}
\sigma_x &= \frac{K_I}{\sqrt{2\pi r}}\cos\frac{\theta}{2}\left(1-\sin\frac{\theta}{2}\sin\frac{3\theta}{2}\right)\\
\sigma_y &= \frac{K_I}{\sqrt{2\pi r}}\cos\frac{\theta}{2}\left(1+\sin\frac{\theta}{2}\sin\frac{3\theta}{2}\right)\\
\sigma_z &= 0\\
\sigma_{xy} &= \frac{K_I}{\sqrt{2\pi r}}\cos\frac{\theta}{2}\sin\frac{\theta}{2}\cos\frac{3\theta}{2}
\end{aligned}\right\} \tag{1.3}$$

For the case that $\theta = 0$ (plane through the crack):

$$\sigma_x = \sigma_y = \frac{K_I}{\sqrt{2\pi r}} \tag{1.4}$$

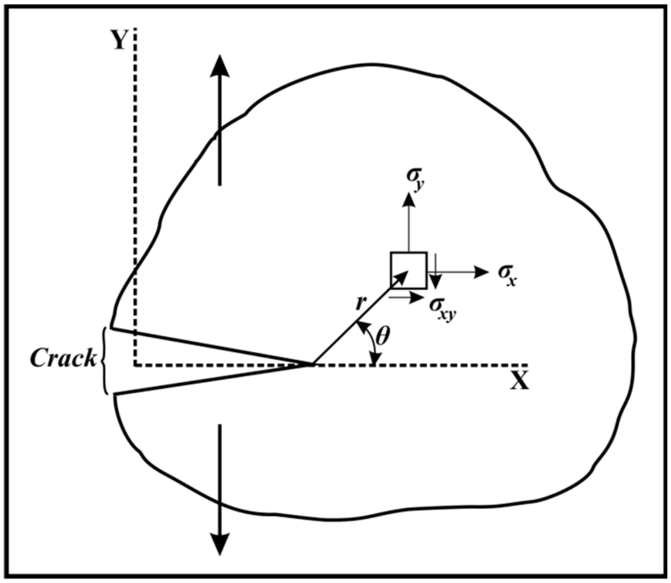

Figure 1.15 Schematic stress field around an arbitrary crack for the mode I loading
Taken and adapted from Broek (1988, p. 50)

Equations 1.3 and 1.4 represent that at the crack tip ($\theta = 0$), the transverse stress (σ_x) is equal to the longitudinal stress (σ_y). Plain strain, therefore, leads to (Broek, 1988):

$$\varepsilon_z = \frac{\sigma_z}{E} - \nu\frac{\sigma_x}{E} - \nu\frac{\sigma_y}{E} = 0 \tag{1.5}$$

with $\nu \approx 0.33$:

$$\sigma_z = \nu\,(\sigma_x + \sigma_y) \approx 0.66\sigma_y \tag{1.6}$$

In loading, plastic deformation occurs when the difference between the maximum and minimum principal stress reaches yield strength (σ_0) (Tresca yield criterion). Thus, for plane strain condition:

$$\sigma_y - 0.66\sigma_y = \sigma_0 \quad \text{or} \quad \sigma_y = 3\sigma_0 \tag{1.7}$$

Equation 1.7 demonstrates that σ_y must be 3 times the yield strength before plastic deformation begins. Instead, in the case of plane stress ($\sigma_z = 0$), yielding will commence when $\sigma_y = \sigma_0$. Hence, the plastic zone size at the tip of the crack will be:

$$\text{plane stress:} \quad r_p = \frac{1}{2\pi}\left(\frac{K_I}{\sigma_0}\right)^2 \tag{1.8}$$

$$\text{plane strain:} \quad r_p = \frac{1}{6\pi}\left(\frac{K_I}{\sigma_0}\right)^2 \tag{1.9}$$

The application of LEFM assumes that the size of the plastic zone at the crack tip is much smaller than the crack length. In other words, there is a plasticity limitation on the LEFM model. Therefore, LEFM is applicable if (Dowling, 2013):

$$\text{plane stress:} \quad a_I \geq \frac{4}{\pi}\left(\frac{K_I}{\sigma_0}\right)^2 \tag{1.10}$$

$$\text{plane strain:} \quad a_I \geq 2.5\left(\frac{K_I}{\sigma_0}\right)^2 \tag{1.11}$$

Where a_I is the distance between the crack tip and any of the other sample's surfaces ahead of the crack tip.

1.8.2.3 Fatigue crack growth

According to the LEFM model, Paris *et al.* (1961) demonstrated that the crack propagation rate in fatigue usually depends on the initial crack size and the stress intensity factor range ($\Delta K = K_{max} - K_{min}$) which is obtained by:

$$\Delta K = Y\Delta\sigma\sqrt{\pi a} \tag{1.12}$$

where $\Delta\sigma$ is the stress range. Accordingly, Paris' law can be written as follows:

$$\frac{da}{dN} = C\,(\Delta K)^m \tag{1.13}$$

where da/dN is usually expressed in (mm/cycle) and where C and m are constants.

Figure 1.16 illustrates the crack propagation per load cycle versus the stress intensity range in three regions. In the first region *(region A)*, for the crack to propagate, the stress intensity range needs to be larger than a threshold (ΔK_{th}), *region B* is the stable crack growth region (i.e., Paris region) characterized by a linear variation between the crack propagation rate (*log da/dN*) and the stress intensity range (*log ΔK*). *Region C* is the unstable crack propagation region that rapidly leads to failure.

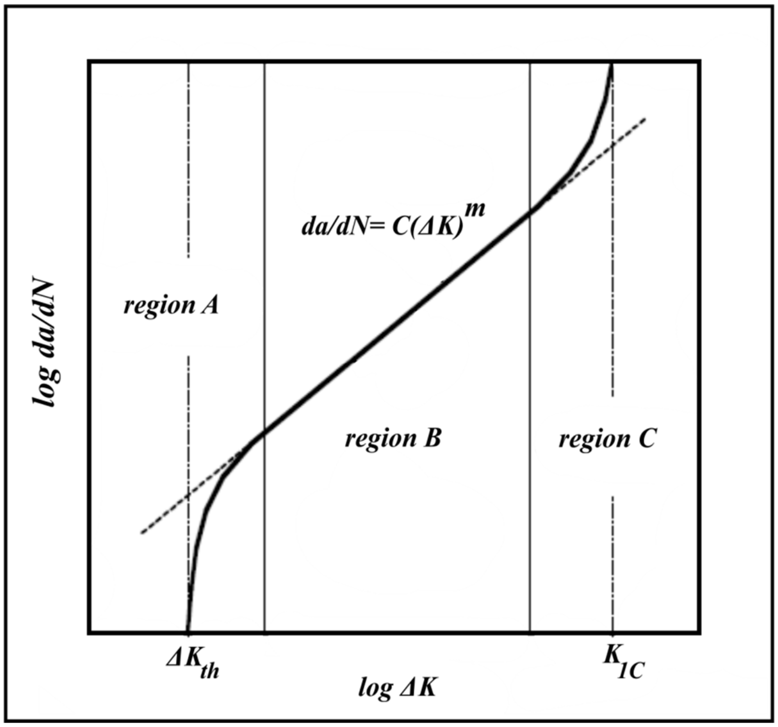

Figure 1.16 Schematic fatigue crack propagation curve
Taken and adapted from Huth (2005, p. 80)

1.9 Fracture mechanics approach: Kitagawa-Takahashi diagram

As the presence of defects in casting components is a widespread fact, it is required to have criteria for tolerable defects in castings. Kitagawa and Takahashi (1967) established a diagram that differentiates a propagating crack from a non-propagating one. Kitagawa diagram brings two threshold values together. The first threshold is the fatigue limit ($\Delta\sigma_{fl}$) evaluated by the safe-life approach. This limit state usually corresponds to the fatigue limit of a defect-free material. The second threshold (i.e., inclined line) is the stress intensity factor from fracture mechanics (LEFM) for long fatigue crack propagation (ΔK_{th}). The long crack propagation threshold is a unique property of the material.

Figure 1.17 illustrates a modified Kitagawa-Takahashi diagram with three regimes of crack growth (Kumar, 2004):

- The microstructurally short crack region in which the fatigue limit of the pristine specimen is demonstrated by a horizontal line insensitive to defects (Björkblad, 2008).

- The transition region in which increasing crack length leads to a gradual decrease in the stress range.

- The long crack region where the fatigue crack propagation follows linear elastic fracture mechanics (LEFM) relations and Paris law.

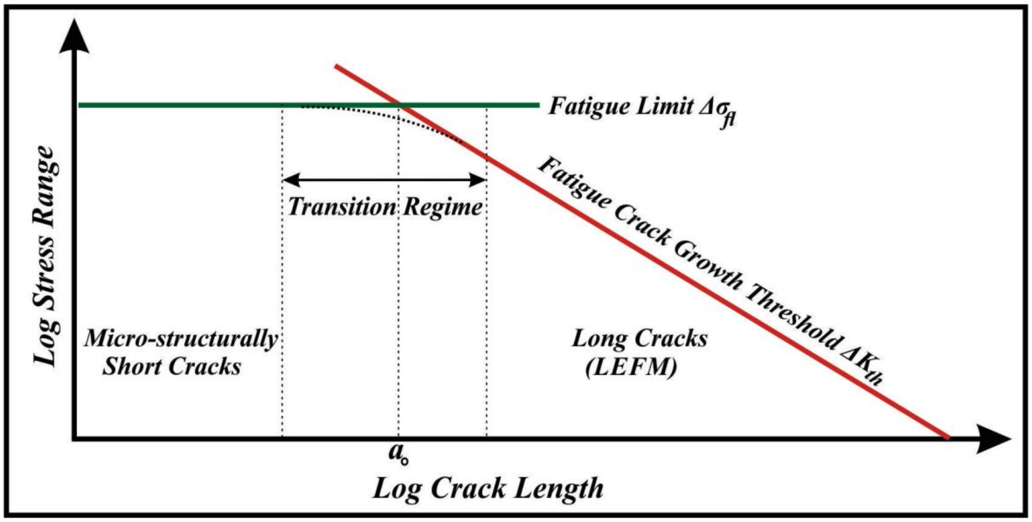

Figure 1.17 Showing three regimes of crack growth in
Kitagawa-Takahashi diagram
Taken and adapted from Kumar, Raman & Pathak (2004, p. 522)

1.10 Effect of casting defect characteristics on fatigue properties

As mentioned earlier (cf. section 1.5), various characteristics of the defects such as shape, position, size, and distribution determine the dangerousness of the defects to fatigue performance of cast materials:

1.10.1 Defect shape

The shape of a defect determines the stress concentration factor ($K_t = \sigma_{max}/\sigma_n$) so that more stress is concentrated in sharper areas. Hence, the defect shape can directly affect fatigue life by facilitating the fatigue crack initiation (Björkblad, 2008). Defects with different shapes show an equivalent average stress-strain concentration around them if they demonstrate the same projected areas on the plane normal to the load direction. Thereby, the loading direction in proportion to the geometry of the defect can also be an important factor in determining the harmfulness of a defect (Li, Lee, Maijer & Lindley, 2009; Björkblad, 2008).

For real cast defects that are usually irregular in morphology, it is not easy to define their shape and although the stress concentration factor is the main element for fatigue life predictions, stress concentration analysis can be complicated due to the complex shapes of these defects (Dabayeh, 1998).

Defects like elongated shrinkage porosities often diverge with three-dimensional (3D) tortuous irregular shapes and diffuse contours. It has been investigated that the impact of elongated shrinkage porosities with smaller sizes on fatigue strength is equivalent to the effect of larger but rounded porosities. Therefore, the impact of complex-shaped porosities on stress concentration and fatigue performance is more severe than rounded ones (Nicoletto, Konečná & Fintova, 2012).

1.10.2 Defect position

The effect of defect position on fatigue life is influenced by the distance to the areas under higher stress. In fatigue, the presence of higher stress in the material gives more energy for crack opening and propagation which makes the life of the component shorter. From one standpoint, the impact of position is represented by the distance of the defect to the surface. Small defects that are located close to or at the specimen surface can increase the stress concentration more than large internal defects and serve as fatigue crack nucleation sites (Dabayeh, 1998). In nodular cast iron, for a given size, the internal defect needs to be almost ten times larger than the surface defect to achieve the same fatigue life (Nadot, Mendez, Ranganathan, & Beranger, 1999). Duckworth and Ineson showed that inclusions of the same size could have a different effect on the fatigue strength of En24 steel based on where they are located in the cross-section of the sample. Inclusions located at the surface were associated with lower fatigue strength than internal ones (Duckworth & Ineson, 1963). Besides, in an A357-T6 cast aluminum alloy, it was illustrated that the detrimental effect of porosities on early crack nucleation is not only depending on their size. The defect position is indeed significant to evaluate the defect's harmfulness (Serrano-Munoz, Buffière & Verdu, 2018). That means the interaction between defect and near-free surface causes an increase of the stress intensity factor (Murakami, 2002).

Furthermore, the fatigue cracks are more frequently originating from the surface as the surface is not ideally smooth. This plus environmental interaction can originate microscopic stress concentrations. Eventually, material discontinuities such as porosities create higher stress concentration when they are at the free surface rather than if they were internal.

From another point of view, the position effect is illustrated by the distance of the defect to the areas under load. This comes from the fact that the component is usually not loaded uniformly during its operation. One example is from a study of stress levels in Francis turbine runners (Figure 1.18) which shows that the maximal stresses are located in the areas where the blades are connected to the crown. These parts (red spots marked with arrows in Figure 1.18) will be more sensitive to the presence of the defects. Higher applied stress levels in those areas can reveal even small defects as serious ones and on the other side, larger defects can be present without any significance to fatigue life in areas of the part which are under low stress.

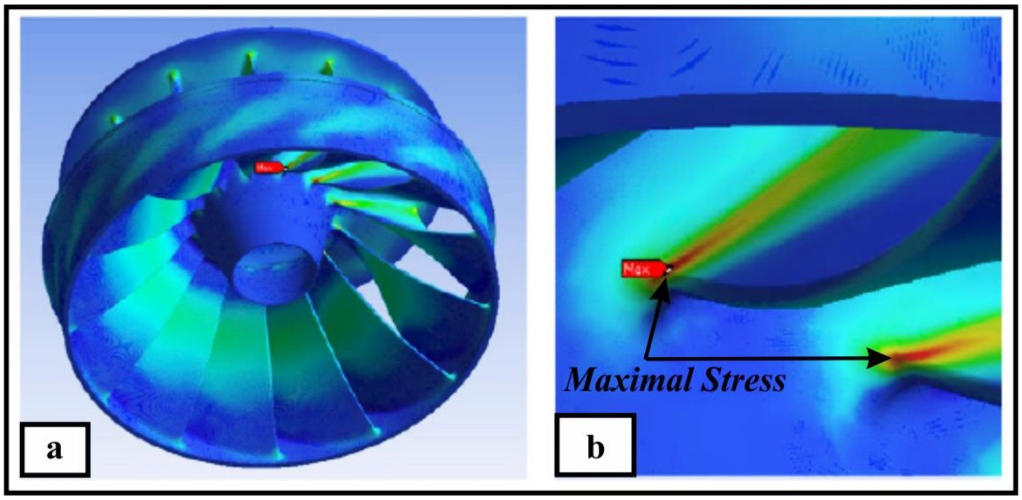

Figure 1.18 (a), (b) Showing maximal stress in the connection spot of the blade to the crown in Francis turbine runners (red signs)
Taken and adapted from Saeed, Galybin & Popov (2010, p. 1252)

1.10.3 Defect size

Size is the principal parameter for cast defects as it determines the fatigue limit (Murakami, 2002). It has been studied that a critical size of casting defects is essential to diminish fatigue life. Defects are required to be larger than the microstructure features (i.e., grain size) (Mu et al., 2014).

For near-spherical-shaped defects (e.g., gas porosities and inclusions), the spherical diameter describes the defect size. This sizing parameter can be determined on two-dimensional (2D) metallographic cross-sections.

For fully three-dimensional (3D) elongated casting defects with irregular shapes (e.g., shrinkage porosity), it is not straightforward to determine the size. In order to characterize this type of defect from a two-dimensional (2D) description, a variety of defect size definition exists. Some of the defect size definitions in terms of area and diameter are described as follows (Figure 1.19 and Figure1.20):

- Murakami uses "effective area" as a representation of the area parameter of the defects. An "effective area" is estimated by considering a smooth contour that envelops the projection of a defect or a crack onto the plane perpendicular to the maximum tensile stress (Murakami, 2002; Meimandi et al. 2017) (Figure 1.19a).

- The area of an ellipse that envelops the defect is a particular case of defect size to estimate (Figure 1.19b).

- Murakami's geometrical parameter ($\sqrt{area}$) which is defined as the square root of the defect projected area (Murakami, 2002). This parameter approximately translates the shape and the size of a defect into one single measure, which is most feasible for non-uniform defects (Figure 1.20a).

- Feret's diameter: the longest distance between any two points along the outlined boundary (Meimandi et al. 2017) (Figure 1.20b).

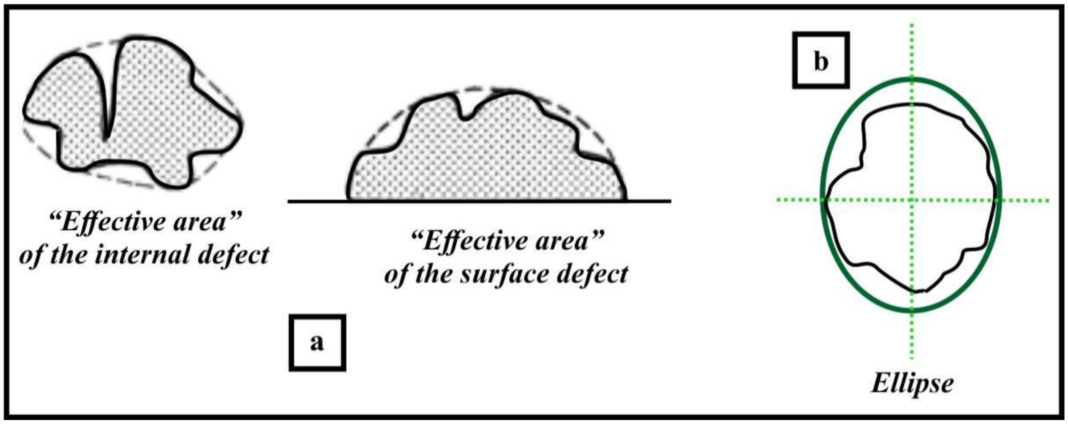

Figure 1.19 (a) Estimation of "effective area" for irregular-shaped defects
Taken and adapted from Murakami (2002, p. 18),
(b) ellipse covers the complex-shaped defect

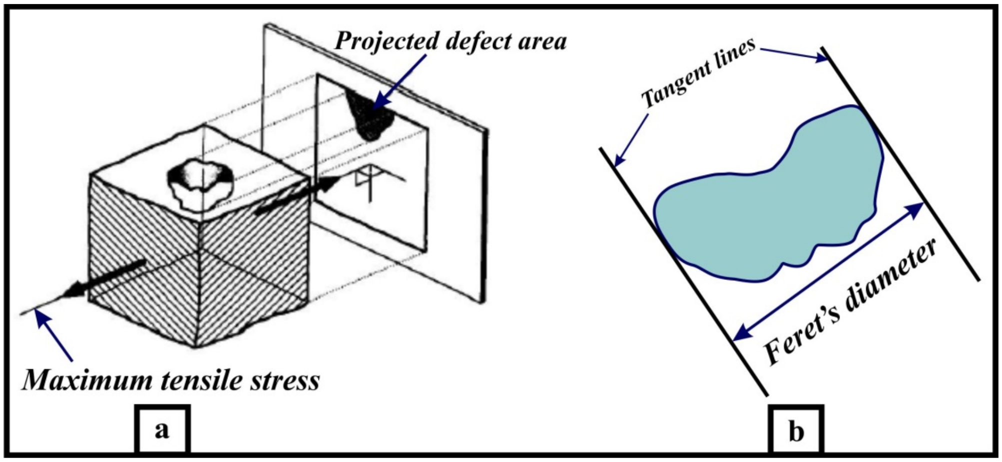

Figure 1.20 (a) Definition of Murakami's geometrical parameter ($\sqrt{area}$)
Taken and adapted from Murakami & Endo (1994, p. 172),
(b) definition of "Feret's diameter"

1.9.4 Defects distribution

Distribution of the defects has significance in fatigue life. Random distribution of defects is less significant than clustered discontinuities. In other words, multiple defects on the same cross-section might interact together and have a more severe effect than the individual ones (BS 7910:2005, 2005). Due to the interaction of neighbouring defects stress concentration might increase; therefore, the cluster of defects should be considered as a single weakening factor rather than treated as a set of isolated defects (Jayet-Gendrot, Gilles & Migne, 2000).

The interaction between a defect and another nearby one increases the intensity of the stress concentration as compared to an isolated one. In Figure 1.21, the interaction between neighbouring defects will be considered significant when the length DA is smaller or equal to CD. Otherwise, the interaction effect is negligible. If the length DA is smaller than CD, neighbouring defects may merge by fatigue crack growth. For interacting defects, their "effective area" is estimated by considering a smooth contour that envelopes all of them together (Murakami, 2002).

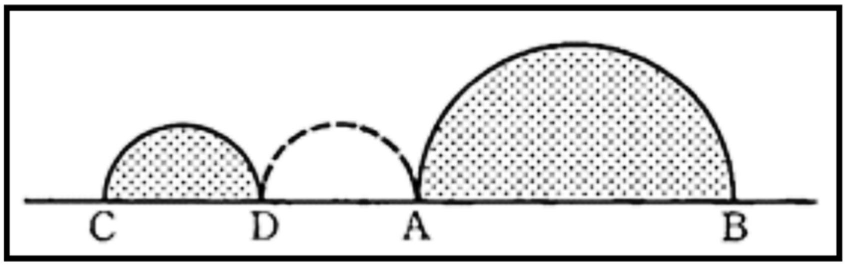

Figure 1.21 Interaction effect between two adjacent cracks
Taken from Murakami, (2002, p. 23)

1.11 Effect of shrinkage porosities on fatigue properties and mechanical performance of cast steels

As has repeatedly been concluded, the effect of porosity (gas or shrinkage type) on the casting quality and mechanical properties is of critical importance. Numerous investigations have represented that the presence of porosity plays a key role in determining the fatigue performance of Aluminum casting alloys (Ammar, 2006). For steel castings, such studies are not as self-evident and well understood. Detailed below are some of the research about cast steels:

Hardin and Beckermann (2012) studied the effect of shrinkage porosity on deformation, damage and tensile fracture of the cast steel. A combination of experimental and computational investigations was performed using industrial radiographs. Radiographs are used to reconstruct and measure the porosity so it can be included in simulations. Predicted and measured tensile curves, elongation results and fatigue lives were in good agreement. The most remarkable effect of porosity was ductility reduction due to its distribution and this was also well predicted.

Kim *et al.* (2006) studied the effect of casting micro-shrinkage in microstructure on fatigue properties of 17-4PH stainless steel. This investigation showed that fatigue properties are influenced by the total area of defects more than the maximum size. Accordingly, clustered micro-shrinkages are more effective in originating fatigue cracks.

Sigl *et al.* (2004) studied the effect of porosity on fatigue properties of 8630 cast steel. The fatigue and monotonic tensile tests were conducted on cast specimens containing porosity levels that varied from micro- to macro-levels. The fatigue results for the micro-and macro-porosities were compared with sound material and a negative effect on fatigue properties caused by the presence of porosity was perceived. Monotonic tensile tests exhibited that specimens with micro-porosity had strength properties comparable to sound material but with a significant reduction in ductility.

Briggs (1969) studied the effect of internal shrinkage discontinuities on the fatigue and impact properties of cast steel sections (8630 type). This study represented that shrinkage porosities reduce the fracture energy in bending impact testing and the amount of this reduction increases with the severity level of shrinkage porosity. Besides, the bending fatigue properties were markedly deducted when various levels of shrinkage porosity extended to the surface of test samples.

In another research, Briggs (1966) investigated the effects of surface discontinuities on the fatigue properties of 8630 cast steel sections. This study also demonstrated that the presence of severe surface defects has a detrimental effect on fatigue strength in torsion and bending.

1.12 Fatigue in Francis turbine runners

Francis turbine runners are under two loading types (Kubota & Tanaka, 1984):

- Low cycle fatigue (LCF): Large alternating stress levels with a low number of cycles (i.e., 10^3 to 10^5) such as a few start-stop cycles of the runner during each day. In this case, fatigue cracks initiated from casting defects will propagate by start-stop cycles and become critical when the stress intensity range passes the fatigue crack growth threshold.

- High cycle fatigue (HCF): Stress amplitude is relatively small, but they occur under high cyclic loads (i.e., 10^9 to 10^{11}) caused by the interaction between the runner and the wicket gates. HCF contributes to crack propagation by small-amplitude stress cycles, leading to growth.

In conclusion, after this review of casting defects and their influence on the fatigue properties of cast parts, it is evident that there are many challenges and one might wonder why the casting process is still used by the industry. The simple answer is that casting is economical and for a lot of cases it is the only method to manufacture a given product. Therefore, it is essential to find strategies that can prevent catastrophic failures and economical loss.

CHAPTER 2

MACRO-DEFECTS CHARACTERIZATION IN CAST CA-6NM MARTENSITIC STAINLESS STEEL

Shilan Meimandi [a], Nicolas Vanderesse[a], Denis Thibault[b], Philippe Bocher[a], Martin Viens[a]

[a] Department of Mechanical Engineering, École de Technologie Supérieure,
1100 Notre-Dame West, Montreal, Quebec, Canada H3C 1K3
[b] Hydro-Québec's Research Institute (IREQ), Varennes, Québec, Canada J3X 1S1

Paper published in *Materials Characterization*, November 2017

2.1 Abstract

Cast low carbon CA-6NM (13%Cr-4%Ni) martensitic stainless steel has been used for hydraulic turbine runners manufacturing since the 60's owing to its high strength, toughness, corrosion, and cavitation-erosion resistance. These castings contain several types of defects which may have detrimental effects on the performance of the produced parts. Several aspects of the casting defects in these steels have not been specifically studied in detail. It is common in the industry to evaluate the integrity of cast components by non-destructive testing such as X-ray radiography before putting them in operation. However, the tortuous and complex geometry of macro-shrinkage porosities makes them difficult to be characterized precisely only by 2D radiographic results. In the present study, the relation between radiography mapping and actual macro-defect morphologies has been studied by the "Salami" cross-sectioning method in order to document the real shape and morphology of defects. Furthermore, metallographic characterization of cast microstructure in CA-6NM stainless steels has also been performed using several techniques to document both chemical composition and microstructure around macro-defects. Briefly stated, the main purpose of the investigation described herein is to study several severity levels of macro-defects in cast martensitic stainless steels and investigate some characteristics of real defects that can impact the fatigue properties of cast parts at the microstructural level.

Keywords: Hydraulic-turbine, Macro-shrinkage porosity, Cast martensitic stainless steel, Characterization, Shape analysis

2.2 Introduction

Soft martensitic stainless CA-6NM cast steels are widely used for hydraulic turbine runner castings (Figure 2.1) since they possess high toughness together with excellent resistance to cavitation and erosion (Iwabuchi, 1987; Thibault, Gagnon & Godin 2015; Ferreño et al., 2011; Tokuda et al., 1970; Iwabuchi & Sawada, 1982; Larson & Fisher R, 1979). CA-6NM has low carbon content with a maximum of 0.06 percent in weight percentage which results in a good castability when compared with other martensitic stainless steels (Behal & Melilli, 1982).

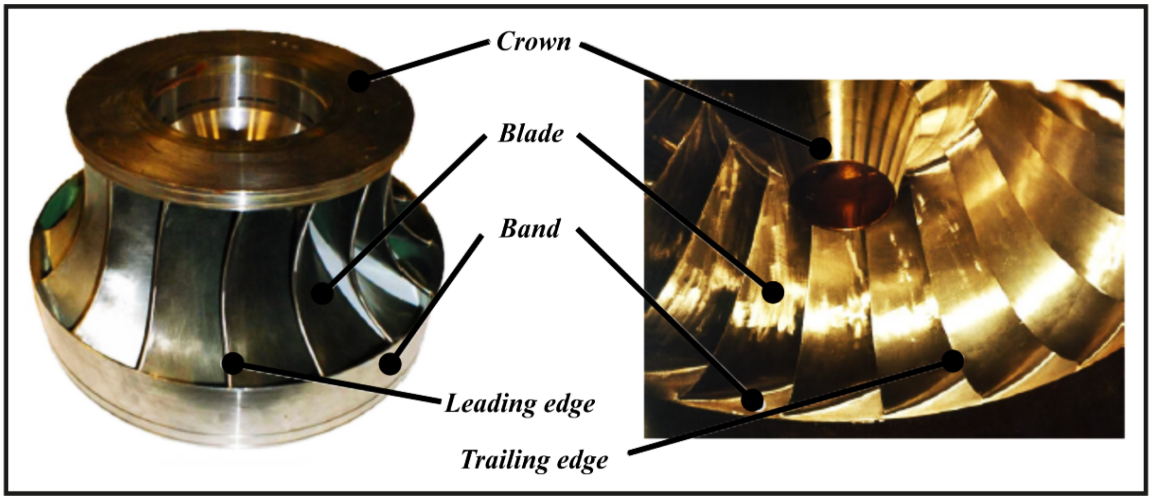

Figure 2.1 Runner- the most vital part of Francis turbine runner
Taken and adapted from Huth (2005, p. 14)

In fact, casting is a method used to make parts with complex shapes at low cost and high production rates (Moore, 1981); however, its drawback is that defects are introduced into metal parts from a deficient melt, inefficient casting design, or imprecise control of the solidification process (Stefanescu, 2009). Some types of casting discontinuities can be represented as inclusion entrapment, shrinkage porosity, gas porosity, and mold-wall interactions, to name a few (Campbell, 2011; McMaster, 1959). Casting defects are frequently the main cause of cracks when the part is put in operation, sometimes resulting in complete component failure. To anticipate the remaining life of hydraulic turbines and improve their performance, it is important to understand the heterogeneities inherent to the defects found in cast microstructure by characterizing their corresponding types, sizes, morphologies, positions, and later on, determining their effect on mechanical properties in order to establish adequate conditions for operation.

To ensure that casting components meet the adequate quality in terms of defects, their integrity is generally evaluated through non-destructive testing such as X-ray radiography before installation. Radiography is a non-destructive evaluation method (NDE) commonly used to identify the presence of internal defects in parts. It gives a picture of the flaw profile, including dimensions and positions on the radiography's film plane, and provides a decision tool whether a manufactured component should be approved, repaired or rejected (McMaster, 1959).

Radiography has however some drawbacks. Radiography is limited to macro-defects, as the typical resolution is in millimetres, and has a poor probability of detection (POD) for planar defects if they are not well-oriented with respect to the film plane. In addition, radiography generates 2D images that capture incomplete information of 3D defects having irregular geometries (McMaster, 1959; Hellier, 2013; Martz & Logan, 2002). However, according to radiographic images generated on castings investigated in this research, defects are mainly expected to be different types of macro-shrinkage porosities.

Among all defect types, shrinkage porosity is one of the most common ones found in casting structures. They result from insufficient liquid metal feeding of casting sections as molten metal solidifies (Campbell, 2011). Since shrinkage porosities develop as tortuous three-dimensional defects, it is difficult to characterize them precisely only by 2D radiographic results. Shrinkage porosities extend from the macroscopic to the microscopic scale. Macro-shrinkage porosities are large enough to be detected even by unaided eyes on non-destructive graphic inspection, while micro-shrinkage porosities are not visible without magnification (ASM Handbook Vol. 11, 2002). Their shape is as important as their size, as elongated pores have a stronger detrimental effect than round pores on mechanical properties. As discontinuities in casting structures, pores do not have any material to support the load, causing stress concentration in the remaining material and severely reducing the mechanical strength in cast components, specifically fatigue strength (ASM Handbook, 2009; Sigl et al., 2004; McDowell, Gall, Horstemeyer & Fan, 2003).

Many approaches have been proposed in order to assess the influence of a defect on fatigue life. An overview of that problem can be found in Murakami's work. A defect can be considered against fatigue using four parameters: defect type, morphology, position, and size (Vincent, Nadot, Nadot-Martin & Dragon, 2016; Murakami, 2002). Due to the complex nature and irregular shape of shrinkage porosities, their size is usually characterized in terms of area. A variety of defect size definitions exist. One of the popular definitions is Murakami's defect area parameter ($\sqrt{area}$) (Murakami, 2002).

In the present work, the relation between radiography mapping of cast CA-6NM and actual macro-shrinkage morphologies with several severity levels have been characterized by the "Salami" cross-sectioning method. "Salami" cross-sectioning is a procedure to establish the shape of defects by sequential sectioning. Standard DNV RP F-118 describes this destructive method to precisely measure dimensions of a single defect by sequential cross-sections at 2 or 4 mm intervals of potential flaws detected by radiography. The digital image of each cross-section enables the various morphological parameters of the defects to be characterized (Veritas, 2010; Ginzel, Thomson & Ginzel, 2011; Denys, 2008; Lozev, Spencer & Hodgkinson, 2005). Using such a method, the radius of defect tips, the diameter of the defects and the surface area for various shrinkage porosity categories were evaluated. Accordingly, shrinkage categories with different levels of severity were compared qualitatively and quantitatively. This information is useful for a correct assessment of the fatigue behavior of the cast parts.

Chemical segregation around defects has also been investigated. Indeed, chemical segregation can be a consequence of the solidification process and results in a non-uniform composition (Stefanescu, 2009). Since chemical segregation can vary significantly at microscopic or macroscopic levels, affecting the part’s mechanical performance, it is of practical interest to study the material around the defect; document how different it is from the matrix, and characterize an element or phase segregation that could embrittle this region.

2.3 Experimental procedue

2.3.1 Material

This study investigates the properties of a cast blade from Francis turbine runner in which, indications with different severity levels have been detected by X-ray radiography. The test samples are then taken directly from the cast blade. The experimental material used in this study was a CA-6NM martensitic cast blade with the composition given in Table 2.1. This composition was determined by optical emission spectroscopy, high-temperature combustion (for C and S) and inert gas fusion (for O and N).

The as-received CA-6NM blade was cast vertically in a sand casting process. In the casting pattern, the trailing edge was located at the bottom and the leading edge on top of the blade. Risers were placed over the leading edge. Molten metal was provided in an arc furnace, and then it was poured from the bottom of the ladle into the mold through the trailing edge. Molten metal was allowed to be solidified from the trailing edge to the leading edge. After initial melting and before pouring into the mold, refining of the melt was performed using an AOD (Argon Oxygen Decarburization) process.

Subsequently, the CA-6NM casting blade was normalized and tempered. The as-received cast microstructure of the normalized and tempered material is mostly martensitic but can also contain delta ferrite and retained austenite (Bilmes et al., 2001).

Table 2.1 Chemical composition of the base metal investigated in the current study (wt. %)

C	Cr	Ni	Mo	Mn	Si	P	S	Fe
0.016	12.79	3.49	0.55	0.5	0.26	0.019	0.007	Bal.

2.3.2 X-ray radiography and “Salami” cross-sectioning

Regarding the preparation of test coupons, at first, X-ray radiographic images were taken all over the blade from a top view (Figure 2.2a). Those images were captured on films with dimensions of 35.5 cm x 43 cm (Outlined area within Figure 2.2a). The radiographs were performed using a source of iridium 192 with a focal point of 4.0 mm on Kodak films. As indicated in Table 2.2, the corresponding defect types to each area of the blade were categorized by codes and levels of severity from 1 to 5 (ASTM E446-98, 2004; ASTM E186-98, 2004). Evaluation of indications was performed by a certified technician based on a comparison with a set of reference radiographic images. It is noteworthy that indications were only found in specific places subjected to shrinkage porosities. Areas with potential defects, here designated as areas of interest, are identified in Figure 2.2b. In the second step, several blocks with various types of indications were extracted from the areas of interest. In order to reveal additional information, high-resolution radiographs were provided for these extracted blocks (Figure 2.3). Table 2.3 specifies all setting parameters used for the X-ray radiography.

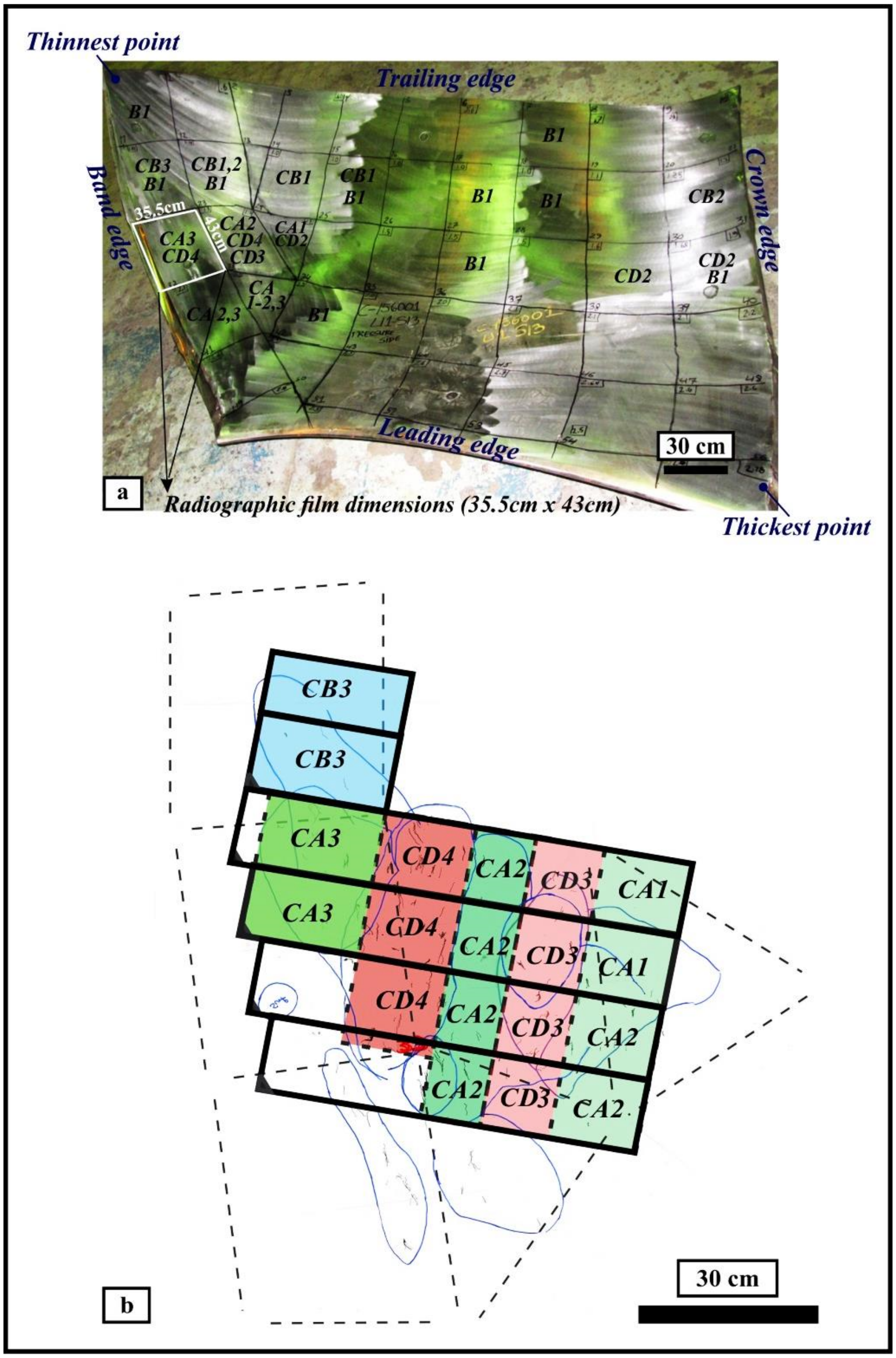

Figure 2.2 (a) Blade image showing the geometry of the blade and distribution of defect types and severity levels according to ASTM standards E446 and E186 (ASTM E446-98, 2004; ASTM E186-98, 2004), (b) Sketch of cutting plan from radiograph images representing areas of interest in the blade

Table 2.2 Radiographic codes of casting defects according to ASTM E446 and ASTM E186 standards (ASTM E446-98, 2004; ASTM E186-98, 2004)

Code	Indication
A	Gas porosity
B	Sand or slag inclusion
C	Shrinkage
CA	Individual Shrinkage
CB	Grouped Shrinkage
CC	Sponge Appearance
CD	More dense but similar to CB

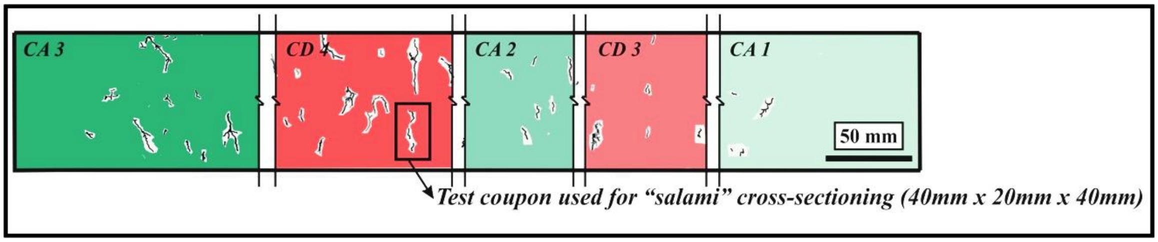

Test coupon used for "salami" cross-sectioning (40mm x 20mm x 40mm)

Figure 2.3 Sketches from radiographic images showing macro-shrinkage porosity categories with different severity levels (darker colors show more severe areas)

Table 2.3 X-ray radiography setting parameters

Distance from tube to film	Voltage	Current	Focal spot	Exposure time	Film type
1016 mm (40 inches)	350 kV	5 mA	5.5 mm	250 seconds	Kodak mx125 (Fine Grained)

In the X-ray radiography method, precise information about the actual sizes and 3D morphologies of inspected defects are missing, which makes this method subjective and imprecise. Therefore, the "Salami" cross-sectioning procedure was used to provide more detailed information about the actual defects and their morphologies. For this purpose, 12 coupons with average dimensions of 40 mm in length, 20 mm in width, and 40 mm in thickness were extracted from 6 areas of interest (Outlined area within Figure 2.3). Those areas included several shrinkage porosity types with various severity levels, namely CA (CA1, CA2, and CA3), CB (CB3), and CD (CD3, CD4) (Figure 2.2b, Figure 2.3). 3 to 6 defects on average were found in each specific severity level. Using the Accutom-50 (Struers) precision cut-off machine, all salami slices were cut at 1.5 to 2 mm intervals. Figure 2.4 illustrates a defect detected by X-ray radiography and a schematic view of "Salami" cross-sectioning. With this precise slicing technique, 0.5 mm-thick material is removed between each interval. The coupons were sliced perpendicular to the direction of radiographic projection.

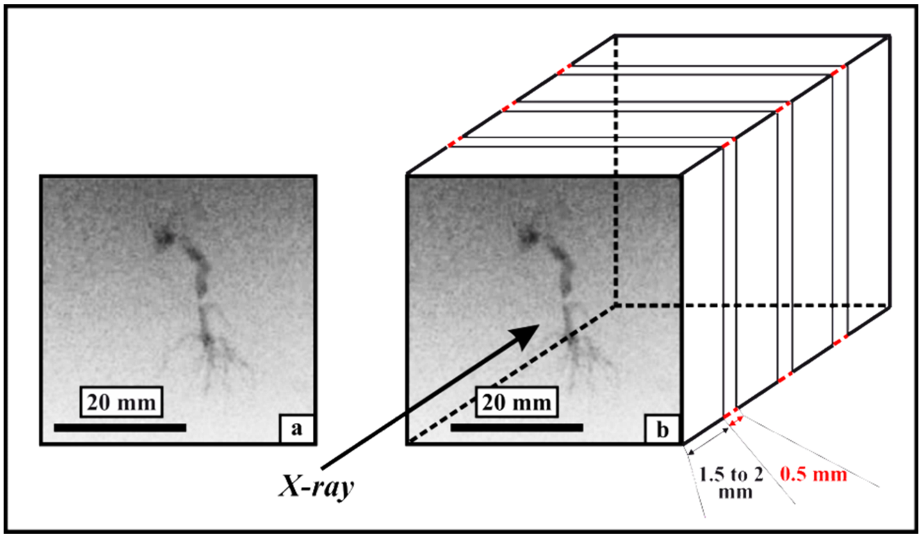

Figure 2.4 (a) A defect detected by X-ray radiography,
(b) Schematic "Salami" cross-sectioning

2.3.3 Preparing for Macro-Micro structure evaluation with metallographic techniques

The slices were degreased with isopropanol in an ultrasonic bath. Prior to imaging, the surfaces of slices were not ground or polished; in that way, the entire information related to defects could be preserved as much as possible. A Clemex L2.OC optical microscope was used to examine the macrostructure characteristics of slices at magnifications up to 50x. Digital images of the macroscopic structures were produced by a mosaic of several microscopic images related to opposite faces of each slice (Figure 2.5). Subsequently, image processing software Fiji, ImageJ, was used to quantify some characteristics of the defects which include the radius of defect tips, the diameter, and the surface area.

Using image processing methodology, 779 isolated defects were detected in total. These defects are related to extracted coupons of all shrinkage porosity types with different severity levels. Since crack propagation and failure in materials are extreme value-related phenomena, the goal of the data analysis was to quantify the most severe characteristics of the defects (smallest radius of defect tips and the largest dimension of the defects). This data was studied for the highest severity levels of each shrinkage porosity class. It is also noteworthy that the information on both sides of each slice was provided to collect more data for statistic representativeness.

After sectioning and macrostructure evaluation, some slices from each porosity type and level of severity were selected to study the cast microstructure and analyze the chemical segregation around the defects. Thin slices were mounted, but before mounting, to avoid defects filling with mounting powder and keep their interior as clean as possible, specimens were wrapped with an aluminum foil. The slices were ground with 800 and 1200 SiC abrasive grinding papers followed by polishing using 6, 3, and 1 μm diamond suspensions with an alcohol-based on silk polishing pad. Between each step, samples were immerged in an isopropanol ultrasonic bath for 3 to 5 minutes. The chemical etching was performed to reveal the microstructure of the cast material around the defect. Samples were swabbed for 45 seconds in Vilella’s reagent (5 cc HCl + 2 gr Picric acid + 100 cc Ethyl alcohol) (Small, Englehart & Christman, 2008). A Hitachi S-3700N scanning electron microscopy (SEM) at 15 Kev was also used for additional observations. Using this machine, the chemical composition variation around the defects of all shrinkage porosity types in each severity level was measured by Energy Dispersive X-ray spectroscopy (EDX) analysis. Those measurements in different line-scans and point-scans were carried out at magnification of 1000x from the edge of the defect to the sound matrix at a distance of 200 µm. Microstructure analysis will be presented in section 2.4.1.

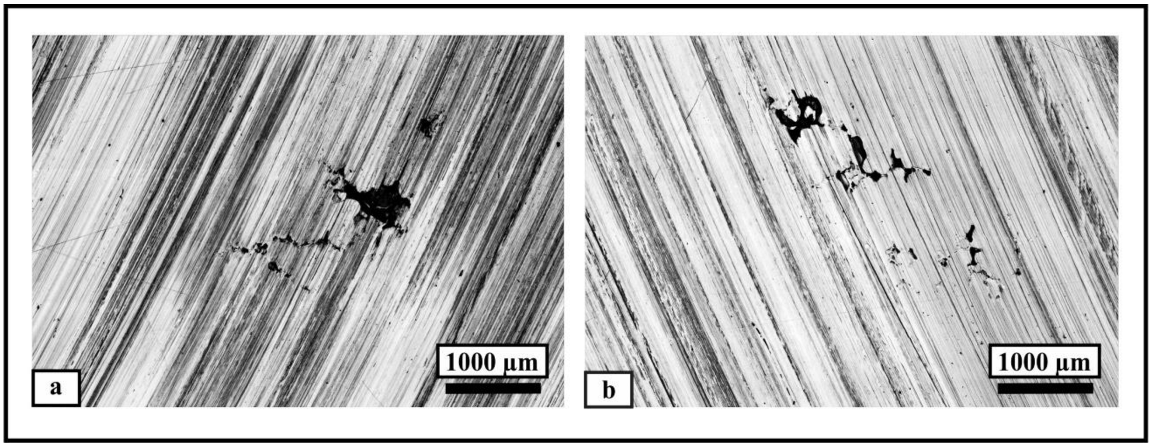

Figure 2.5 (a), (b) Opposite faces of a slice with a macro-shrinkage in CB3

2.3.4 Shape analysis of the defects

After cross-sectioning, slice images were analyzed in order to quantify the morphological parameters of the defects. Using the open-source image processing software Fiji (Schindelin et al, 2012), based on ImageJ (Schneider, Rasband & Eliceiri, 2012), the analysis was carried out and extended with a Fourier shape analysis plugin (Tupper & Boudier, 2009). The images were first converted into 8-bit. The defects were then manually segmented using a region growing algorithm, which selects contiguous pixels having similar gray levels (Figure 2.6). Several basic morphological parameters were evaluated as follows:

- Area: Defined as a smooth ellipse area that encompasses the original shape of the defect.

- Feret's diameter (L): Defined as the longest distance between any two points along the outlined boundary (Ferreira & Rasband, 2012).

- Curvature: The curvature profile along the contour of each defect was computed using a method based on the approximation of the contour by the sum of closed curves which is related to the principle of Elliptical Fourier Analysis. This method is commonly used for shape analysis in biology (Glasbey, Horgan & Wiley, 1994; Carlo, Barbeitos & Lasker, 2011). The curves, called harmonics, relate to the surface of the defect, its elongation, and the amplitude of concavities and convexities. The higher the harmonic level the smaller the scale. Depending on the number of harmonics taken into account, the shape can be approximated with varying detail. The contour of the defects was approximated with 50 harmonics. This value accounted for high-resolution reconstruction of the defects with an acceptable low level of noise. The local curvature values were then calculated on these approximated curves. Because the concave corners of the defects, here specified as negative values of curvature, will not cause a severe effect on fatigue properties; therefore, only convex corners (positive curvature values) were considered.

- Radius (ρ): Defined as the reversed curvature (1/curvature).

Figure 2.6a illustrates one isolated defect extracted from CD4 shrinkage classification with its contour outline. Figure 2.6b represents the curvature values profile along the contour, starting from the point indicated in Figure 2.6a and running in the direction of arrows. The threshold of the 10% highest values (last decile) was considered as representative of the highest curvature to be taken into consideration in order to characterize fatigue failure susceptibility (Figure 2.6c).

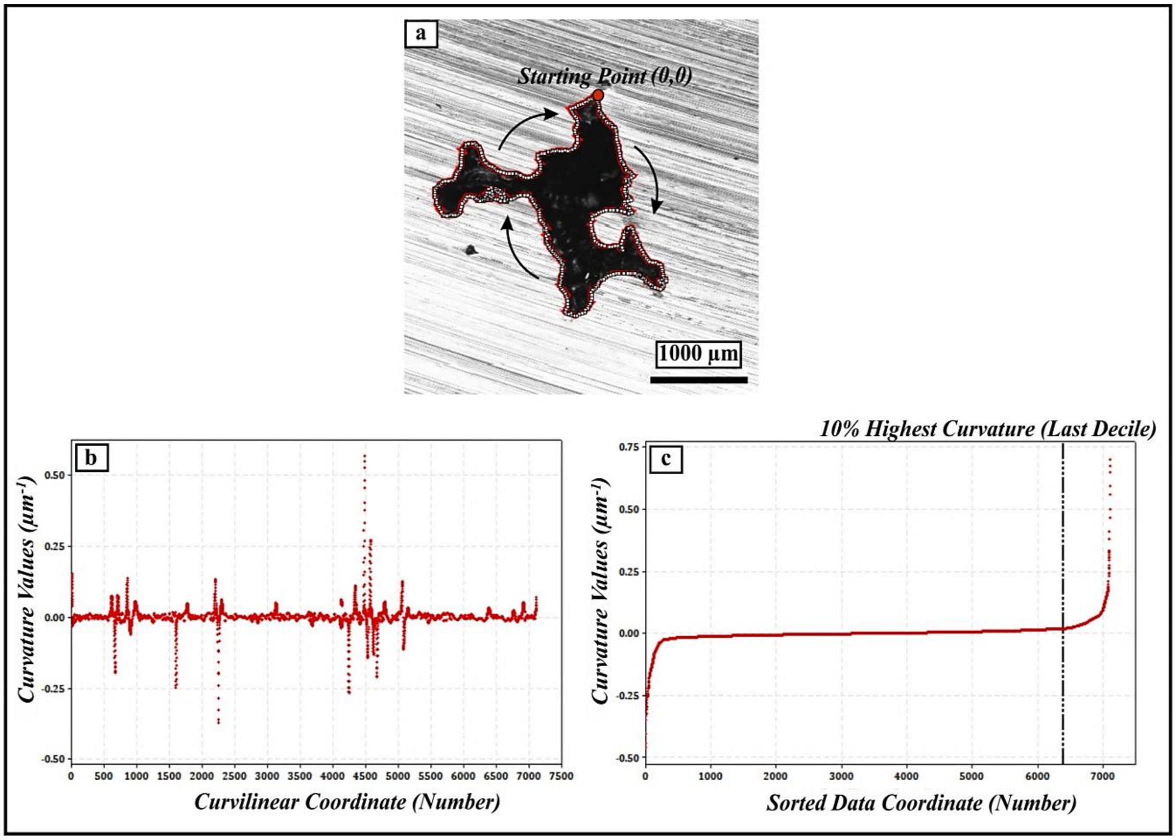

Figure 2.6 (a) Example of a defect from CD4 shrinkage code with its outlined contour, (b) Corresponding curvature profile, (c) 10% highest curvature values

2.4 Experimental results, data analysis and discussion

2.4.1 Microstructure characterization of solidification defects

Microstructure example after Vilella’s etching is presented in Figure 2.7. The metallographic characterization of as-cast normalized and tempered CA-6NM around the defect consisted mainly of the typical tempered lath martensite. Delta ferrite islands were dispersed in regions around the defects and sound parts away from the defects. However, delta ferrite was not formed as a continuous layer around the defects. This may suggest that there is no uniform segregation around the defects. Some researchers support that the presence of delta ferrite decreases crack nucleation and crack propagation energy (Wang et al., 2010); therefore, segregated delta ferrite as a continuous layer could make the area around the defect more fragile under loading which is not the case in this study. The absence of segregation was supported by EDX analysis.

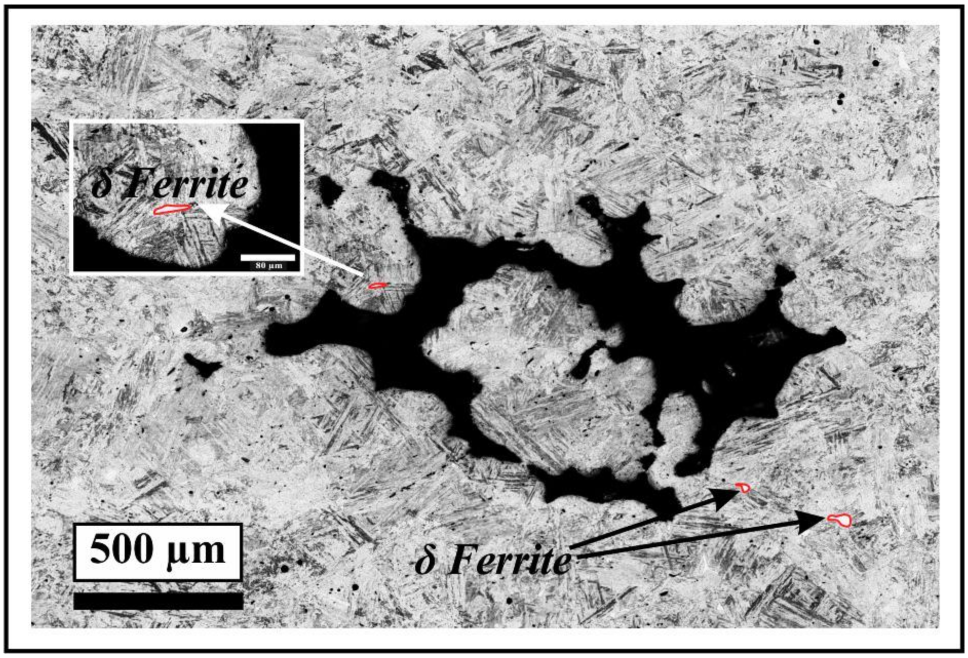

Figure 2.7 Martensite microstructure with small δ-ferrite islands around the defect

2.4.2 Macrostructure characterization and solidification defects

As mentioned before, the influence of a defect on fatigue life can be determined by its physical characteristics such as defect morphology and size (Vincent, Nadot, Nadot-Martin & Dragon, 2016; Murakami, 2002). From "Salami" cross-sectioning, the morphology and size of macro-defects were quantified to complement information for X-ray radiography standards.

2.4.2.1 Defect type and morphology

In radiography mapping, potential defects were coded as different shrinkage porosity classes with several severity levels. The cross-sections macrostructure of the defects confirmed their type as macro-shrinkage porosity with tortuous and irregular morphologies. Figure 2.8 illustrates the macrostructure of the shrinkage porosities with their highest severity levels found in this research. Fig. 8a represents individual shrinkage (CA) with a severity level of 3. Figure 2.8b shows grouped shrinkage (CB) with severity levels of 3. Figure 2.8c illustrates a denser type of grouped shrinkages (CD) with the highest severity level of 4. Although slices were taken at 1.5 to 2 mm intervals, defects are so dispersed in shape and size that they are difficult to be traced from one slice to another. Nevertheless, shrinkage porosities of higher severity levels displayed larger porosities and sharper endings.

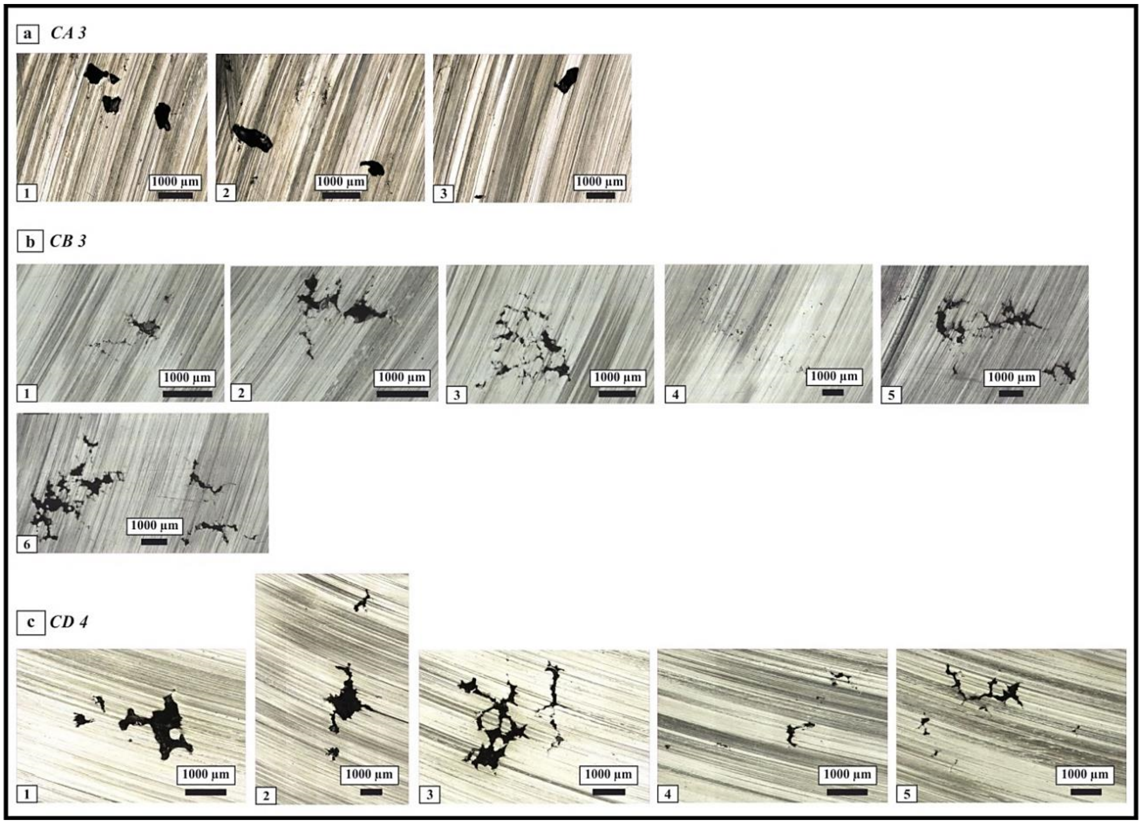

Figure 2.8 Macrostructure of different shrinkage porosity classes with the highest available severity levels (a) CA with a severity level of 3,
(c) CB with a severity level of 3, (c) CD with a severity level of 4

2.4.2.1.1 Sharpness

To quantify the sharp ending behavior, sharpness was specified as the defect length divided by the radius of the defect tip in each defect (L/ρ). In this research, the defect length is described as Feret’s diameter (L) and radius (ρ) is specified as the reversed curvature (1/curvature) (section 2.4). Considering extreme values in failure, corresponding curvatures were taken as 10% highest positive values in each isolated defect. It is remarkable to mention that theoretically when sharpness is more than 10 ($L/\rho > 10$), the defect root is very sharp and acts as a crack (Murakami, 2002).

Figure 2.9a and Figure 2.9b represent the distribution of Feret's diameter and radius values, respectively. These distributions were accomplished overall observed defects, without discrimination between shrinkage categories and severity levels. In this regard, 779 Feret’s diameter values and 746 radius values were processed. Because of eliminating concave corners, the quantity of radius data is less than Feret’s diameter. Table 2.4 reports Feret's diameter, radius, and sharpness values range.

As it is indicated in Figure 2.9a, a model using a 3-parameter Weibull distribution was fit to the cumulative distribution of Feret’s diameter values (c.f. equation 2.1). The parameters are defined as: α= shape parameter ($\alpha > 0$), β= scale parameter ($\beta > 0$), and γ= threshold parameter ($\gamma \leq x \leq +\infty$).

$$F_L(x) = 1 - \exp\left(-\left(\frac{x-\gamma}{\beta}\right)^{\alpha}\right) \tag{2.1}$$

Figure 2.9b represents the cumulative distribution of radius described by a Lognormal distribution with two parameters (c.f. equation 2.2). The parameters are defined as μ= location parameter, σ= scale parameter ($\sigma > 0$), and Φ denotes the Laplace integral.

$$F_\rho(x) = \Phi\left(\frac{\ln x - \mu}{\sigma}\right) \tag{2.2}$$

Besides, Figure 2.10 demonstrates the statistical dependence of sharpness measurements which is also well described by a double parameter Weibull distribution (shape (α) and scale (β)) (c.f. equation 2.3).

$$F_S(x)= 1- \exp\left(- \left(\frac{x}{\beta}\right)^{\alpha}\right) \tag{2.3}$$

This analysis showed that only 5.2% of sharpness values are less than 10 results in the fact that 94.8% of the defects in this research can be considered significantly elongated i.e., as cracks.

Table 2.4 Defects characteristics data range

Defect characteristic	**Range**
Feret's Diameter	**L=** 0.0395 - 7.7 mm
Radius	**ρ=** 0.0004 - 0.096 mm
Sharpness	**L/ρ=** 1.15 - 5646

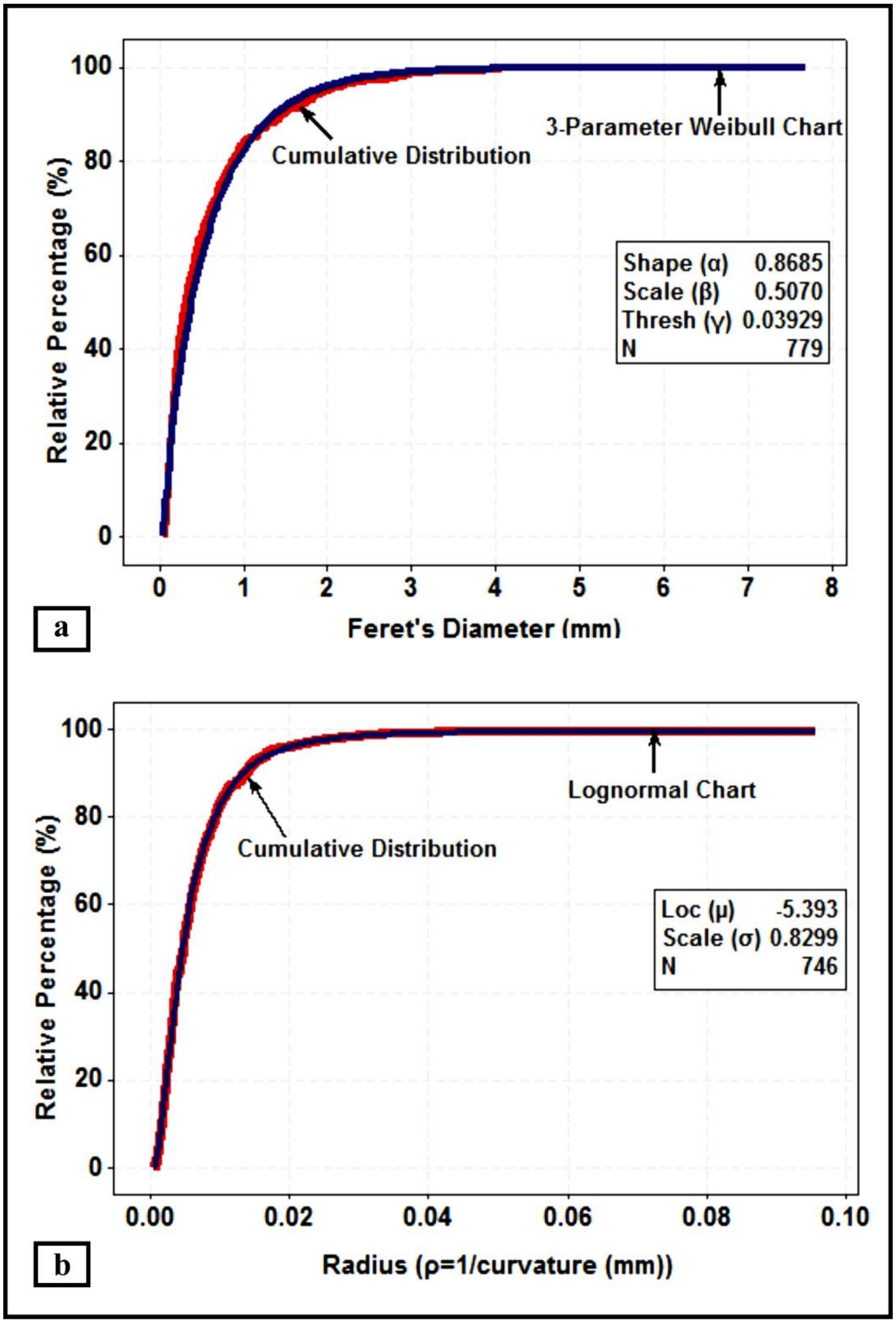

Figure 2.9 Showing distribution of (a) Feret’s diameter and (b) Radius

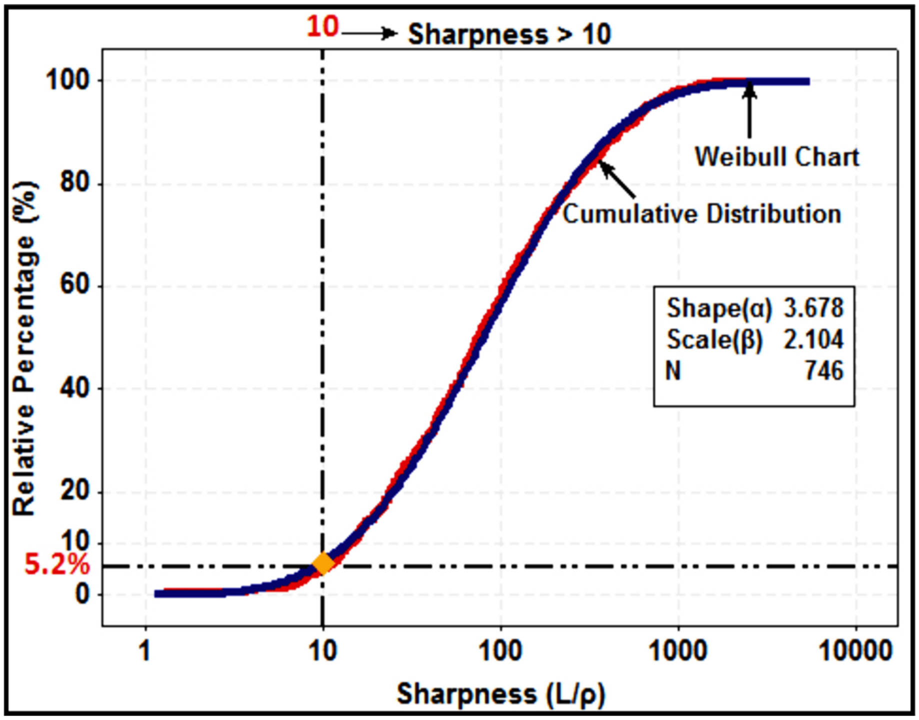

Figure 2.10 Cumulative distribution of sharpness values overlaid with a Weibull chart

2.4.2.2 Comparison between physical parameters and macro-shrinkage categories

In order to compare the behavior of various classifications of macro-shrinkage porosities, the correlation between shrinkage porosity classes and physical parameters of the defects such as morphology and size was studied. For this purpose, the highest severity level in each type of macro-shrinkages was taken. These levels of severity included enough statistical data to be quantified.

2.4.2.2.1 Curvature and macro-shrinkage categories

Since curvature has a direct correlation with sharpness, different shrinkage porosities were compared according to their curvature values. Figure 2.11 demonstrates the cumulative distribution of curvature values relevant to CA3, CB3, and CD4 macro-shrinkage porosities. As indicated in Figure 2.11, increasing the intensity of shrinkage classes results in higher curvature values (lower radius) and consequently sharper defects. Additionally, Table 2.5 specifies 10% of the highest curvature values related to various shrinkage porosity types. It can be seen that the 10% highest curvature value of CD4 is greater than CB3, and the CB3 value is larger than the CA3 quantity (**CD4** > **CB3** > **CA3**).

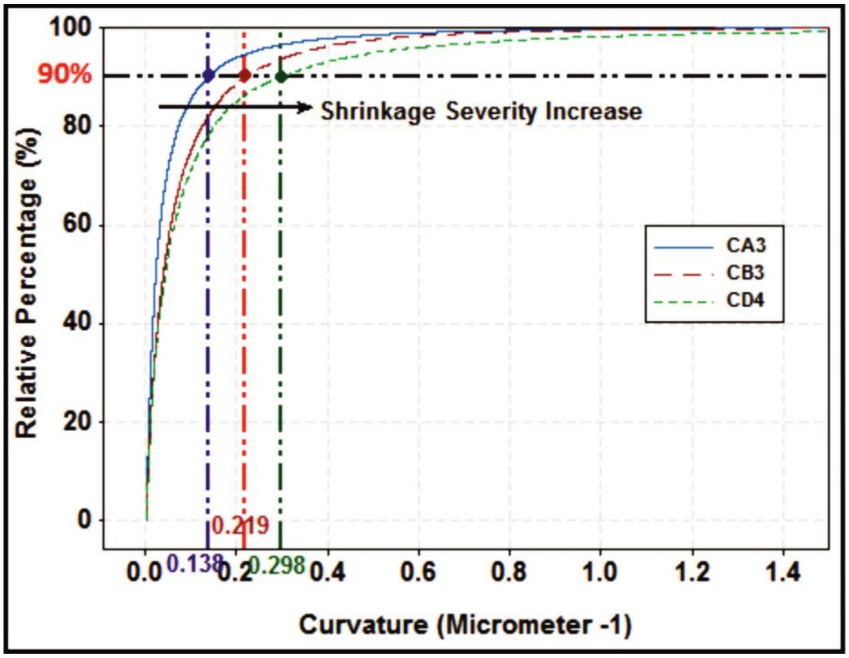

Figure 2.11 Cumulative distribution of curvature values in different macro-shrinkage porosity categories

Table 2.5 10% highest curvature values related to macro-shrinkage porosities

Macro-shrinkage porosity class	**10% highest curvature value**
CD4	**0.298 μm^{-1}**
CB3	**0.219 μm^{-1}**
CA3	**0.138 μm^{-1}**

2.4.2.2.2 Defect size and macro-shrinkage categories

Defect size is one of the most important parameters influencing the fatigue behavior of cast components. Murakami describes the area as a term of “effective area”. An effective area is estimated by considering a smooth contour that encompasses the original irregular shape. This effective area is substituted as “area” in the following discussion. Additionally, Murakami uses the square root of the projected defect area ($\sqrt{area}$) as a representation of the defect dimension (Murakami, 2002; British Standards BS 7910, 2005).

In the current research, the area of each defect was defined as an ellipse that encircles the original shape of the defect and they were measured by the shape analysis Fiji software described in section 2.3.4.

As suggested by Murakami, the square root of the area was plotted for each macro-shrinkage category and illustrated in Figure 2.12. As it is shown, statistical data related to CA3 (with 120 defects) and CB3 (with 302 defects) did not show a considerable difference between these categories, but CD4 (with 232 defects) displayed a higher quantity in the square root of the area. Consequently, the distribution of data showed a general trend that the more severe the shrinkage porosity, the higher the square root of the area. The data can be demonstrated as a probability density function of the 3-parameter Weibull distribution (c.f. equation 2.4).

It is noteworthy to mention that this analysis is helpful when using the Kitagawa-Takahashi type diagram with a data set corresponding to fatigue tests for CA-6NM cast alloys.

$$f_{\sqrt{area}}(x)= \frac{\alpha}{\beta} \left(\frac{x-\gamma}{\beta}\right)^{\alpha-1} \exp\left(- \left(\frac{x-\gamma}{\beta}\right)^{\alpha}\right) \tag{2.4}$$

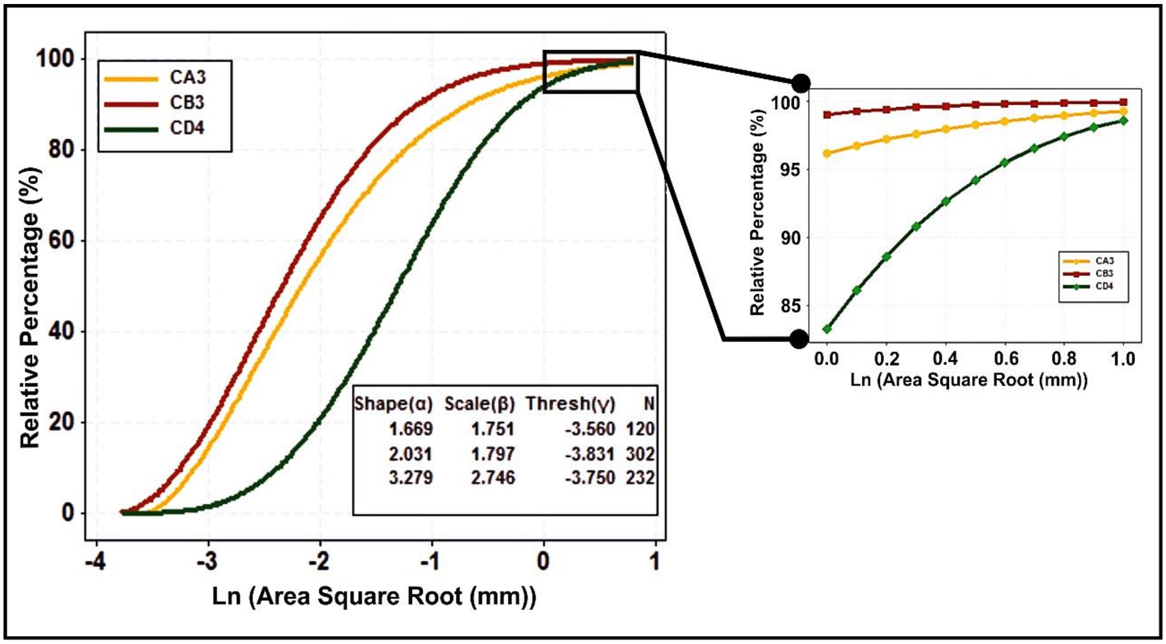

Figure 2.12 Correlation between area square root and shrinkage categories

2.5 Conclusions

Evaluating the macro-defects in the cast components was the main purpose of this research. The “Salami” cross-sectioning and later on shape analysis procedure were carried out to characterize the macrostructure of cast shrinkage porosities. The microstructure of solidification defects was also investigated by metallographic evaluation. The results achieved in this research are summarized as follows:

- “Salami” cross-sectioning provides complementary information of indicated macro-defects besides the interpreted information achieved from X-ray radiography images.

- “Salami” cross-sectioning confirms the defects indicated in X-ray radiography as different types of macro-shrinkage porosities.

- Using shape analysis software, macro-shrinkage porosities showed very sharp endings. According to the cumulative distribution of sharpness measurements obtained by metallography, almost 95% of defects demonstrate sharpness values higher than 10 ($L/\rho>10$) and consequently, their fatigue behavior can be treated as cracks (Murakami, 2002).

- Macro-shrinkage porosities of different categories with higher severity levels represent systematically sharper endings and potentially more deleterious defects.

- Macro-shrinkage porosities of more severe categories (such as CD4) present a higher probability of finding defects with larger Murakami's parameter ($\sqrt{area}$) and more severe potential damage.

- Chemical segregation around defects was investigated microscopically. This examination did not display phase segregation around the defects. The absence of segregation was supported by EDX analysis.

2.6 Expected future works

The current research has been performed on only 1 cast turbine blade; a larger spectrum of specimens would have allowed the comparison of the performance of many casting processes in terms of defect density and severity. This will be subject to future works.

2.7 Acknowledgments

The authors wish to acknowledge the help and facilities provided by Institut de recherche d'Hydro-Québec (IREQ) and Alstom Canada Inc. The writers also would like to thank Dr. Demartonne Ramos Franca (ÉTS) for helpful discussions and valuable revisions. The useful counsel by Prof. Antoine Tahan (ÉTS) is gratefully appreciated as well. Furthermore, the precious technical assistance by E. Dallaire and A. Lapointe at IREQ is thankfully acknowledged. The authors are also grateful for helpful discussions and counsel by B. Papillon and M. Sabourin from Alstom. Moreover, the X-ray radiography analysis performed by N. Giguère at CMQ (Centre de Métallurgie du Québec) is appreciatively acknowledged.

This project was financially supported by Alstom Canada; Hydro-Québec; Mitacs; Consortium de recherche en fabrication et réparation des roues d’eau (CReFaRRE); and the Natural Sciences and Engineering Research Council of Canada (NSERC).

CHAPTER 3

TWO DIMENSIONAL (2D) FRACTOGRAPHIC CHARACTERIZATION OF SHRINKAGE POROSITY AND FATIGUE PROPERTIES OF CAST CA-6NM MARTENSITIC STAINLESS STEEL

3.1 Introduction

The fracture surface is generally the first and only evidence of the crack initiation site(s) for the fatigue damage mechanism. Therefore, characterizing the fracture surface of ruptured samples in a scanning electron microscope (SEM) is a popular and classic method to relate the fatigue properties of the cast metals/alloys to the presence of defects. In two-dimensional (2D) fractographic analysis, both qualitative and quantitative information of the largest defects can be acquired only based on the fracture surface evaluation.

Concisely, the main objectives of this chapter are: (1) to apply SEM fractographic evaluation and identify the features (i.e., type, morphology, size and position) of the defects serving as the origin(s) of the fatigue failure; (2) to investigate the impact of defect size and position on the distribution of the fatigue life in cast CA-6NM martensitic stainless steel; (3) to verify linear elastic fracture mechanics (LEFM) conditions. This confirmation was performed to predict the Kitagawa-Takahashi diagram for the finite life (i.e., the target life of 25000 cycles) of the Francis turbine blade. Besides, the geometrical factor ($Y(a)$) variation in proportion to the size of the defects during fatigue crack growth evolution was calculated and modelled. Eventually, this model was applied to compute the initial size of the shrinkage porosities (i.e. the fatigue crack initiation site) and compare it with measured data.

It is worth noting that the primary study of fatigue properties presented in this chapter only contains the fractographic analyses performed on post-mortem specimens. In the next chapter, further experiments will be applied on a pristine fatigue sample that was initially scanned by the XCT tomography technique and then cycled.

3.2 Experimental procedure

3.2.1 Material

The material under this section of the investigation was extracted from the same CA-6NM cast blade that was studied in the previous chapter. Fatigue testing specimens were prepared from sound areas (material without visible indications but with probable defects) of the blade. As mentioned earlier, the evaluation of indications was performed by a certified technician based on a comparison of radiographs taken from the blade with a set of reference radiographic images. Figure 3.1 highlights the sound (i.e., OK) areas as well as the distribution of the regions with potential flaws that are identified as radiographic codes and their corresponding severity level.

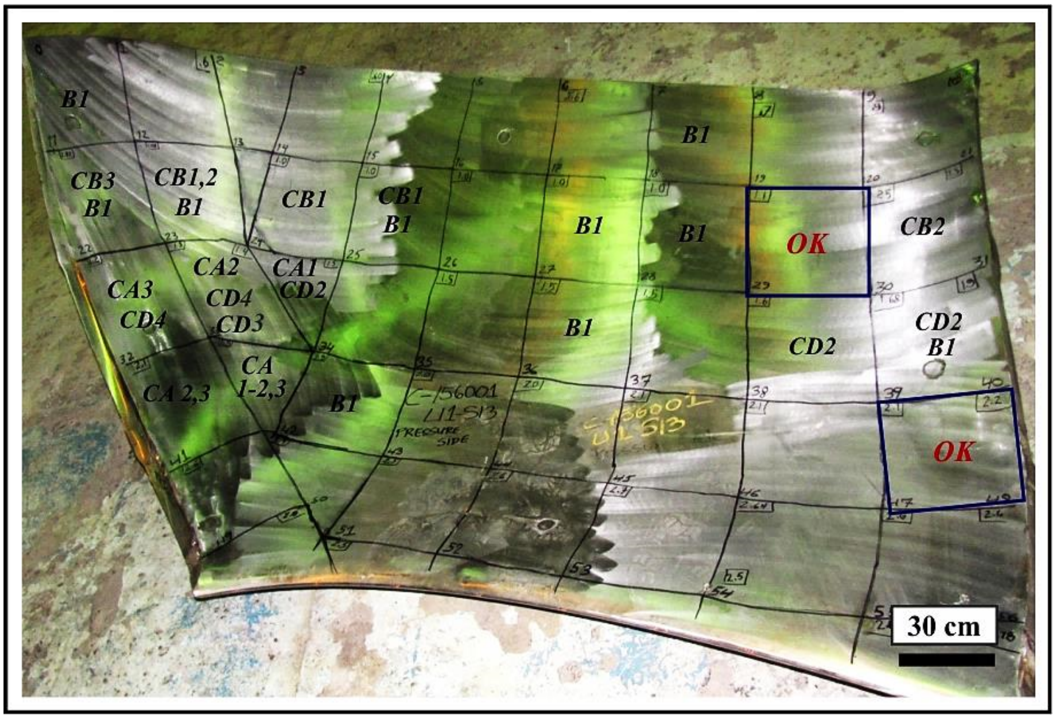

Figure 3.1 Blade image showing the distribution of indications according to (ASTM E446-98, 2004 & ASTM E186-98, 2004), and areas without visible indications

3.2.2 Standard fatigue specimen

Fatigue specimens were designed according to ASTM E466 norms (ASTM Standard E466-07, 2007). The configuration and dimensions of a standard fatigue sample are displayed in Figure 3.2. The drawn cutting schemes on two cast blocks are also shown in Figure 3.3. Using these cutting sketches, fatigue samples were extracted and turned to obtain a set of 22 samples.

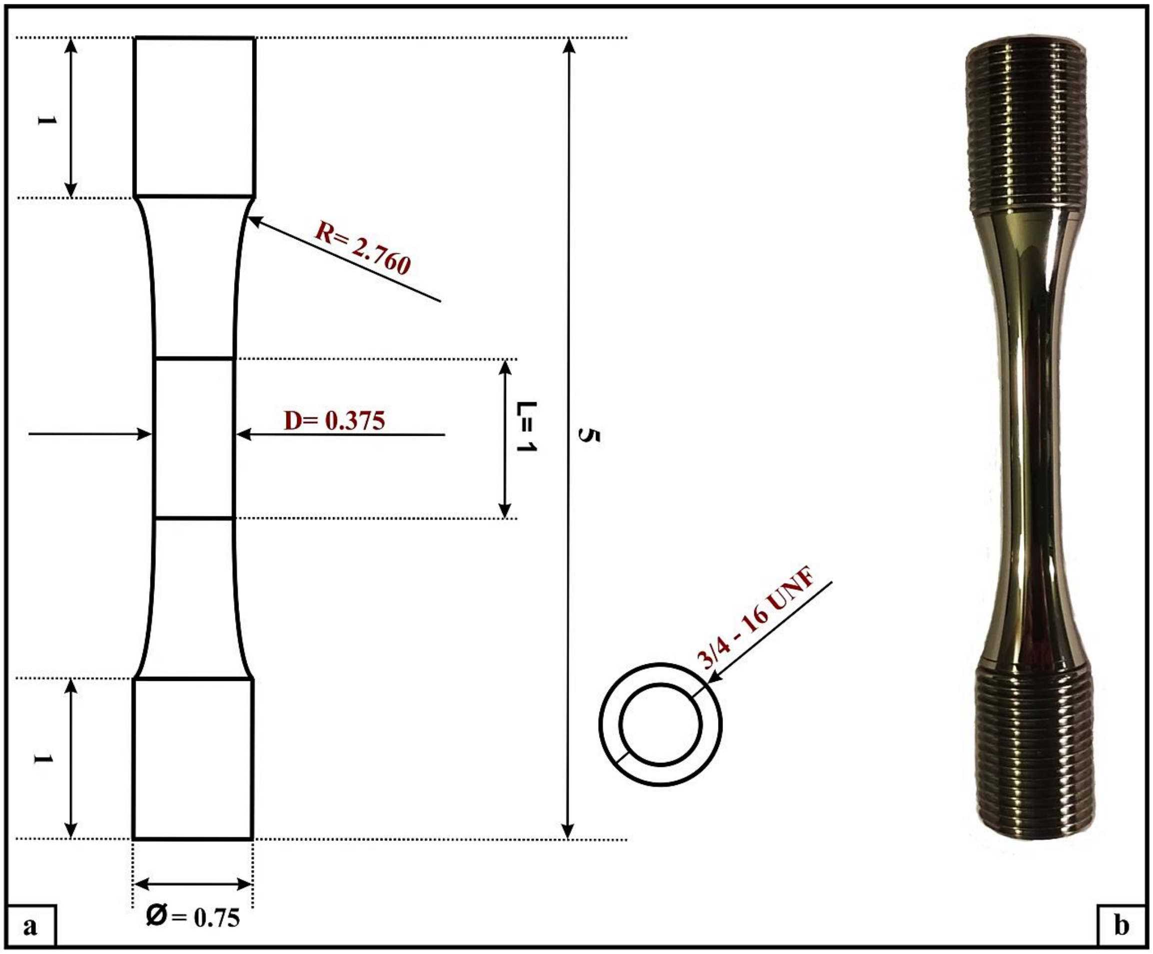

Figure 3.2 (a) Sketch of the standard cylindrical fatigue specimen (all dimensions are in inches (in.)) (ASTM E466, 2007), (b) Machined and polished fatigue sample

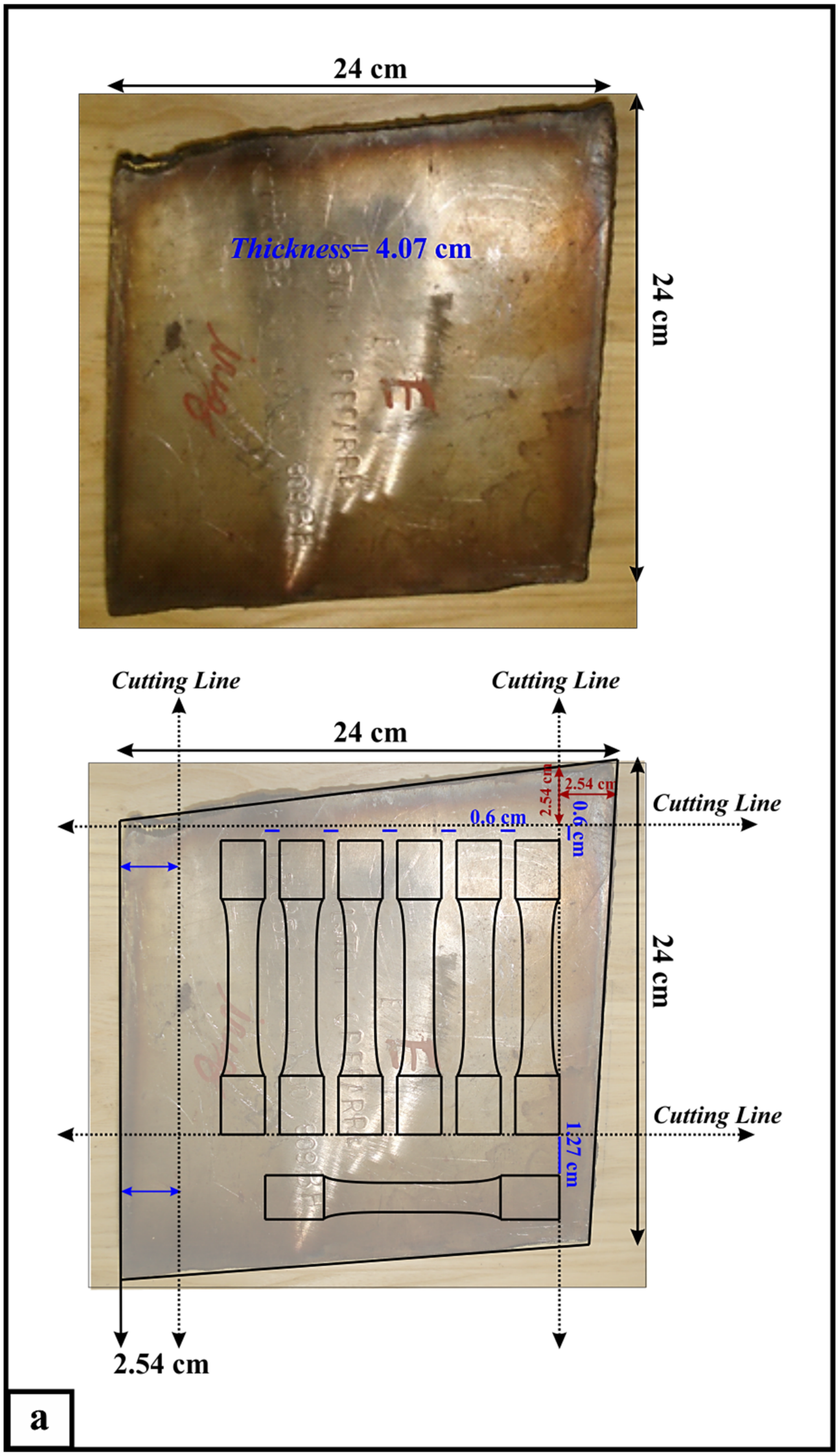

Figure 3.3a Cutting scheme representing the distribution of the fatigue samples over the first cast block providing seven samples

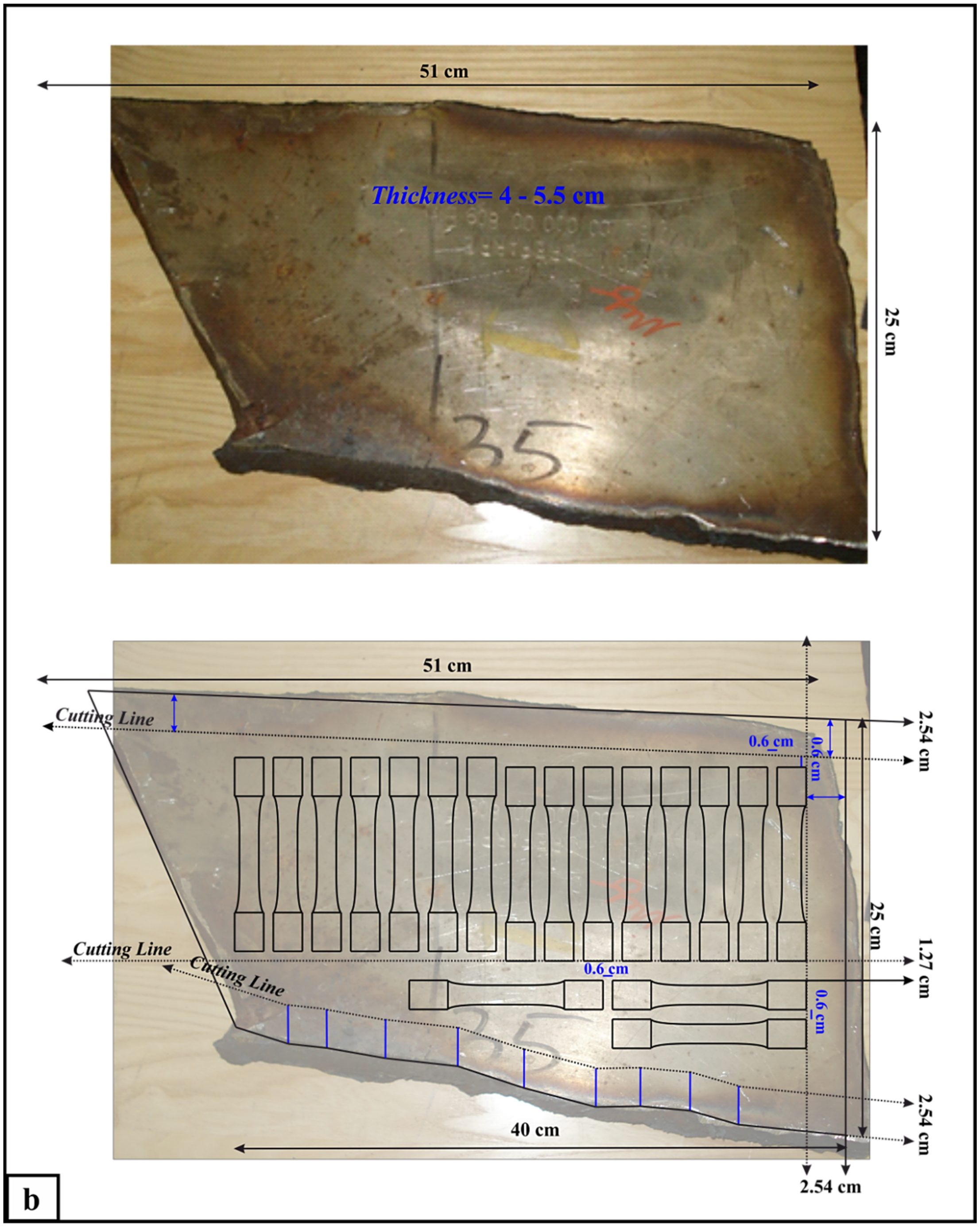

Figure 3.3b Cutting scheme representing the distribution of the fatigue samples over the second cast block providing eighteen samples

3.2.3 X-ray radiography

High-resolution radiographic images were provided for all machined fatigue samples to reveal internal defects that could be invisible during the inspection of thicker sections of the blade (Figure 3.4). Outlined white circles highlight detected internal discontinuities on the full-scale radiographs. Image quality indicators (IQI) are also shown in Figure 3.4(c) and (d) to demonstrate that the image quality comprises the ASTM standards. The X-ray radiography was accomplished with a set of parameters listed in Table 3.1.

Table 3.1 X-ray radiography setting parameters

Distance from tube to film	Voltage	Current	Focal spot	Exposure time	Film type
457.2 mm (18 inches)	160 kV	5 mA	3 mm	35 seconds	Kodak T2000

3.2.4 Fatigue sample preparation

Following conducting the X-ray radiography imaging, metallographic polishing of fatigue specimens was performed. To avoid surface roughness that can bias fatigue results, all fatigue specimens were polished gently and carefully. Using a polishing lathe, grinding and polishing steps were conducted manually at a fixed speed of 1000 rpm. Fatigue specimens were ground with 220, 320, 500, 800, and 1200 SiC abrasive grinding papers followed by polishing with 6, 3, and 1 μm diamond suspensions with an alcohol-based lubricant used on silk polishing pads. Between each step of preparation, to prevent transferring any kind of contaminations or coarse particles of grinding papers, samples were washed thoroughly, immerged in an ethanol ultrasonic bath for 5 to 10 minutes, and air-dried. Similarly, the polishing set-up was meticulously cleaned. After each step of preparation, the diameter of the gauge length was measured at several locations to verify the uniformity of polishing.

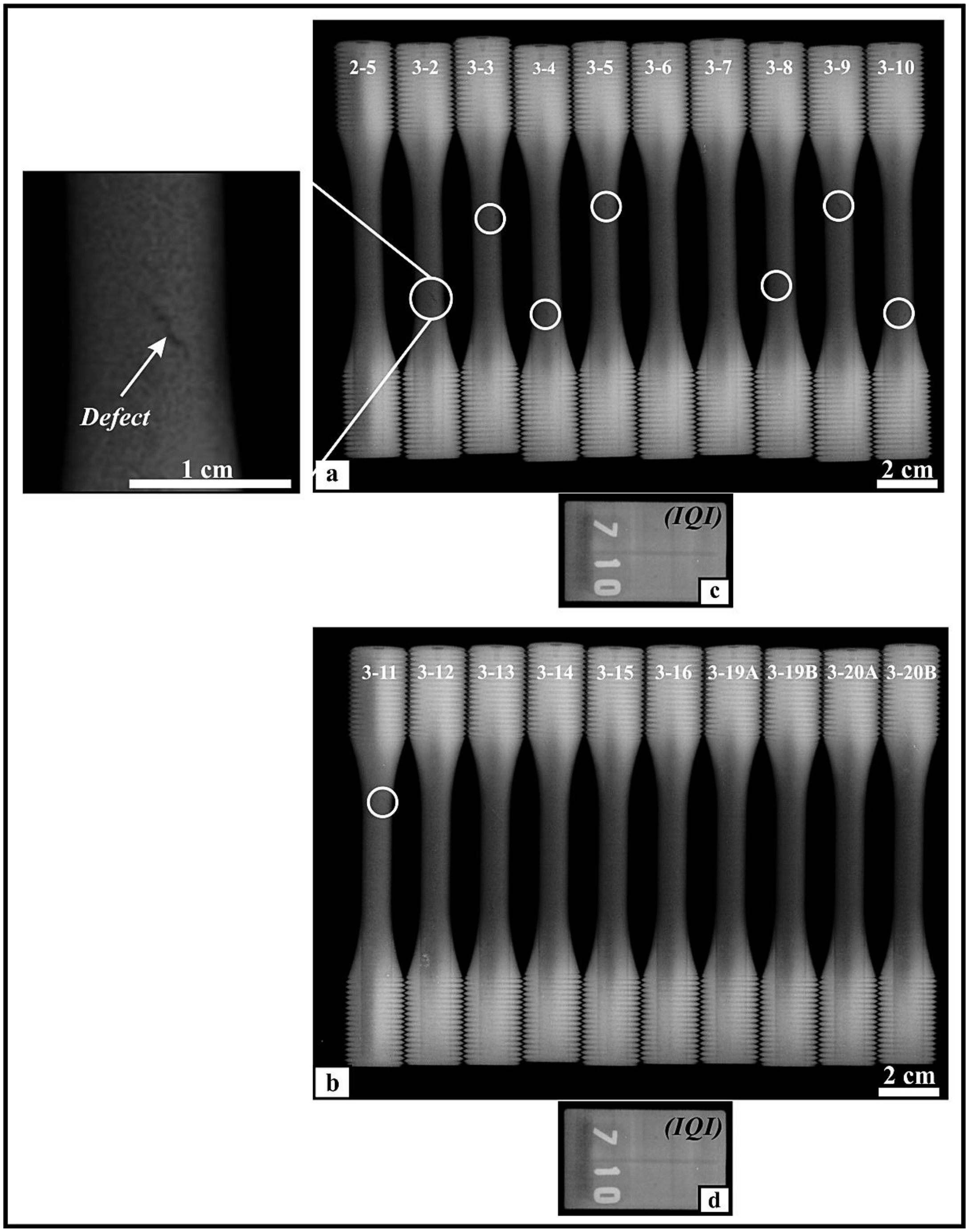

Figure 3.4 (a), (b) Radiographic images showing internal defects within the fatigue specimens, (c), (d) Image Quality Indicator (IQI)

3.2.5 Residual stress measurement

Machining can induce residual stress on the fatigue specimen surface and therefore alter the fatigue results. Based on that, the residual stress was evaluated on the as-machined and afterwards on the polished surfaces of fatigue samples.

A Pulstec μ-X360 portable X-ray residual stress analyzer with an X-ray chromium tube was used for this purpose. Axial stress was considered based on the fatigue loading direction. The residual stress was measured at three different points (point 1, point 2, and point 3) along the loading axis, fatigue samples gauge length, and three different angular locations which were regularly spaced (0 degrees, 120 degrees, and 240 degrees) (Figure 3.5).

The residual stress of the as-machined fatigue specimens was in the range of -500 MPa. After conducting the grinding process (cf. section 3.2.4), the stress value was reduced to about -125 MPa. Showing that grinding/polishing is capable of decreasing surface residual stress, samples were further polished using 6, 3, and 1 μm diamond suspensions (cf. section 3.2.4).

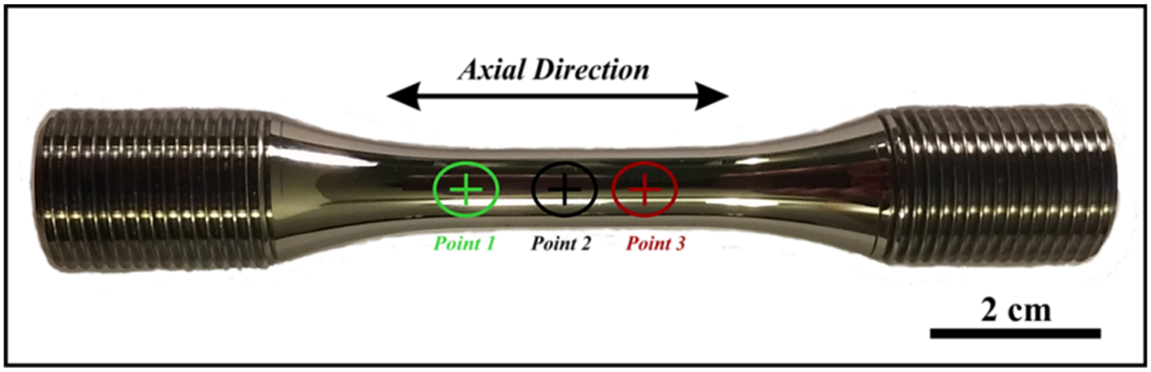

Figure 3.5 Illustration of the residual stress measurement points at one of the angular locations on the fatigue specimen surface

3.2.6 Fatigue testing (LCF)

Following conducting the residual stress measurement, low-cycle fatigue (LCF) tests were conducted on a set of 22 prepared fatigue samples. Using an MTS machine equipped with hydraulically operated wedge grips (Figure 3.6), all fatigue tests were performed under uniaxial tension-tension loading at room temperature (between 22 °C and 25 °C) in ambient air with a stress ratio of R = 0.1 exerted in a sinusoidal waveform, a frequency of 5 Hz and maximum applied stress of 688 MPa. Maximum applied stress was initially selected according to the representative tensile properties for the standard cast CA-6NM martensitic stainless steel that is air-cooled from > 1900 °F and tempered in the range of 1100 °F to 1150 °F (Table 1.3; Figure 1.3 & Steel casting handbook, 2004).

During fatigue testing, the MTS software automatically recorded the running time, the axial force and the number of cycles before complete fracture. In this research, all fatigue samples failed in their gauge length.

These tests aimed to evaluate the fatigue life data and to show the effect of casting defects on the fatigue life of cast blades in Francis turbine runners. Hydraulic turbines are expected to remain functional for about seventy years (approximate lifetime of a typical hydraulic turbine). Based on the number of start-stop cycles experienced by the runner within this length of time, the target life is about 25000 cycles. For those fatigue samples that resisted 25000 cycles, the fatigue test continued until the complete failure.

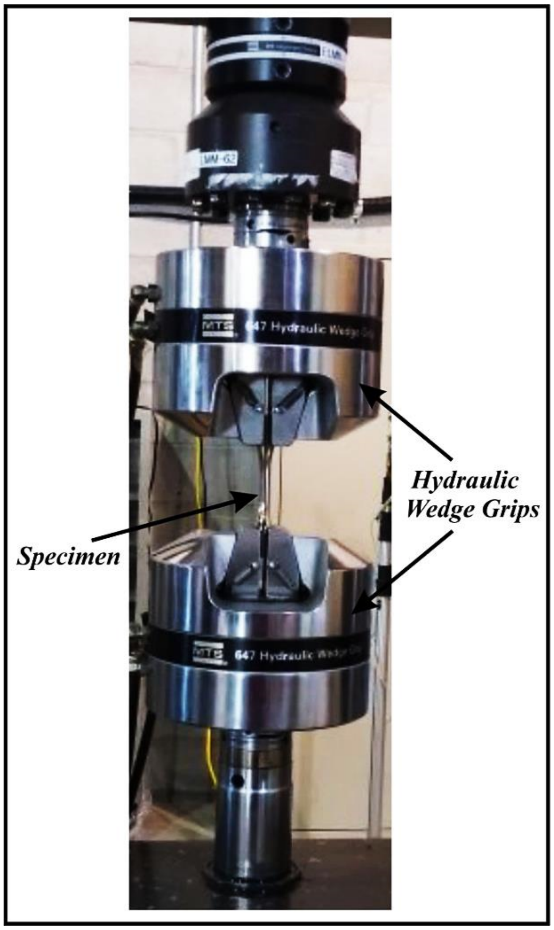

Figure 3.6 MTS fatigue testing machine

3.2.7 Fractography

SEM fractography is commonly applied to obtain both qualitative and quantitative data. This information is used to attain a more precise failure analysis and to specify which defect(s) act as fatigue crack initiation sites.

Following that, a Hitachi S-3700 N scanning electron microscopy (SEM) at 15 Kev was used for fractographic observations. All test coupons were sectioned from the ruptured fatigue specimens and mounted carefully for evaluation. 44 test coupons (i.e., both broken halves of

22 fatigue samples) were characterized. To protect fracture surface information, each half was kept separately.

Figure 3.7 indicates a typical fatigue fracture surface that consists of three principal fractographic features: (1) fatigue crack initiation site located and propagated in the area that contained "river lines" (i.e., fatigue striations), (2) rough region covered by dimples where the fracture damage has occurred in a ductile way and the cross-section of the sample cannot endure the applied load anymore, (3) final catastrophic fracture region (Ammar, 2006).

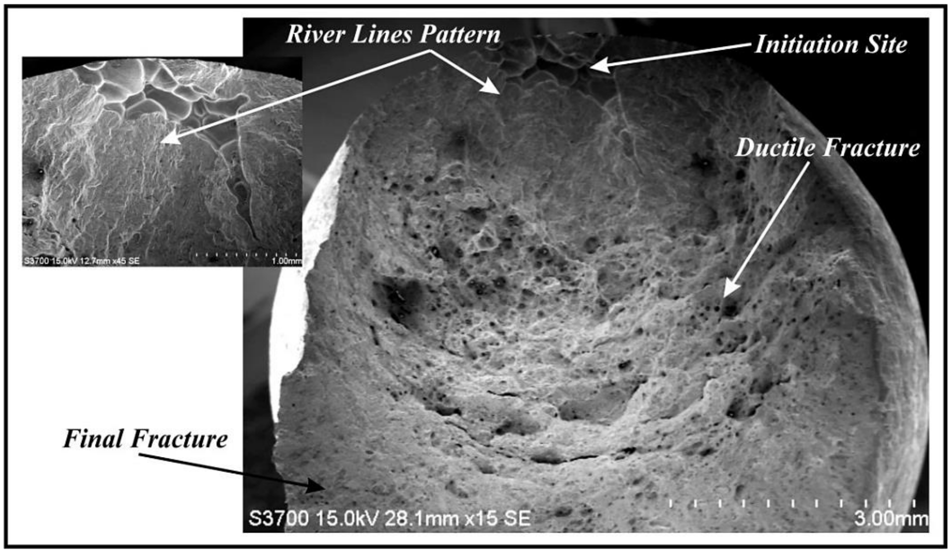

Figure 3.7 Fatigue failure surface of cast CA-6NM (sample #3-16)
showing the surface porosity associated with the crack initiation site

3.2.8 Defect size characterization method

After SEM fractographic evaluation, fatigue fracture surfaces were characterized using the open-source image processing software Fiji, ImageJ (cf. chapter 2). Quantitative measurement of the sizing parameter was applied to casting defects which were the origin of the failure. This analysis was carried out on both fracture halves of each tested sample (Figure 3.8).

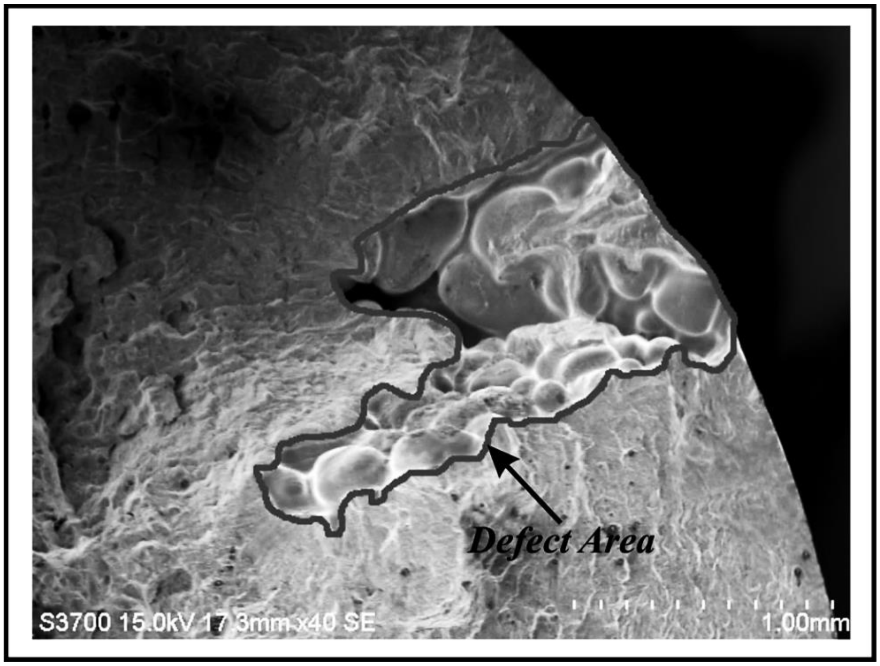

Figure 3.8 Characterization of defect size on the fracture surface of cast CA-6NM (sample #3-20A)

3.3 Experimental results, data analysis and discussion

3.3.1 Characterization of defect position, morphology and size

The fractographic results confirmed that in all fatigue samples (i.e., 100% of the samples tested), the failure originated from a surface defect on the sample cross-section (Figure 3.9 & Annex I, Figure I). Figure 3.9 exemplifies the fracture surface of two random fatigue samples. A complete set of fractographic images related to all 22 tested samples is presented in APPENDIX I, Figure I. In this figure, the numbering of images is in the order of the number of cycles to fatigue failure (see Table 3.3, second column).

The SEM fractographic results display that internal failure never occurred even though some specimens contained larger internal defects (see Figure 3.10 & Table 3.2). Also, all observed defects had tortuous and irregular morphologies, indicating that they are shrinkage porosities resulting from the casting process (Figure 3.9 & APPENDIX I, Figure I). Accordingly, shrinkage porosities are given particular attention in this study as they play a significant role in influencing the fatigue performance of cast low carbon CA-6NM martensitic stainless steel.

As mentioned earlier in chapter 1 (cf. section 1.9.3), it is quite challenging to define the sizing parameter of the defects with elongated and intricate shapes. Therefore, Murakami's geometrical parameter ($\sqrt{area}$) (i.e., ~ crack length) was applied to simplify the definition of the dimension of such defects.

Because defects with maximum size will end up being more critical and the failure in cast components is an extreme value related phenomenon (cf. chapter 2); therefore in each fatigue sample, the largest shrinkage porosity initiating the fatigue crack was taken into account to define Murakami's geometrical parameter ($\sqrt{area}$).

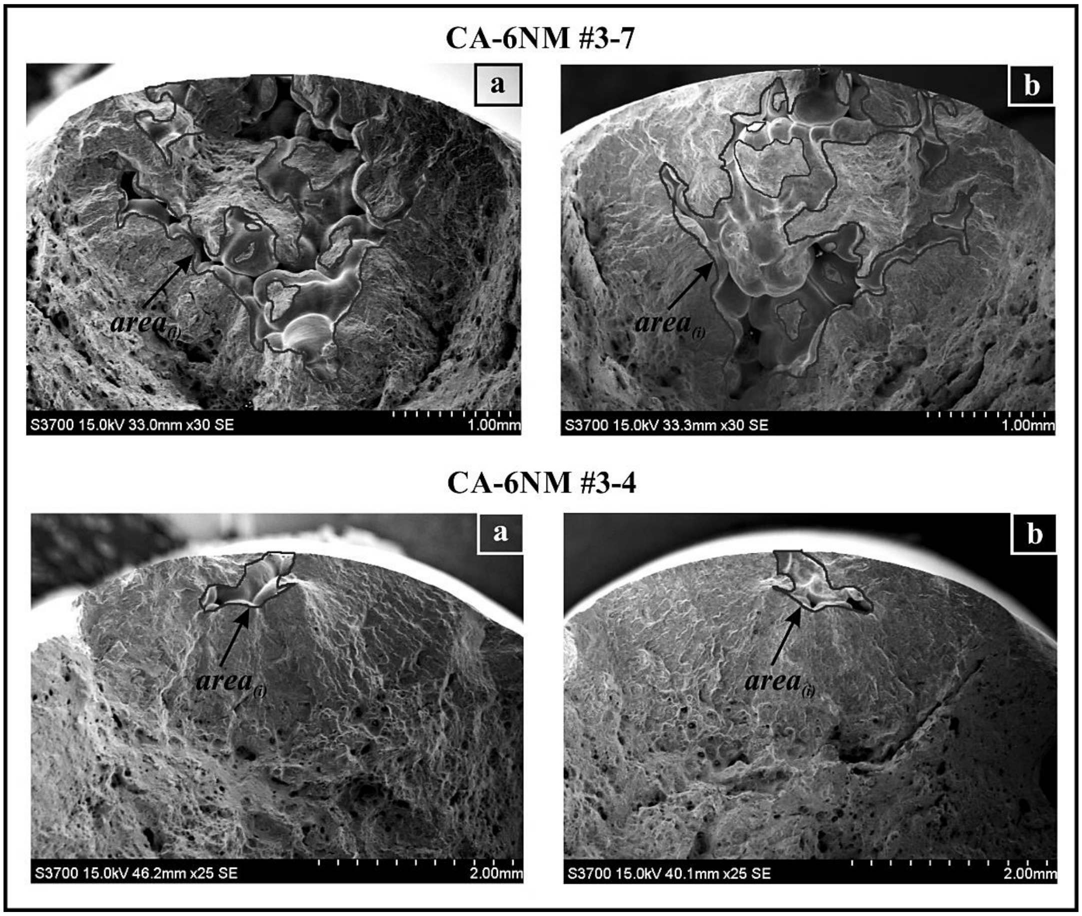

Figure 3.9 (a), (b) Area measurement of macro-shrinkage porosities (i.e., the origins of fatigue failure) on both broken halves of tested samples

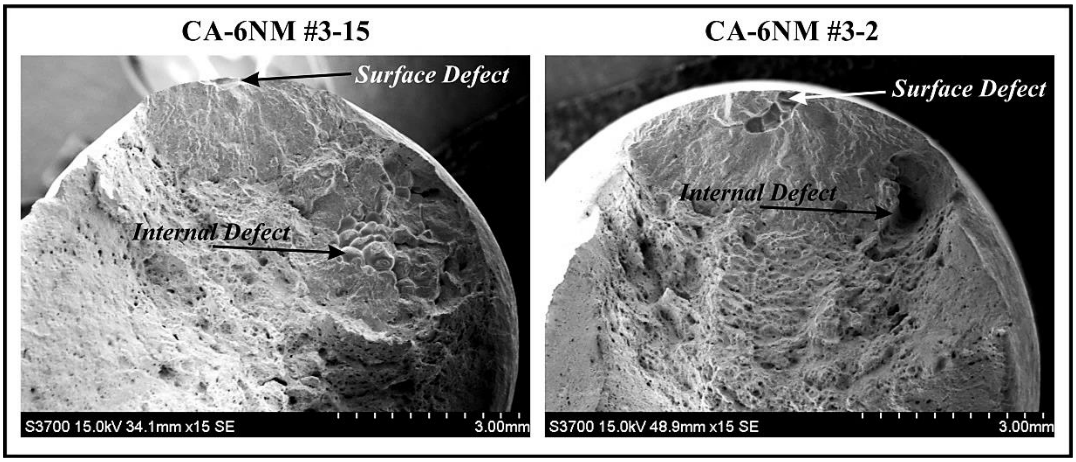

Figure 3.10 Showing two examples of cast CA-6NM fatigue fracture surface containing a large internal porosity and a relatively small surface porosity

Table 3.2 Comparing fractographic analysis of surface porosities vs. internal porosities

Sample number	**Cycles to fracture (N_f)**	**Surface porosity size $\sqrt{area_{(i)}}$ (mm)**	**Internal porosity size $\sqrt{area_{(i)}}$ (mm)**
CA-6NM #3-15	21056	0.37	1.32
CA-6NM #3-2	23377	0.62	1.15

Generally, when the size of surface porosity increases, a noticeable reduction in fatigue life occurs. The possible cause is the stress concentration which is higher at the surface defect and leads to a stress gradient between the surface and the center of the specimen. Accordingly, larger surface porosities increase the stress concentration value and therefore the stress gradient. This stress gradient is a driving force for crack propagation toward the sample interior and shortening the fatigue life of the material.

A precise analysis of the fractographic data in Table 3.3 and Figure 3.11 demonstrates that the fatigue life of the stressed specimens containing shrinkage porosities diminishes with an increase in the size of the defect. In this regard, using a nonlinear fitting method, the correlation between fatigue life (i.e., the number of cycles to complete fracture) and the size of shrinkage porosity was quantitatively formulated by a negative exponential function:

$$N_f = 1.3607 * (\sqrt{area})^{-0.898} * 10^4 \tag{3.1}$$

where N_f is the fatigue life (cycles) and $\sqrt{area}$ is the size of shrinkage porosity (mm).

The fatigue life curve in Figure 3.11 represents that the fatigue performance is sensitive to the presence of shrinkage porosities so that even a small defect can reduce the fatigue life substantially. Nevertheless, there exists a scatter in the statistical distribution of the fatigue life and it is not always straightforward to correlate the fatigue life and the size of shrinkage porosities. Comparing the last two lines of Table 3.3 (i.e., sample CA-6NM #3-6 and CA-

6NM 3-19B)) clarifies that. The reasons for this scatter and sometimes poor correlation can be:

- The distribution of shrinkage porosities is variable from one sample to the next.
- The fractographic evaluation only reveals a shrinkage porosity which is critical for the porosity distribution/population of that specific perused sample.
- As mentioned earlier, fatigue fractures are initiated at casting shrinkage porosities that are located at or near the free surface of specimens. This phenomenon might result in significantly shorter fatigue life.
- The size and morphology of shrinkage porosities observed on fracture surfaces are scattered too.

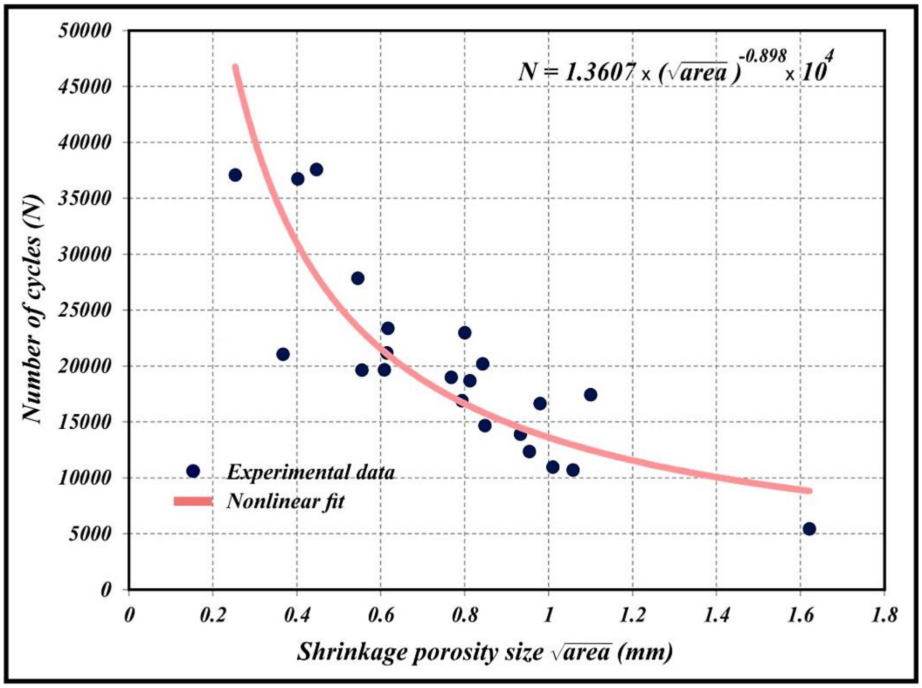

Figure 3.11 The effect of shrinkage porosity size on the fatigue life of cast CA-6NM martensitic stainless steel

3.3.2 Kitagawa-Takahashi diagram and calculation of geometrical correction factor ($\bar{Y}(a)$)

As hypothesized in the previous chapter, in this research, macro-shrinkage porosities can be treated as cracks owing to their high sharpness. Besides, the LEFM model is valid only for long cracks and for the components that behave mainly elastic under fatigue loading. Therefore, under LEFM conditions, the Kitagawa-Takahashi diagram can be a useful tool to define the safe design zone of non-propagating fatigue crack (see also section 1.9).

Murakami and Endo developed the Kitagawa model by replacing the initial size of the defect (i.e., crack length (a_0)) with Murakami's geometrical parameter ($\sqrt{area_{(0)}}$) (cf. section 1.10.3). Murakami's parameter is a more practical way to interpret the shape and size of defects with complex configurations.

Considering the above-mentioned modification and according to the LEFM relations, the correlation between the stress intensity factor range and the applied stress range (equation 1.12) can be reformulated as equation 3.2:

$$\Delta K_{th} = \Delta\sigma_{fl} * \sqrt{\pi \sqrt{area_{(0)}}} * Y(a) \tag{3.2}$$

where ΔK_{th} is the threshold stress intensity factor range for long crack propagation, $\Delta\sigma_{fl}$ is the material fatigue limit independent from defects and $Y(a)$ is the Murakami's shape factor. Depending on the defect position, Murakami introduced a shape factor, $Y(a)$, of 0.5 for internal defects and 0.65 for surface defects (Murakami, 2002).

To plot the Kitagawa-Takahashi diagram, at first, it was required to calculate the geometrical parameter $Y(a)$ for each fractured fatigue sample. $Y(a)$ was studied by applying two methods namely the back-tracking method and Forman & Shivakumar solution which is a model to evaluate the geometrical correction factor ($Y(a)$) for surface cracks in a solid cylinder exposed to tension loading.

3.3.2.1 Back-tracking method

Estimation of the shape factor, $Y(a)$, for each specimen requires several elements: (1) the stress range which was defined as the stress range applied in fatigue testing, (2) the initial size of the crack ($\sqrt{area_{(i)}}$) (i.e., the size of the initiation site), (3) the final size of the crack ($\sqrt{area_{(f)}}$), (4) the Paris law constants obtained in a previous investigation on fatigue crack propagation of cast CA-6NM martensitic stainless steel in the air with a stress ratio of R = 0.1 (Figure 3.12) (Thibault et al, 2011), and (5) the number of cycles to complete fracture (N_f). The parameter set employed to compute the geometric factor $Y(a)$ and to plot the Kitagawa-Takahashi diagram is given in Table 3.4.

Considering the crack growth behavior of CA-6NM ($da/dN = 2.2 * 10^{-9} * \Delta K^{3.15}$), a crack with an initial size of ($\sqrt{area_{(i)}}$) propagated to final size ($\sqrt{area_{(f)}}$) in a specific number of cycles (N_f) and the average value of the geometrical parameter ($\bar{Y}(a)$) was adjusted for each fatigue sample manually. The calculated data for average shape factor $Y(a)$ are indicated in Table 3.3, the sixth column named $\bar{Y}(a)$. These results demonstrate that the considered average shape factor is ranging from **0.67** to **0.87**.

To ensure, before plotting the Kitagawa-Takahashi diagram, the LEFM condition was verified. For this purpose, equation 1.10 was applied to the largest shrinkage porosity that caused fatigue failure in this study. In equation 1.10, the K_{max} (K_I) is equal to 1.1 ΔK since the ratio K_{min}/K_{max} for all the fatigue tests was 0.1, σ_0 is the maximum applied stress and $Y(a)$ is the $\bar{Y}(a)$ of the studied sample. The aforesaid and other required parameters are given in Table 3.3 (sample CA-6NM #3-7) and Table 3.4:

plane stress condition: $a_1 \geq 2.5 \left(\frac{K_I}{\sigma_0}\right)^2 \quad \rightarrow \quad D - \sqrt{area_{(i)}} \geq 2.5 \left(\frac{K_I}{\sigma_0}\right)^2 \quad \rightarrow$

$$D - \sqrt{area_{(i)}} \geq 2.5 * \left(\frac{1.1 * Y(a) * \Delta\sigma * \sqrt{\pi * \sqrt{area_{(i)}}}}{\sigma_0}\right)^2 \tag{3.3}$$

where a_1 is the distance between the crack tip and any of the other sample's surfaces ahead of the crack tip. "D" was defined as the fatigue sample diameter. The result is as follows:

$$D - \sqrt{area_{(i)}} = \mathbf{7.9\ mm} \geq 2.5 * \left(\frac{1.1 * Y(a) * \Delta\sigma * \sqrt{\pi * \sqrt{area_{(i)}}}}{\sigma_0}\right)^2 = \mathbf{7.01\ mm} \tag{3.4}$$

In the next step, to build the Kitagawa-Takahashi diagram three different values of *Y(a)* were selected from the data range mentioned above. The experimentally measured data were also superimposed to the diagram to fit the model and define the safe design zone (i.e., no fatigue failure). The Kitagawa diagram shows that the geometrical factor, *Y(a)*, of **0.85** was the best match describing the experimental fatigue results (Figure 3.13). The reason for that is there exist four samples namely CA-6NM #3-8, #3-21B, #3-6 and #3-19B that experimentally fail after the target life of 25000 cycles (cf. Table 3.3). When the *Y(a)* of **0.85** was applied to the Kitagawa-Takahashi model, the aforementioned four samples were in the safe design zone and this validated *Y(a)*, of **0.85** as the best fit.

Note that the final crack size ($\sqrt{area_{(f)}}$) roughly refers to the end of the propagation region (i.e., river lines) just before rupture displayed in Figure 3.7. Similar to the initial defect size measurement, the final size was also quantified using the image processing software Fiji, ImageJ for both broken halves of each fatigue sample and the largest size was recorded afterwards.

In brief, the results of this section represent that considering the LEFM model, for a crack with an initial measure of ($\sqrt{area_{(i)}}$) to propagate to the final size ($\sqrt{area_{(f)}}$) in a specific number of cycles (N_f), an average value of the geometrical parameter ($\bar{Y}(a)$) between **0.67** and **0.87** must be considered.

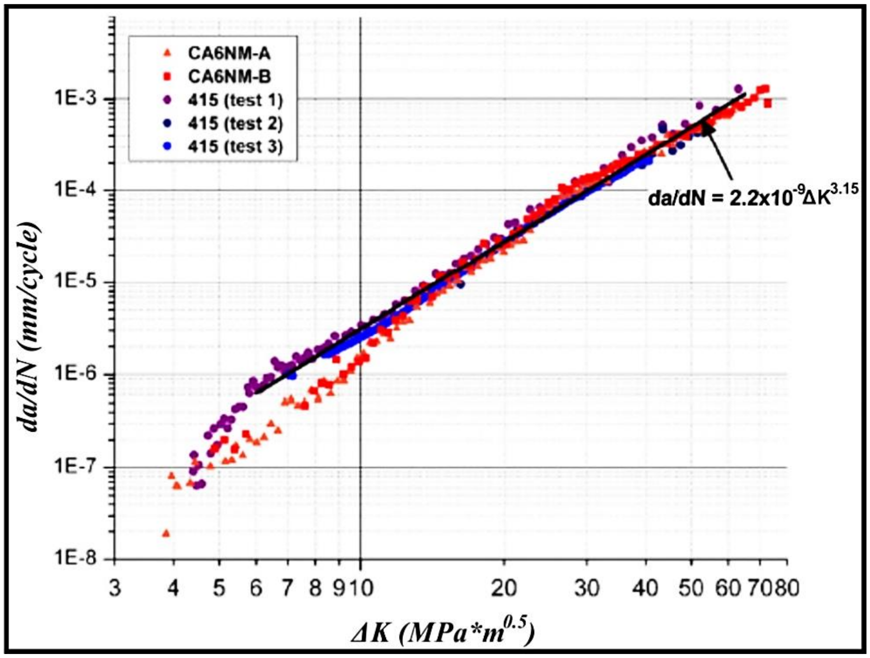

Figure 3.12 Fatigue crack propagation behavior of CA-6NM
Taken and adapted from Thibault et al. (2011, p. 6522)

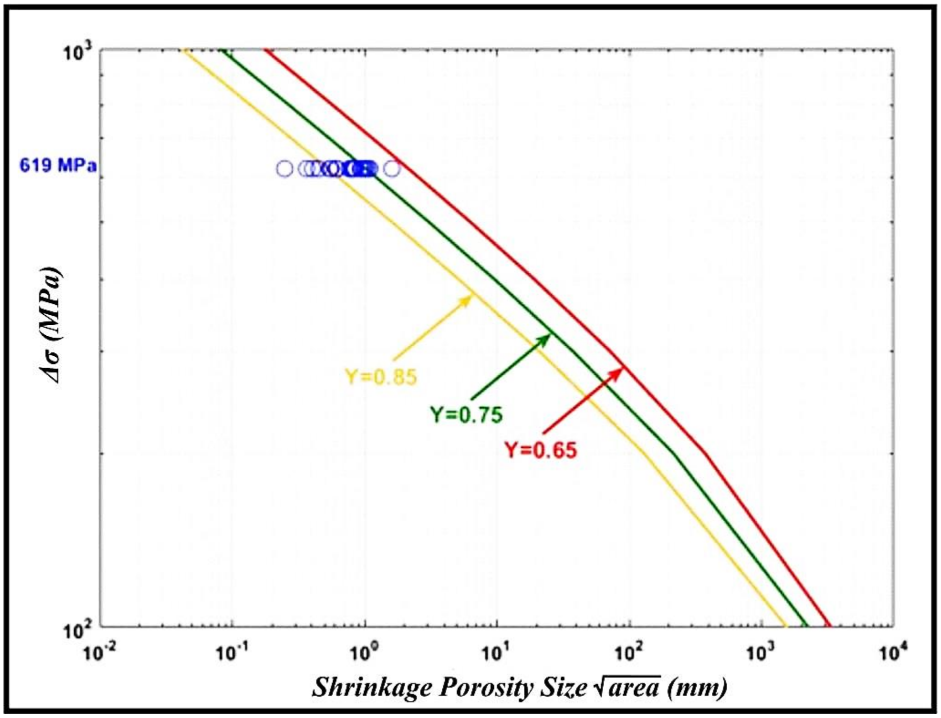

Figure 3.13 Kitagawa-Takahashi diagram for studied cast CA-6NM

3.3.2.2 Geometrical correction factor model for surface cracks in a solid cylinder

In this method, the geometrical factor ($Y(a)$) was solved and verified using an equation for surface cracks in a solid cylinder exposed to **tension** loading (Forman & Shivakumar 1986; Forman, et al. 1998).

Figure 3.14 illustrates a schematic surface crack in a cylindrical rod. "2*c*" represents the crack length, "*a*" exhibits the crack depth and a/c is presumed to equal one. Applying this solution, the stress intensity factor along the front of the surface crack and subsequently, the geometrical correction factor $Y(a)$ can be expressed by equations (3.5, 3.6 and 3.7):

$$K_T = Y(a)_T * \sigma_T * \sqrt{\pi a} \qquad (3.5)$$

$$Y(a)_T = GG_1 \qquad (3.6)$$

where

$$\left.\begin{aligned} G &= 0.92\left(\frac{2}{\pi}\right)\sec\beta\left(\frac{\tan\beta}{\beta}\right)^{0.5} \\ \beta &= \left(\frac{\pi}{2}\right)\left(\frac{a}{D}\right) \\ G_1 &= 0.752 + 1.286\,\beta + 0.37\,A^3 \\ A &= 1 - \sin\beta \end{aligned}\right\} \qquad (3.7)$$

where "D" and "a" were defined as the fatigue sample diameter and the final size of the defect/crack ($\sqrt{area_{(f)}}$) respectively. All other necessary parameters such as stress range and Paris law constants were derived from Table 3.4.

Using a Matlab routine and "Forman & Shivakumar" solution (i.e, equations 3.6 & 3.7) for each fatigue sample, the geometrical correction factor $Y(a)$ was calculated by a "step by step" reduction from the final size ($\sqrt{area_{(f)}}$) to the initial size ($\sqrt{area_{(i)}}$) in a specific number of cycles (N_f). The variation of geometrical factor *Y(a)* during the fatigue crack propagation stage was modelled and quantified. The results are listed in Table 3.3, the seventh column named “computed *Y(a)*”.

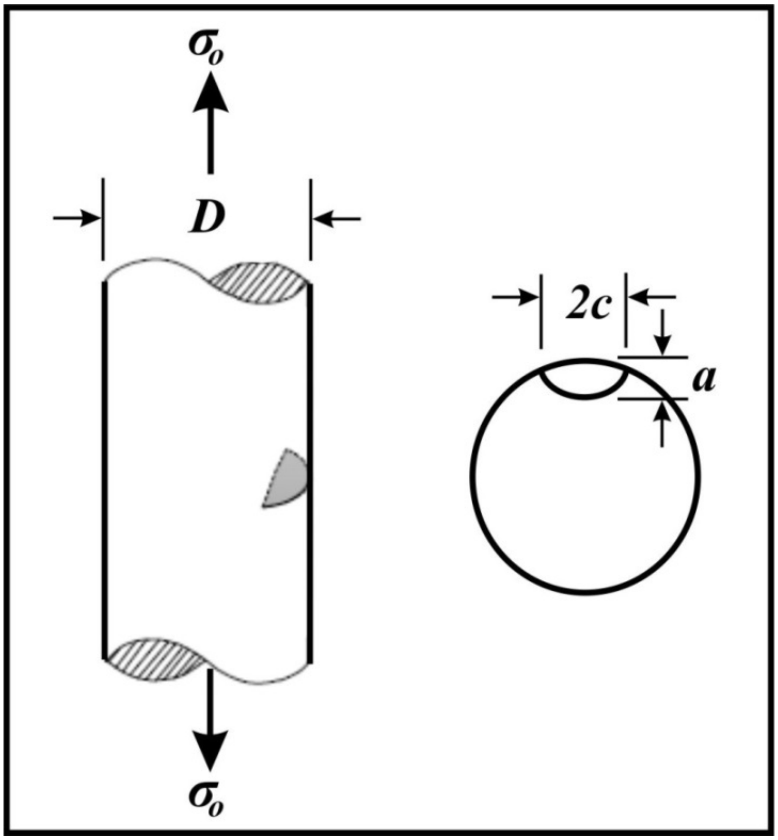

Figure 3.14 A surface crack in a solid cylinder under tension loading, taken and adapted from Zhang, Liu, Wang, & He (2017, p. 9)

Moreover, Figure 3.15 represents the variation process of the predicted *Y(a)* factor in proportion to crack size plotted for two picked samples tested in fatigue. In this figure, sample CA-6NM #3-7 and CA-6NM #3-19B show the lowest and highest fatigue life respectively. A complete collection of these plots for all 22 fatigue samples is demonstrated in APPENDIX I, Figure II.

A careful observation of each plot shown in the above-mentioned figures and numerically computed geometrical factor (*Y(a)* in Table 3.3) describes that the stress intensity along the whole crack front during the fatigue crack propagation is highly dependent on the size of the crack. The data analysis displays a gradual transition from a defect with an intricate shape to almost a regular semi-elliptical crack.

Using this hypothesized model, the initial size of the defects was also predicted and compared with the experimentally measured data (Figure 3.16, Table 3.3 the fourth and fifth columns). The standard deviation values of the measured and computed initial crack size data are around 0.303 and 0.247 respectively. In the same order, the mean values are about 0.769 and 0.737. Hence, the estimate for the difference is 0.032. This analysis represents that the predicted and experimentally measured data seem to be in good agreement; therefore, the model can be extended to actual surface defects in cylindrical fatigue samples.

Table 3.3 Axial tension-tension fatigue testing results, fractographic analysis and numerical results for geometrical correction factor *Y(a)*

CA-6NM sample number	**Cycles to fracture (N_f)**	**Measured *final* crack size $\sqrt{area_{(f)}}$ (*mm*)**	**Measured *initial* crack size $\sqrt{area_{(i)}}$ (*mm*)**	**Computed *initial* crack size $\sqrt{area_{(i)}}$ (*mm*)**	**$\bar{Y}(a)$**	**Computed *Y(a)***
#3-7	5436	3.14	1.62	1.48	0.75	1.04 → 0.75
#3-20A	10708	2.9	1.06	1.03	0.77	0.99 → 0.71
#3-19A	10959	3.31	1.01	1.04	0.8	1.09 → 0.71
#3-5	12353	3.32	0.95	0.97	0.79	1.09 → 0.71
#3-14	13911	3.28	0.93	0.89	0.75	1.08 → 0.7
#3-11	14671	2.86	0.85	0.84	0.76	0.97 → 0.7
#3-16	16640	3.15	0.98	0.78	0.7	1.05 → 0.69
#3-21A	16901	3.18	0.79	0.78	0.76	1.05 → 0.69
#3-9	17439	3.23	1.1	0.76	0.67	1.07 → 0.69
#3-10	18691	2.91	0.81	0.71	0.72	0.99 → 0.69
#3-20B	18992	2.81	0.77	0.7	0.73	0.97 → 0.69
#3-4	19621	2.41	0.56	0.67	0.78	0.89 → 0.69
#2-5	19663	3.48	0.61	0.7	0.79	1.14 → 0.69
#3-3	20197	2.78	0.84	0.67	0.68	0.96 → 0.69
#3-15	21056	2.28	0.37	0.62	0.87	0.86 → 0.68
#3-13	21152	3.04	0.61	0.65	0.77	1.02 → 0.69
#3-12	22976	3.54	0.8	0.62	0.7	1.16 → 0.68
#3-2	23377	2.89	0.62	0.6	0.73	0.98 → 0.68
#3-8	27851	3.01	0.54	0.52	0.72	1.01 → 0.68
#3-21B	36741	3	0.4	0.4	0.71	1.01 → 0.67
#3-6	37083	2.46	0.25	0.39	0.79	0.90 → 0.67
#3-19B	37579	3.55	0.45	0.4	0.7	1.16 → 0.67

Table 3.4 Parameter sets for Kitagawa-Takahashi diagram

Stress range ($\Delta\sigma = \sigma_{max} - \sigma_{min}$) (*MPa*)	**C, E^{-09}**	**m**	**Target life (N)**	**$Y(a)$**
619.2	2.2	3.15	25000	0.65 , 0.75, 0.85

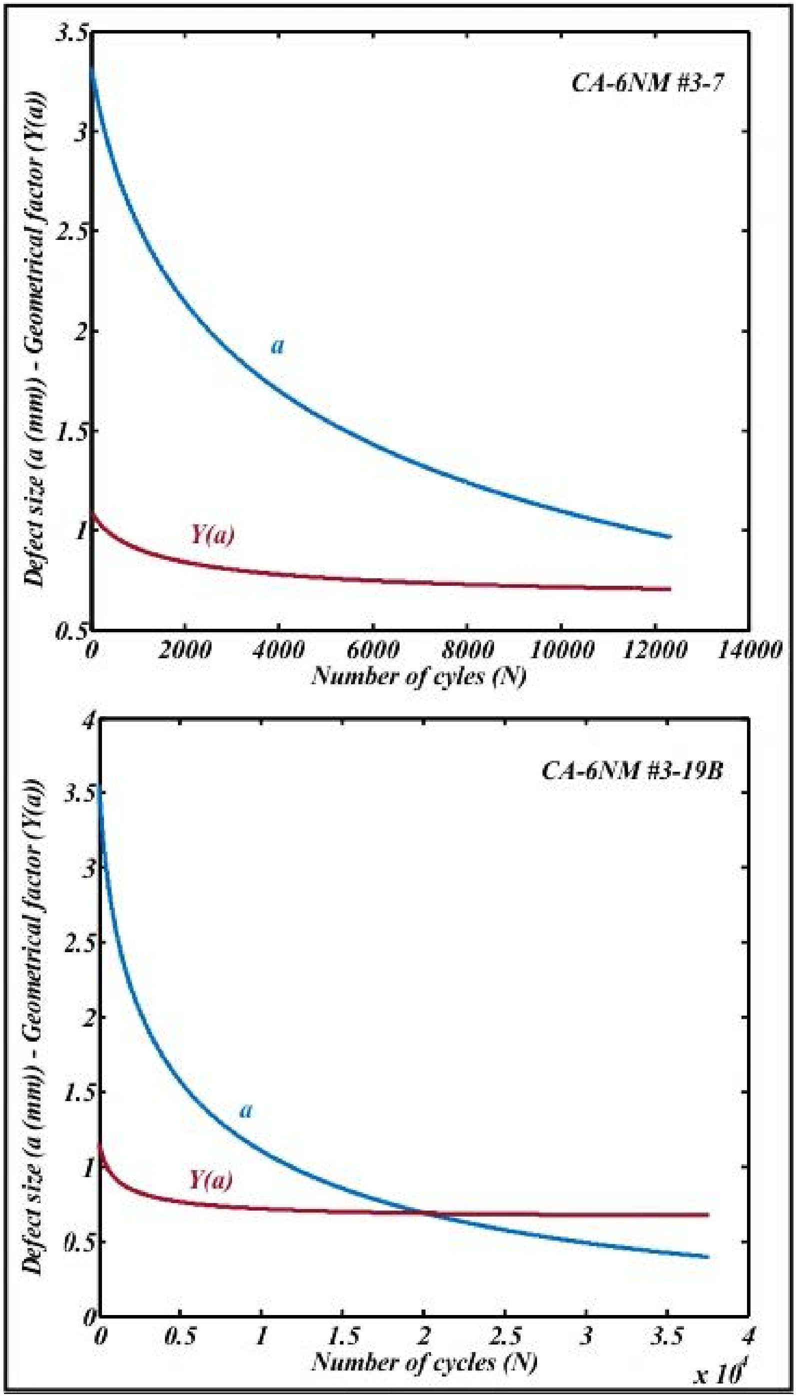

Figure 3.15 Showing the variation of the *Y(a)*
during fatigue crack propagation

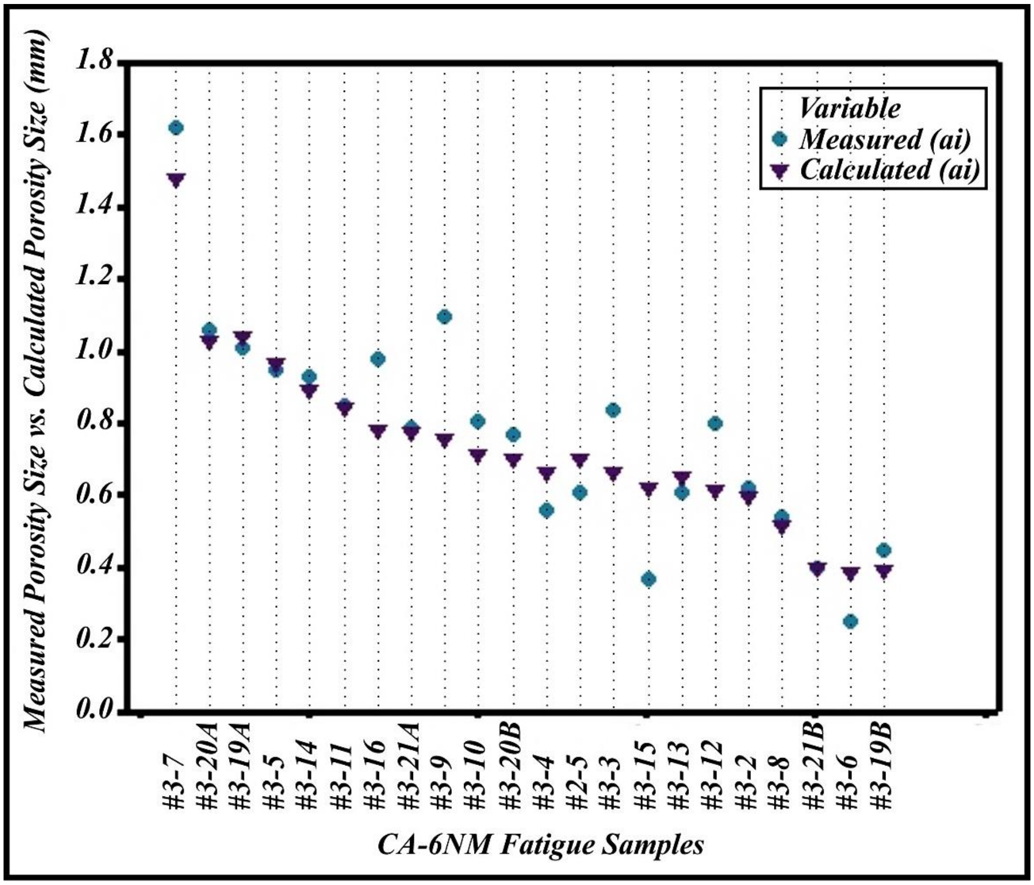

Figure 3.16 Overlapping the measured and predicted initial size of the shrinkage porosities serving as fatigue failure initiation sites

3.4 Conclusions

In this chapter, the uniaxial tension-tension low cycle fatigue testing was applied to the cast CA-6NM martensitic stainless steel fatigue samples. The main purpose was to investigate and correlate the defects characteristic to fatigue life and fatigue crack propagation. To this end, the fracture surfaces of broken samples were characterized in the scanning electron microscope (SEM). Using shape analysis software, the defects sizing parameters (i.e., initial size and final size) were evaluated. The fractographic analysis results are summarized as follows:

- All fatigue cracks were initiated from a surface/near-surface defect on the fracture surface cross-section.

- All crack initiation sites had an intricate and non-uniform configuration indicating that they are shrinkage porosities. Therefore, shrinkage porosities play a critical role in cast CA-6NM stainless steel fatigue properties.

- A statistical distribution of the fatigue life of stressed specimens was quantitatively evaluated by a negative exponential function. The general tendency is that the life decreases with an increase in the size of shrinkage porosities (i.e., fatigue failure initiation sites), but their correlation is nonlinear. The curve displays a steep decline at the initial steps. This illustrates that the fatigue life is sensitive to the presence of shrinkage porosities. Moreover, The scatter in the results shows that the fatigue life of castings with shrinkage porosities is difficult to determine only from the defects' size.

- Following linear elastic fracture mechanics (LEFM) relations, the Kitagawa-Takahashi diagram was predicted and compared with experimental measurements.

- The geometrical factor ($Y(a)$) variation in proportion to the size of the defects during fatigue crack growth was also modelled and quantified considering the LEFM conditions:

    1. In the back-tracking method, for a crack with an initial size of ($\sqrt{area_{(i)}}$) to propagate to the final size ($\sqrt{area_{(f)}}$) in a specific number of cycles (N_f), an average value of the geometrical parameter ($\bar{Y}(a)$) between **0.67** and **0.87** could be considered.

    2. In the "Forman & Shivakumar" solution (i.e., the shape correction factor for surface cracks in a solid cylinder exposed to tension

loading), the $Y(a)$ was calculated for crack sizes reducing from the final size ($\sqrt{area_{(f)}}$) to the initial size ($\sqrt{area_{(i)}}$) in a specific number of cycles (N_f) and the variation process of geometrical factor $Y(a)$ during the fatigue crack growth for each sample was acquired.

- Using the “Forman & Shivakumar” solution, the initial size of the shrinkage porosities/cracks (i.e., the origin of fatigue failure) was predicted and the results agreed well with the experimentally measured data.

CHAPTER 4

THREE DIMENSIONAL (3D) X-RAY TOMOGRAPHIC CHARACTERIZATION OF SHRINKAGE POROSITY AND FATIGUE PROPERTIES OF CAST CA-6NM MARTENSITIC STAINLESS STEEL

4.1 Introduction

In steel casting components, shrinkage porosities are highly detrimental due to their three-dimensional (3D) complex nature and interaction with other casting discontinuities. The effect of shrinkage porosities on the reliability and fatigue properties of cast steels is of significant importance and has been pursued in some studies (Kim et al., 2006; Sigl et al., 2004; Briggs, 1969; Briggs, 1966). However, various aspects of such investigations in cast CA-6NM martensitic stainless steels are not self-evident and well understood in detail. Shrinkage porosities are categorized into macro- and micro- shrinkage porosity. They are also the most common discontinuities found in this research. Macro-shrinkage porosities (i.e., a few millimetres and larger) are usually large enough to be identified by a non-destructive inspection such as X-ray radiography, while micro-shrinkage porosities are invisible to this kind of inspection.

Conventional methods such as non-destructive X-ray radiography (cf. chapter 2 & chapter 3), metallography (using an optical microscope) (cf. chapter 2), destructive “Salami” cross-sectioning (cf. chapter 2) and fractography (using a scanning electron microscope (SEM)) (cf. chapter 3) are used to quantify defects in the planar sections of cast structures. However, on a two-dimensional (2D) cross-section, various configurations of three-dimensional (3D) shrinkage porosity might emerge. These forms could be either the arms of a large shrinkage porosity that are appeared as smaller isolated and diffused porosities or some of the adjacent porosities revealed on the same cross-section. All these might cause a severe underestimate of the actual equivalent size of shrinkage porosities and make it entirely challenging to evaluate its accurate morphology. Figure 4.1 illustrates this fact by a 3D appearance of a shrinkage porosity which is randomly and non-destructively sliced to model the shrinkage geometry in 2D.

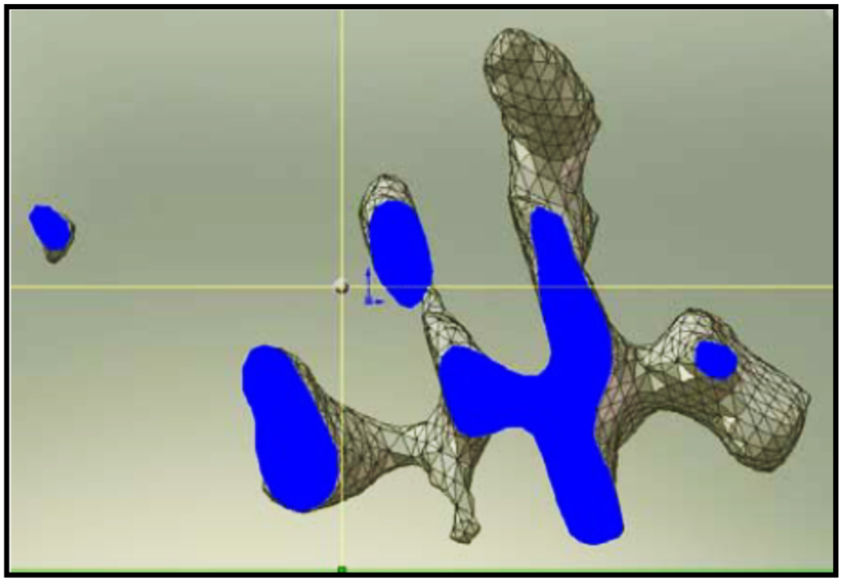

Figure 4.1 Simulated cross-sectioning of shrinkage
porosity in cast Al-alloy
Taken from Nicoletto, Anzelottia & Konečná (2010, p. 551)

To investigate the correlation between the fatigue properties of a cast component and the presence of shrinkage porosities, fracture surfaces of broken specimens are usually studied in a scanning electron microscope (SEM). Fractography is routinely used to determine which defect(s) is (are) responsible for crack nucleation and also to quantify the sizing parameter of the defect(s). As implied earlier, this type of characterization only provides two-dimensional (2D) information of shrinkage porosities which may not be adequate to describe their tortuous morphology. Another drawback of fractographic characterization is that it can only reveal the crack initiation sites within the distribution of porosities (i.e., weak link). When it comes to the tail of the distributions, which matters in fatigue, assessments and comparisons with other specimens stay qualitative (Zhu, Yi, Jonesn & Allison, 2007; Yi, Gao, Lee, Flower & Lindley, 2003). In this respect, statistical frameworks are required to derive a quantitative characterization of the porosity distribution/population and establish its relationship with fatigue damage progress of cast materials more precisely (Wang & Jones, 2007).

Furthermore, the crack nucleation site is the first thing to appear in fatigue testing. When the fatigue sample is pulled apart completely it will be difficult to find and examine microstructural features. Consequently, following the propagation path of the fatigue crack and studying its interaction with involved defects requires some assumptions and interpretations. Combining the three-dimensional (3D) examination before (i.e., pristine sample) and after (i.e., broken sample) fatigue failure facilitates the interpretation of failure analysis obtained by fractography via SEM images (Yang, Kang & Wilkinson, 2015).

Three-dimensional (3D) reconstructed images of natural shrinkage porosities within the volume of fatigue specimens are commonly obtained by laboratory X-ray computed tomography. Using image analysis software, the tomographic data will then be processed to evaluate the main characteristics (size, position, projected area, volume, population, etc.) of the shrinkage(s) that were the source of the fatigue failure. This information applies to analyze the correlation between fatigue properties of the studied material and the aforementioned characteristics and to illustrate which one could be dominant for the cause of the failure. Collecting all this detailed information might give a better understanding of the role of the shrinkage porosity in the fatigue behavior of the cast CA-6NM material.

In short, the goals of this chapter are: (1) to peruse the 3D examination of shrinkage porosities in cast CA-6NM martensitic stainless steel; (2) to image and discover the fatigue crack nucleation site(s); (3) to verify the main characteristics of those defects and (4) to compare the XCT inspection with SEM observation in failure analysis.

4.2 Experimental procedure

4.2.1 X-ray computed tomography

A cast CA-6NM fatigue sample was picked from the prepared samples used in chapter 3. After machining and an accurate polishing of the fatigue specimen, X-ray computed tomography inspections (XCT) were performed on the gauge length of the specimen in stress-free conditions prior to and after fatigue failure. The laboratory computed tomography used in this study is a Nikon XT-H225 computed tomography system. The X-ray source operates at a voltage of 225 keV. The XCT scan was accomplished with a set of parameters listed in Table 4.1. To guarantee that the CT scan will cover the whole gauge section of the pristine fatigue sample, the inspection was slightly extended to a larger area than the gauge segment (25.4 mm/1-inch) and the scanned region became around 33.44 mm (1.31-inch). This scan comprised ~1780 two-dimensional (2D) radiograph projections with an exposure time of 2.83 seconds. The voxel size was 16.91 µm.

Following conducting the fatigue test, broken halves of the specimen were scanned one more time with the same set of parameters (Table 4.1). The voxel size for the longer segment of the broken gauge was 20.52 µm and for the shorter one, it was 13.36 µm. These scans also comprised ~1780 two-dimensional (2D) projections with an exposure time of 2.83 seconds. In all scans (i.e., before and after the fatigue test), a copper plate filter with a thickness of 1.25 mm was applied. In the present study, the 360° rotation scan was performed to image the geometry of porosities. Also, one scan was enough for each sample.

Table 4.1 X-ray computed tomography settings parameters

Parameters	**Initial scan (pristine sample)**	**Final scan (broken segments)**
Beam current (µA)	50	50
Beam energy (keV)	210	210
Rotation step (deg.)	0.2	0.2
Rotation angle (deg.)	360	360

Afterwards, using the CT PRO 3D software (Nikon Metrology), the three-dimensional (3D) reconstructions of acquired images were processed. In order to quantify and evaluate characteristics of internal shrinkage porosities of the studied material, Dragonfly image analysis software was applied to the reconstructed images. Using this rendering software, shrinkage porosities were extracted as separate regions of interest (ROI). Different characteristics of each shrinkage porosity such as the volume, size, surface area (X, Y, Z), circularity, and position (i.e., the center of mass coordinates (X, Y, Z)) were measured. The porosity's sizing parameters quantified as its maximum Feret's diameter and surface area projected on the plane perpendicular to the loading direction (i.e., Murakami's geometrical parameter ($(\sqrt{area})_z$).

4.3 Experimental results, data analysis and discussion

Figure 4.2 represents different views of orthographic projections (2D) from the distribution of shrinkage porosities obtained by the 3D scan. The XCT scan belongs to the whole gauge length of the cast CA-6NM pristine fatigue specimen. Figure 4.3 also displays another set of orthographic projections (2D) of the sample gauge length but with 3D visualization of shrinkage porosities.

By comparing the initial 3D porosity analysis acquired by XCT inspection to "Salami" cross-sectioning results, it can be confirmed that the shrinkage porosities are certainly the most prevalent discontinuities found in this study. As mentioned before (cf. chapter 2), the crack propagation and failure in cast components are extreme value-related phenomena. Hence, before performing the fatigue test, it was hypothesized that the fatigue crack will initiate and propagate through the largest shrinkage porosity present in the sample. The largest porosity is indicated in Figures 4.3 (marked with arrows) and Figure 4.4.

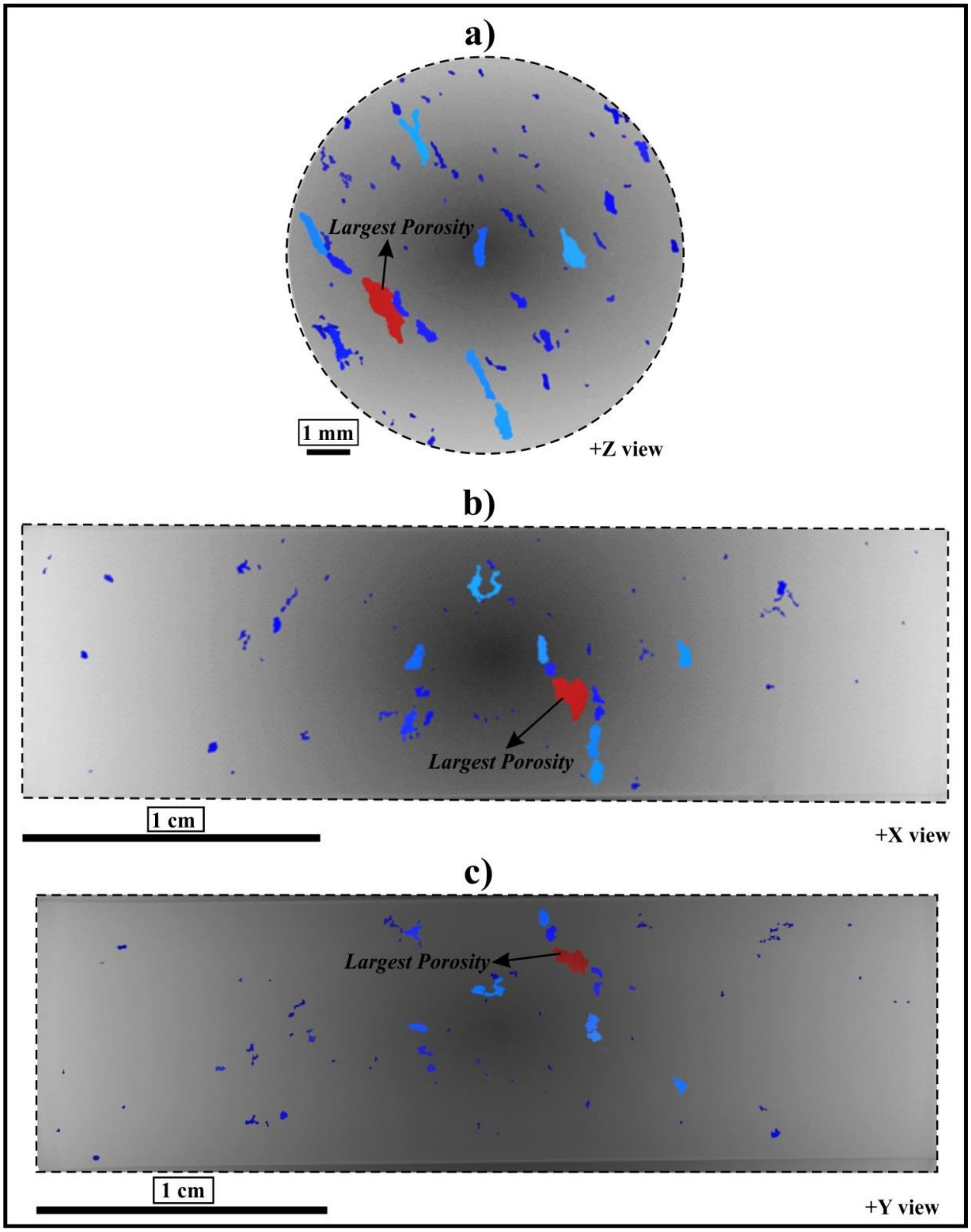

Figure 4.2 (a), (b), (c) Orthographic projections of the gauge length

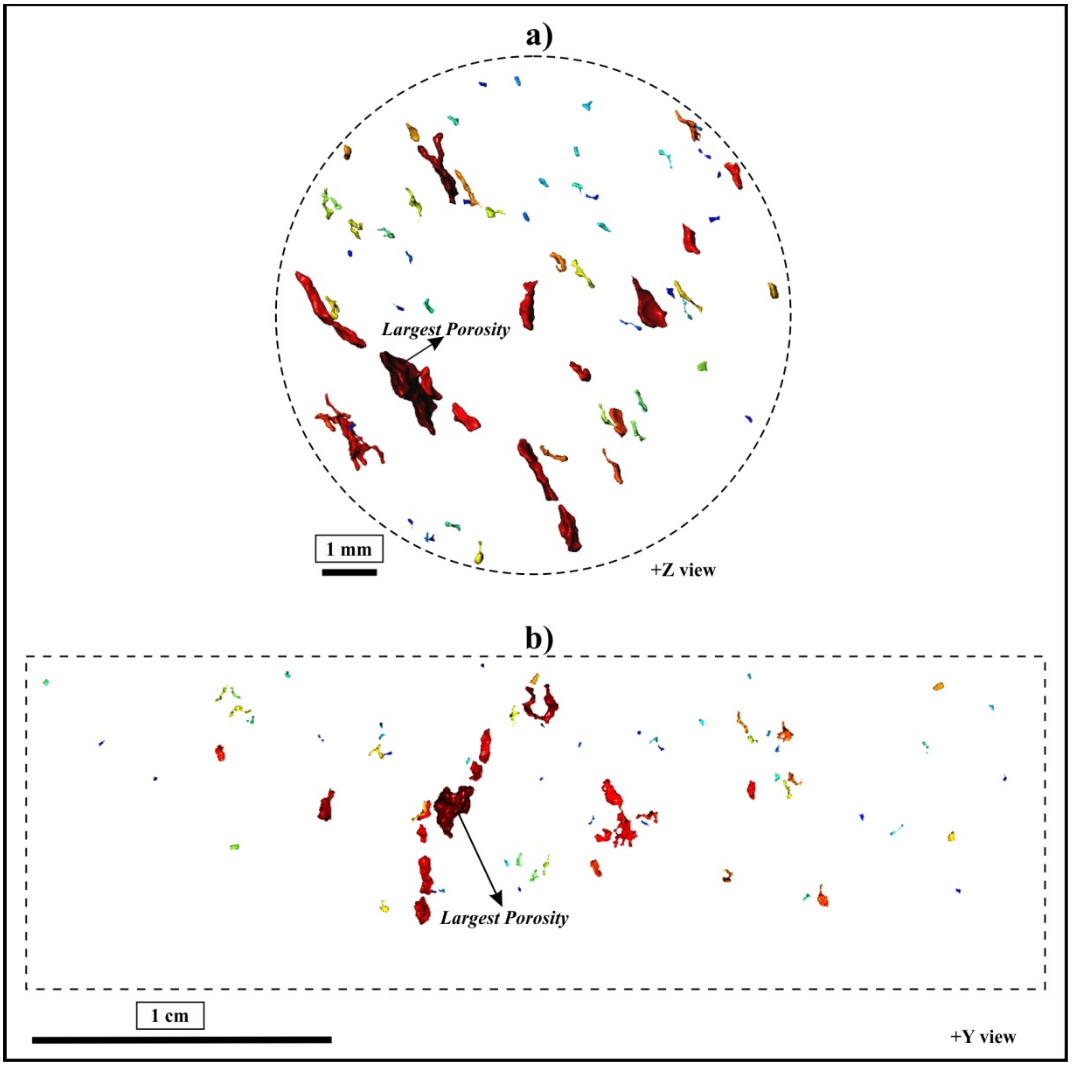

Figure 4.3 (a), (b) Orthographic projections of the gauge length with 3D visualization of shrinkage porosities

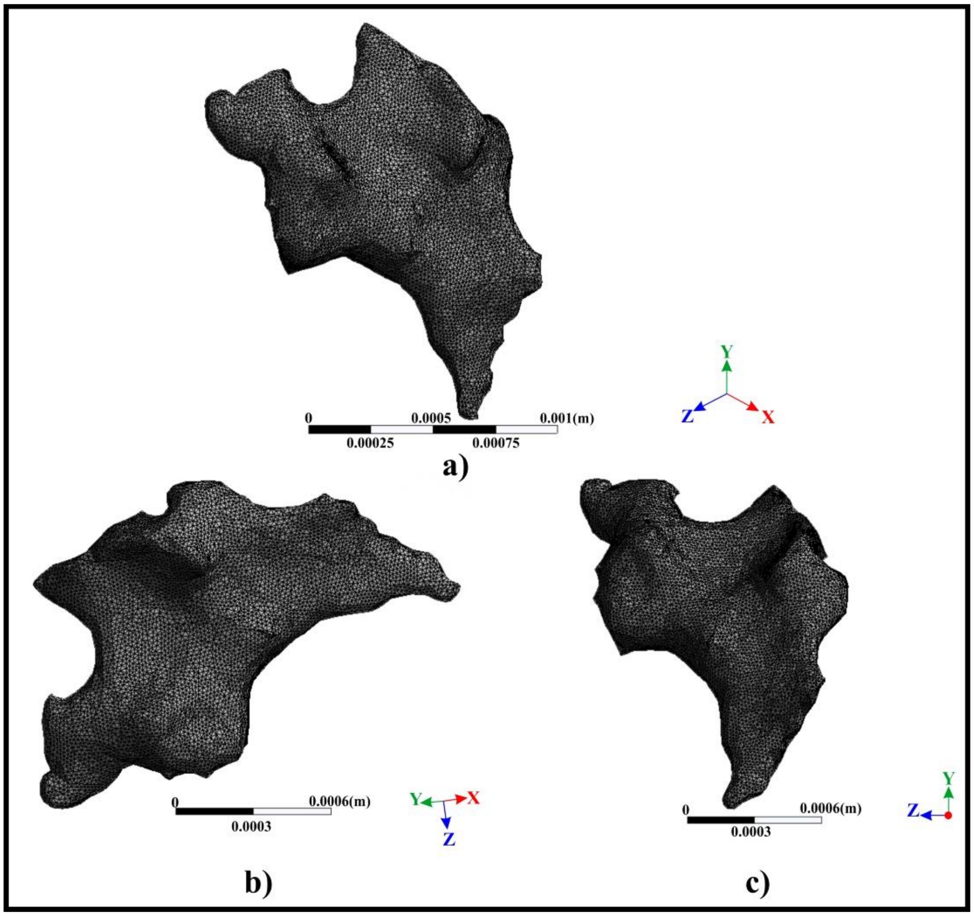

Figure 4.4 (a), (b), (c) Showing the 3D volumetric configuration of the largest shrinkage porosity indicated in Figure 4.3

After the initial XCT scan, a uniaxial tension-tension fatigue test was conducted at room temperature in the ambient air, with a stress ratio of 0.1 (R=0.1), a frequency of 5 Hz, and with maximum applied stress of 688 MPa. The fatigue failure occurred at 20453 cycles. After the complete rupture, the second XCT scanning was conducted on broken segments of the fatigue specimen and 3D tomographic images were reconstructed one more time.

To identify the position of the fracture surface and the shrinkage porosity(s) responsible for fatigue crack initiation, the 3D images of the ruptured segments were reassembled and overlapped with the 3D distribution of shrinkage porosities that belongs to the pristine sample gauge length. Figure 4.5 represents a frontal and side view of the stitched parts containing shrinkage porosities. Figure 4.6 displays one of the broken segments overlapped with the gauge length. Besides, to focus on the porosities around the fracture transverse section, a non-destructive cross-section of ~ 6 millimetres about the fractured area was virtually selected. In Figures 4.6 and 4.7, the position of the shrinkage porosity that initiated the fatigue failure has been marked by green arrows. The 3D configuration of this defect in higher resolution and different orientations is illustrated in Figure 4.8.

Table 4.2 compares various characteristics of the largest porosity with the shrinkage porosity which is responsible for the failure. In this regard, Figure 4.9 defines the distance (i.e., position) of the aforementioned shrinkage porosities from the free surface of the fatigue specimen.

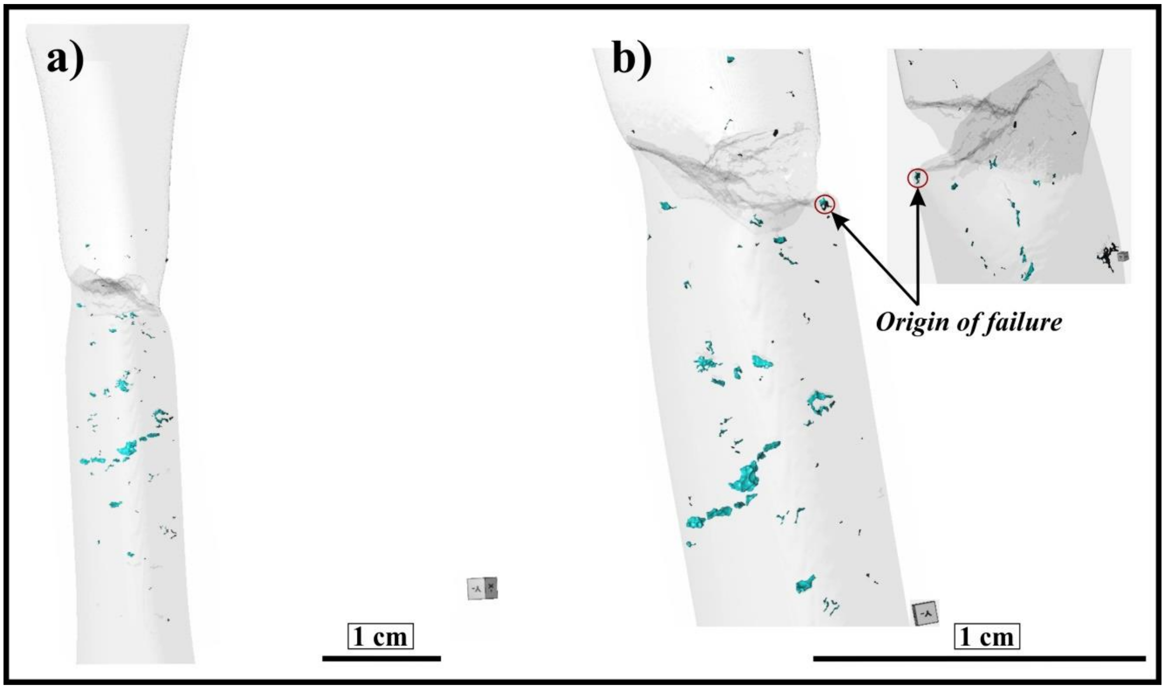

Figure 4.5 Virtual reassembly of ruptured fatigue sample parts
(a) Frontal view and (b) Side view

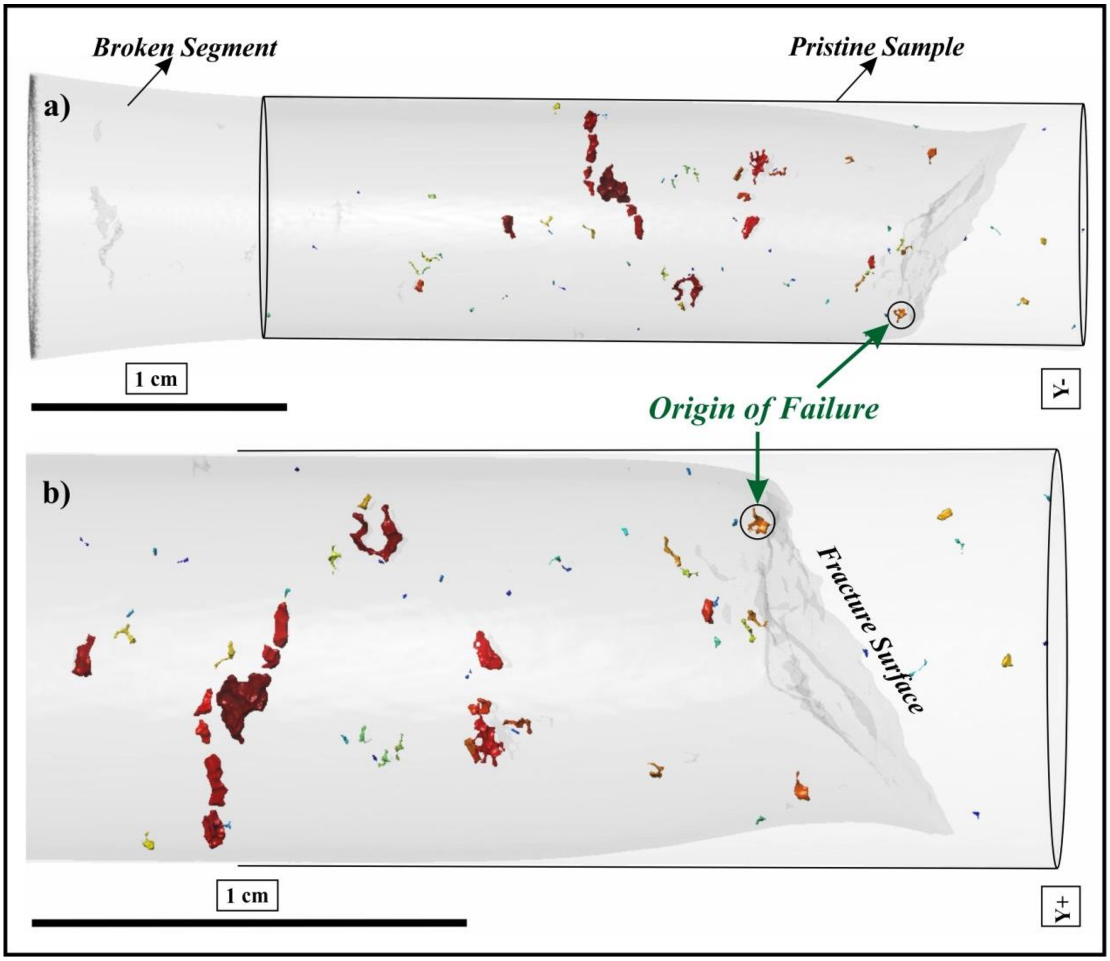

Figure 4.6 (a), (b) 3D illustration of one of the broken parts overlapped with the fatigue sample gauge length in different magnifications

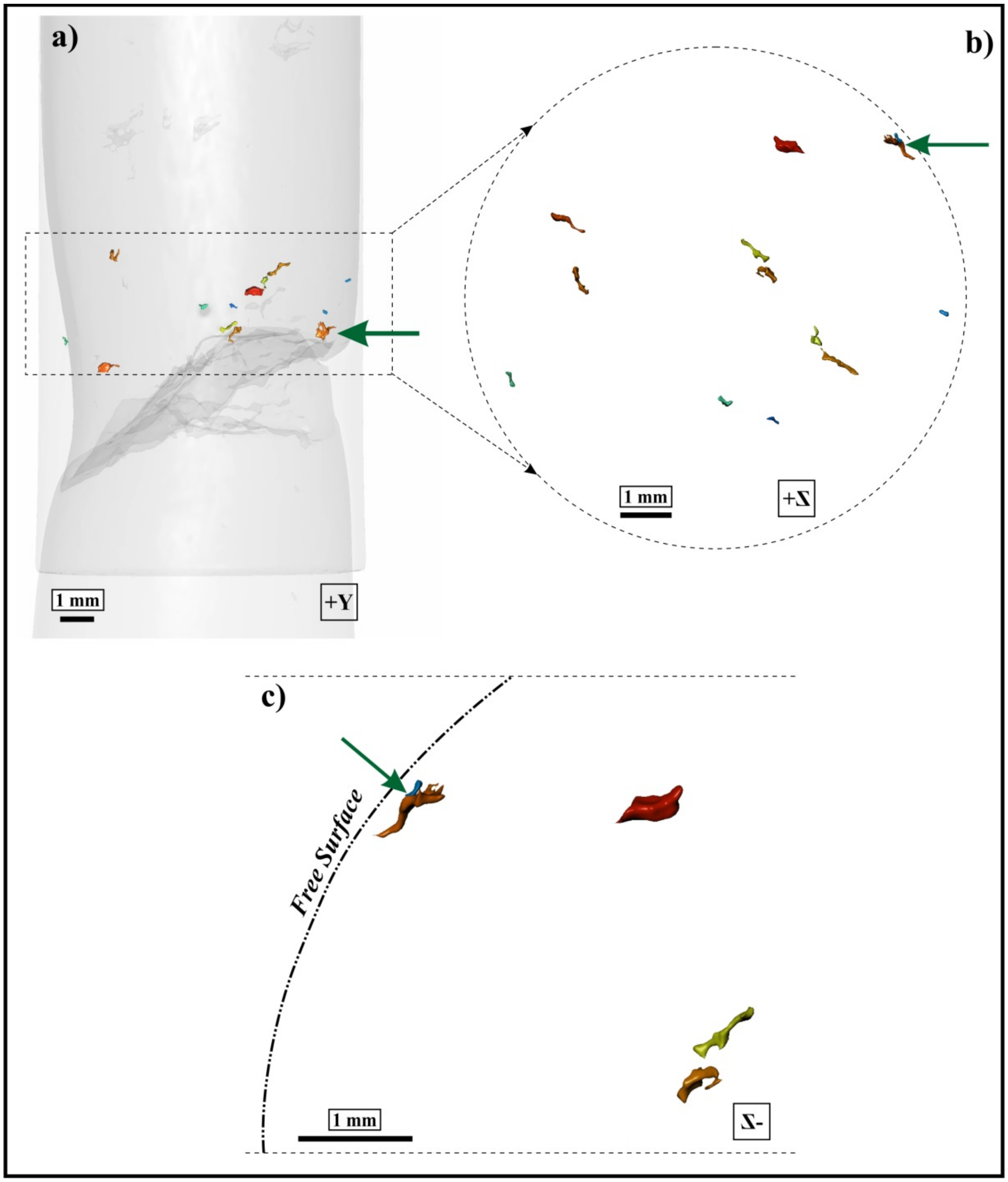

Figure 4.7 (a), (b), (c) Showing distribution of shrinkage porosities on a non-destructive cross-section (~ 6 millimetres width) around the fractured area

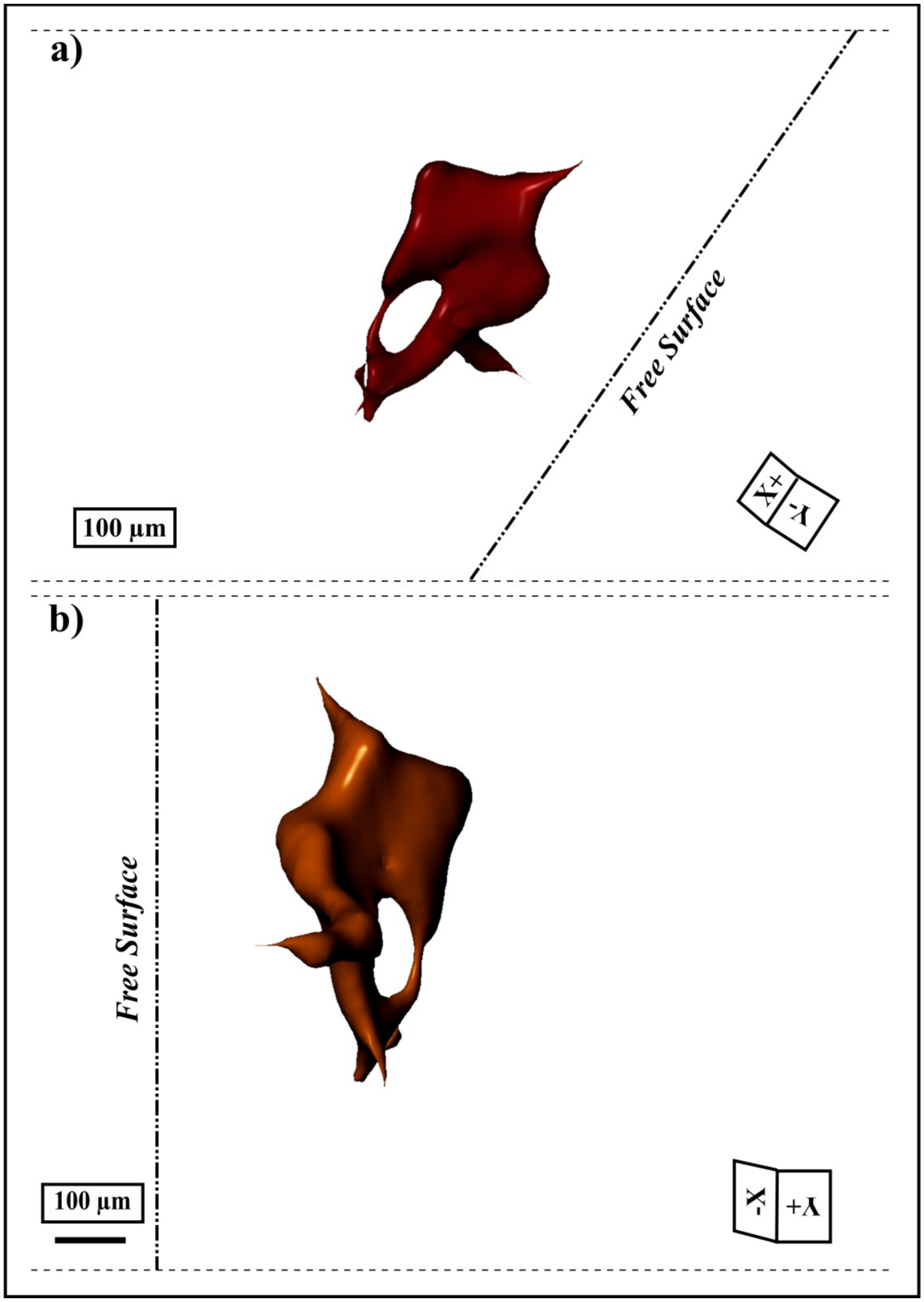

Figure 4.8 (a), (b) Showing 3D visualization of the failure initiation site in various orientations towards the free surface

Table 4.2 Characteristics of the largest porosity and the origin of fatigue failure studied by X-ray computed tomography

CA-6NM Sample number	#2-8	#2-8
Label	Largest porosity	Origin of failure
Volume (mm^3)	**0.21**	**0.001**
Surface Area (mm^2)	5.7	0.7
Surface Area X (mm^2)	1.28	0.17
Surface Area Y (mm^2)	2.67	0.34
Surface Area Z (mm^2)	1.75	0.19
Maximum Feret's Diameter (mm)	**1.71**	**0.84**
Square Root of Surface Area Z ($(\sqrt{area})_Z$) (mm)	**1.32**	**0.44**
Distance from Free Surface (d= mm)	**1.9**	**0.18**
Circularity	**0.5**	**0.33**

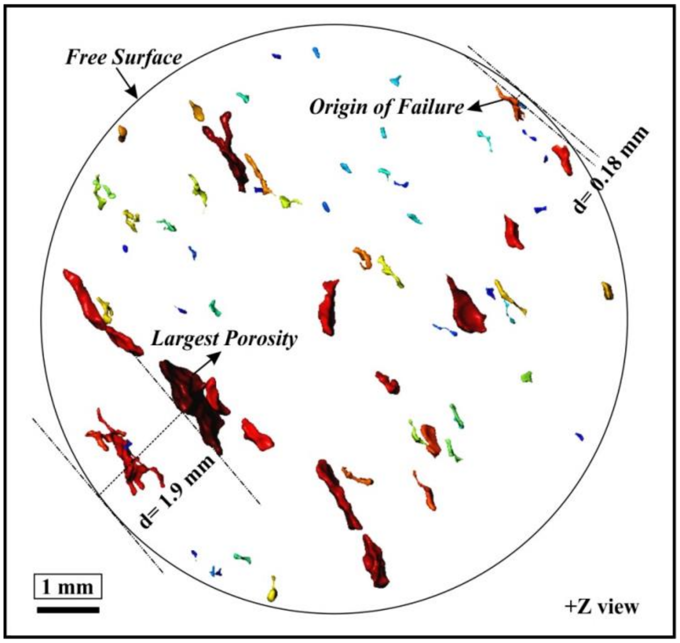

Figure 4.9 Measuring the distance of porosities from the free surface

Based on the three-dimensional (3D) porosity analysis of the fatigue sample, matching it with the ruptured segments, and data analysis in Table 4.2, fatigue crack did not initiate from the largest shrinkage porosity within the gauge length volume but a close to the surface porosity meaning that the largest shrinkage porosity which is further away from the surface is not responsible for the failure. The characterization data in Table 4.2 demonstrates that the size ratio of the largest inner defect and the near-surface defect (i.e., the origin of fatigue failure) is about **2** and **3** for maximum Feret's diameter and Murakami's geometrical parameter $(\sqrt{area})_z$ respectively.

That means that the position of a defect certainly has a more critical role in the fatigue failure of the studied material.

Under cyclic loading, the local stress concentration level in the proximity of the near-surface irregular-shaped shrinkage porosity increases severely. The enhanced stress activates plastic deformation (strain localization) around the defect and accelerates the fatigue crack initiation (Borbély, Mughrabi, Eisenmeier & Höppel, 2002). This local stress depends on the defect's morphology, its distance from the free surface and the adjacent porosities.

It is important to cite that even if the three-dimensional complex configuration of shrinkage porosity is idealized as a spherical pore, the position effect is still substantial. Gao *et al.* (2004) studied two spherical defects with the same size but different locations. The maximum stress concentration factor (K_t) around the surface defect and the internal defect were 4.1 and 2.1 respectively which means that the stress concentration factor can be approximately 50% higher when the defect is situated at the free surface and thereby the surface defect is more critical to initiate a fatigue crack.

To investigate the behavior of the studied porosities more deeply, the level of irregularity was also quantified. In shape analysis, circularity (also known as projection sphericity or form factor) describes the complexity of the shape. Circularity is sensitive to geometry and it indicates the deviation of a configuration from a circular form. This shape parameter is typically measured on a two-dimensional (2D) cross-section image of the porosities that is perpendicular to the direction of the applied stress and it is defined as:

$$Circularity = 4\pi * Area/(Perimeter)^2 \tag{4.1}$$

Circularity ranges between **0** and **1**. From the results listed in Table 4.2, it is obvious that the largest porosity has a higher circularity than the shrinkage porosity responsible for failure (**0.5** vs. **0.33**). This discrepancy demonstrates that the latter defect has a more elongated, irregular and complex morphology. From Figure 4.8 it can be perceived that the shrinkage porosity responsible for failure has a tortuous geometry with extremely sharp/thin grown arms (similar to a crack) in various directions. Different orientations of this defect towards the free surface show that the sharp contours of the porosity are formed perpendicular to the loading axis. Furthermore, it can be seen that there exists a hole inside this shrinkage porosity which also acts as a severe stress concentration raiser (Bacaicoa et al., 2017). All these evaluations represent that wherefore this shrinkage porosity is capable of initiating the fatigue crack which had led to rupture.

In the last step, the fatigue fracture surface was examined by SEM (Figure 4.10). Observing both the SEM result and three-dimensional defect analysis obtained by XCT, the porosity which initiated the fatigue crack and influenced the subsequent crack propagation was identified and confirmed. However, it is evident that the three-dimensional characterization provides more precise and detailed information about the shrinkage porosities characteristics.

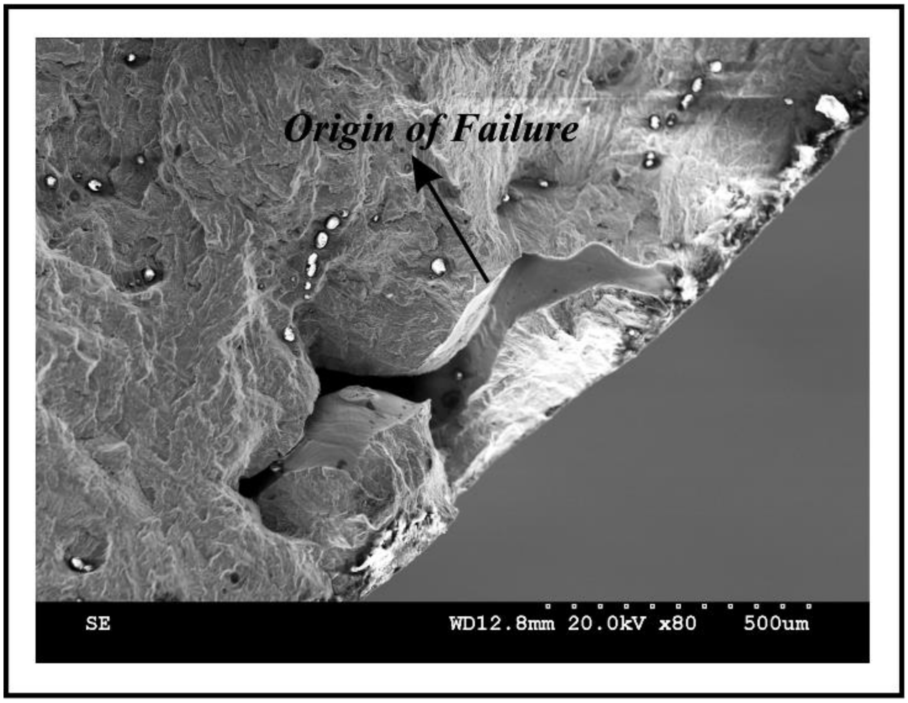

Figure 4.10 SEM micrograph of the fracture surface of the CA-6NM (sample #2-8) broken in fatigue

4.4 Conclusions

A non-destructive 3D evaluation of the shrinkage porosities characteristics (i.e., size, morphology and location) in the cast CA-6NM martensitic stainless steel was the main thrust of this stage of the investigation. To this end, X-ray tomography imaging and later on image analysis procedures were conducted to characterize the cast shrinkage porosities in fatigue sample gauge qualitatively and quantitatively. On this subject, the following outcomes can be drawn:

- Laboratory X-ray computed tomography provided a more detailed and precise three-dimensional (3D) distribution of shrinkage porosities alongside the interpreted analysis acquired by two-dimensional (2D) SEM fractography images.

- 3D porosity analysis obtained by XCT inspection certified that the shrinkage porosities are the most common defects found in this research.

- 3D porosity analysis showed that fatigue crack initiated from a close to surface shrinkage porosity even though there exists a several times larger porosity in the interior of the specimen gauge. Therefore, it is difficult to evaluate the detrimental effect of the casting porosity on the fatigue performance simply from the sizing parameter. Other characteristics such as defect position and 3D nature are of critical importance too.

- To establish an accurate relationship between fatigue properties and shrinkage porosity characteristics, complete quantitative distribution and population of the porosities within the sample is essential to be taken into account.

CONCLUSION

This research characterized the shrinkage porosities and evaluated their effect on fatigue properties of CA-6NM low carbon martensitic stainless steel.

In the first section of this study (Chapter 2), the macro-defects with different severity levels indicated in X-ray radiography mapping of the CA-6NM cast blade were assessed by destructive "Salami" cross-sectioning procedure to provide more complementary information about the actual shape and morphology of the defects. Applying this method confirmed defects as macro-shrinkage porosities. But, shrinkage porosities could extend from the macroscopic to the microscopic scale. Using image processing methodology, 779 isolated defects were detected in total. The fatigue crack propagation and failure in materials are extreme value-related phenomena. Therefore, various characteristics such as the smallest radius of defect tips, the maximum Feret's diameter, and the sizing parameter (i.e., Murakami's geometrical parameter ($\sqrt{area}$)) of the discontinuities extracted from the highest severity levels of each shrinkage porosity class were evaluated. Further shape analysis represented 95% of maco-shrinkage porosities with excessive sharp endings. Accordingly, the fatigue behaviour of cracks (LEFM conditions) was applied in the subsequent steps of this thesis. Moreover, higher severity levels of macro-shrinkage porosities illustrated sharper endings, a higher probability of larger Murakami's parameter ($\sqrt{area}$), and eventually more detrimental defects. Nevertheless, the metallographic examination supported by EDX analysis did not demonstrate a uniform element or phase segregation around the defects that could embrittle this area. Experimental results of the novel approach proposed in this research showed an extensive amount of accurate data.

In the second section of this research (Chapter 3), a set of 22 fatigue samples were cycled under uniaxial tension-tension low cycle (LCF) fatigue testing. The principal characteristics of the defects responsible for the fatigue failure and their impact on the distribution of the fatigue life in cast CA-6NM martensitic stainless steel were verified qualitatively and quantitatively. In doing this, two-dimensional (2D) fractographic and shape analyses were performed on fractured fatigue samples. Fractographic observations validated the morphology of shrinkage porosities. Besides, the relationship between the fatigue life and shrinkage porosity size was described by a negative exponential function and fatigue tests data displayed a substantial reduction of fatigue life when the Murakami's parameter ($\sqrt{area}$) of the defects (i.e., the fatigue crack initiation site) increased. However, the correlation between the fatigue life and the porosity size showed scatter. In this regard, the causes can be: (1) the near to the surface position of crack initiation site(s); (2) the distribution of shrinkage porosities of the whole sample which is variable from one to the next. Afterwards, following linear elastic fracture mechanics (LEFM) the variation of geometrical factor *Y(a)* in proportion to the size of the defects during the fatigue crack growth stage was modelled and quantified. The shape factor, *Y(a)*, of 0.85 was the best match describing the experimental fatigue results. The outcome represented that the computed data were correspondent with Murakami's shape factor for surface defects. Finally, the initial size of the defects was computed from the same solution. These results were also compatible with experimentally measured data.

In the third part of this investigation (Chapter 4), a non-destructive three-dimensional (3D) characterization of shrinkage porosity was conducted by X-ray computed tomography (XCT). One fatigue sample was examined. The outcome affirmed that the position of defects is more critical than the size of them. Fatigue crack initiated from a near-surface shrinkage porosity regardless of several times larger porosities present in the interior of the sample gauge. Also, compared to SEM observation in failure analysis, the XCT evaluation provided more detailed information on characteristics of shrinkage porosity.

Eventually, the research presented in this thesis focused on the characterization of casting defects and their effect on the fatigue properties of a cast turbine blade made of CA-6NM. In this regard, some of the principal goals were: (1) to discover the type of casting defects of the studied material; (2) to study how detrimental the defects can be to the fatigue performance; and (3) to investigate which individual characteristics of the defects could be predominant for the cause of the failure. These objectives were achieved using several techniques. Collecting all this detailed data alongside the X-ray radiography information provides a better understanding of the role of the shrinkage porosity in the fatigue behavior of the cast steels especially CA-6NM material.

However, the current research has been conducted for only one cast turbine blade. Also, characterization of defects by X-ray computed tomography was carried out on a restricted number of samples. Therefore, in this section of the study, statistical data about the effect of shrinkage porosities on fatigue data was not achieved. Moving forward, a larger spectrum of specimens produced through various casting processes will allow the comparison of different casting processes in terms of defects. Different types of defects with diverse levels of severity and the influence of their characteristics on fatigue properties can be perceived.

In addition, to estimate the stress distribution in the vicinity of the shrinkage porosity(s) potentially leading to the failure, to study the deformation field around the fatigue crack induced by the fatigue process and to investigate the distortion of involved defects close to the origin of the failure, a 3D finite element (FE) mesh of shrinkage porosities needs to be generated from the tomographic images. Afterwards, the 3D volumetric mesh has to be imported into a FE calculation package (taking into account the defect size, position and morphology) to compute the stress level around the porosity. This information is helpful to study the capability of the shrinkage porosities to initiate a fatigue crack. To this end, several finite element analyses (FEA) were performed. At first, an FEA model must ensure that the result converges to a solution and is independent of the mesh size. For instance, in this study, the region encompassing the shrinkage porosity was modelled with a refined mesh and maximum applied stress was solved based on the number of mesh elements. The goal was to achieve a convergence so that the amount of stress is repeatable while the mesh sizing decreases. Following that, the results are no longer sensitive to further mesh size reduction. Once this condition is attained, in the next step, the local stress concentration values as a function of geometry and type of loading around the internal surface of targeted shrinkage porosity could be evaluated. However, despite many testings, the convergence to a solution was not completely fulfilled.

In the end, a complete investigation on the casting defects characteristics and their relationship with fatigue properties requires considering a larger number of specimens, experimental tests, and computed data (e.g., Finite Element Analysis (FEA)).

APPENDIX

FIGURE I (A), (B) AREA MEASUREMENT OF MACRO-SHRINKAGE POROSITIES (I.E., ORIGINS OF FAILURE) ON BOTH BROKEN HALVES OF 22 TESTED FATIGUE SAMPLES

CA-6NM #3-7

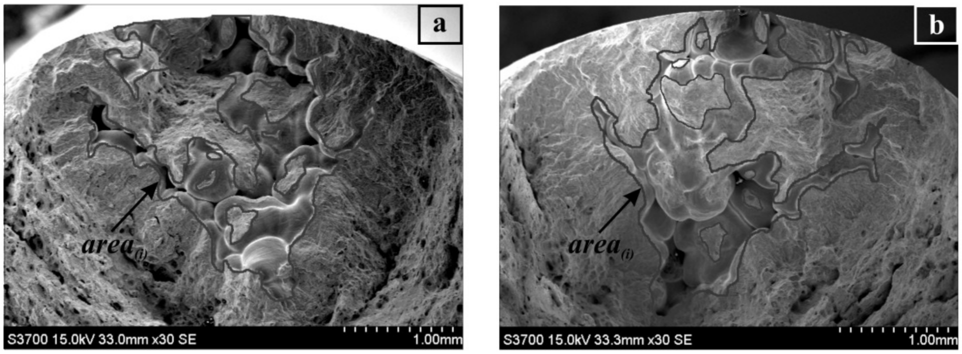

CA-6NM #3-20A

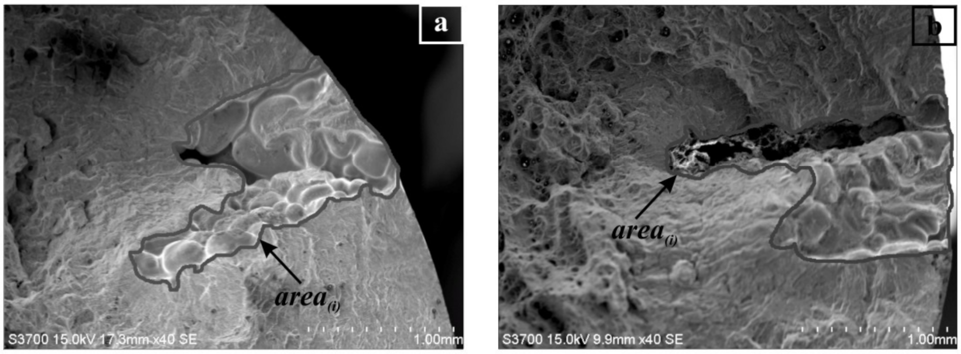

CA-6NM #3-19A

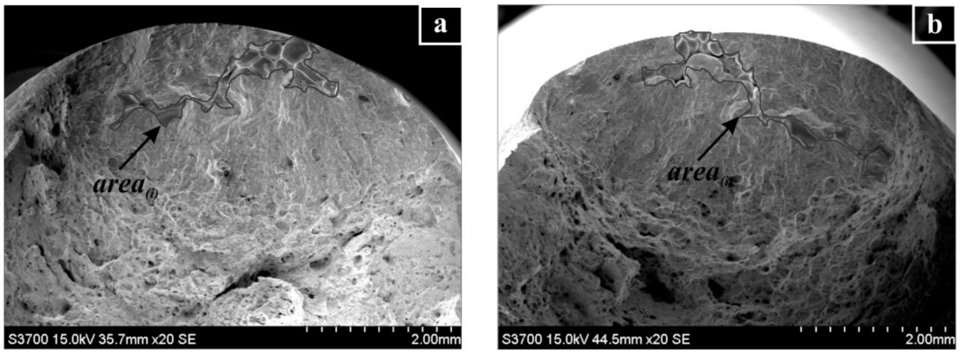

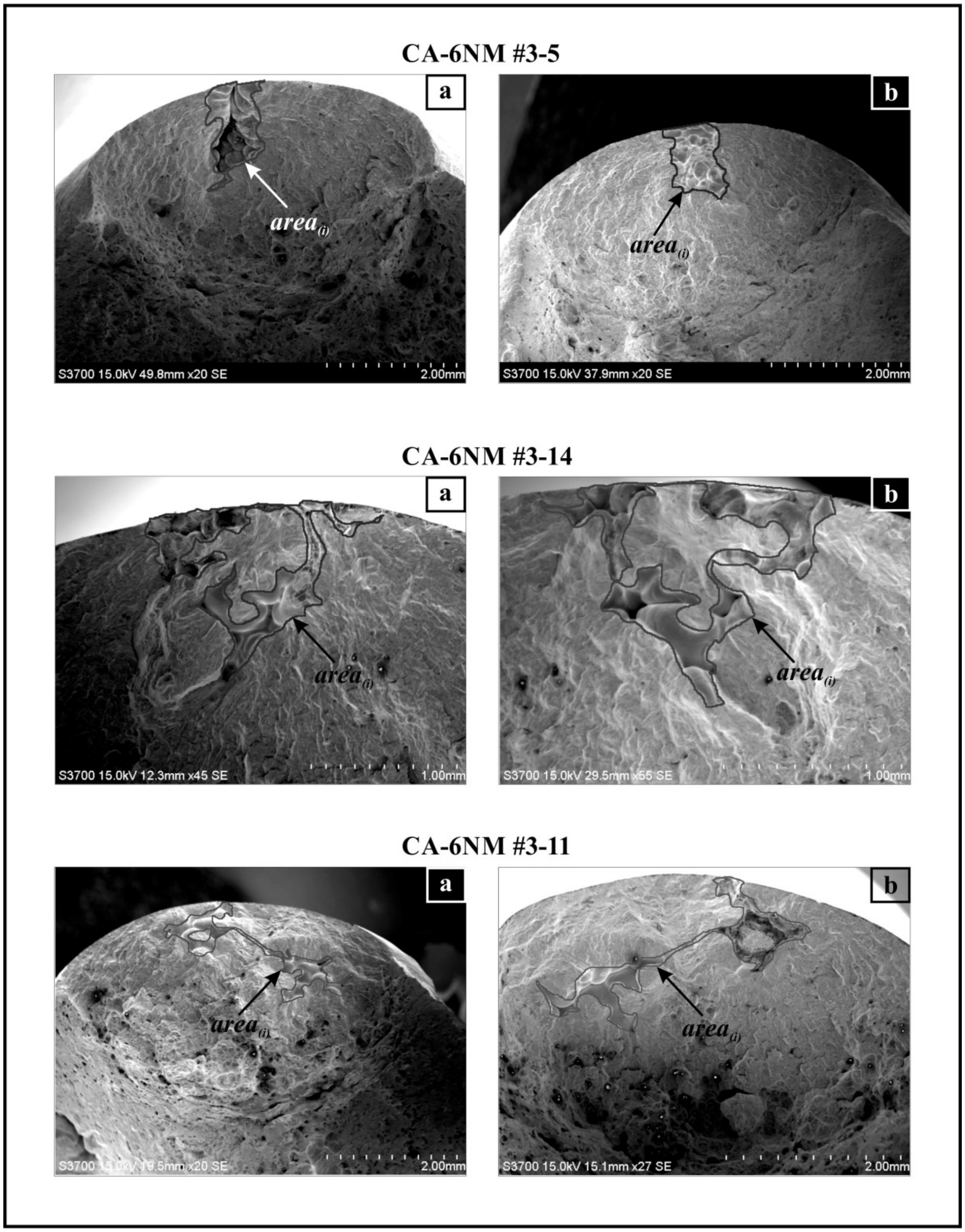
CA-6NM #3-5
a
area(i)
S3700 15.0kV 49.8mm x20 SE
2.00mm
b
area(i)
S3700 15.0kV 37.9mm x20 SE
2.00mm
CA-6NM #3-14
a
area(i)
S3700 15.0kV 12.3mm x45 SE
1.00mm
b
area(i)
S3700 15.0kV 29.5mm x55 SE
1.00mm
CA-6NM #3-11
a
area(i)
S3700 15.0kV 19.5mm x20 SE
2.00mm
b
area(i)
S3700 15.0kV 15.1mm x27 SE
2.00mm

CA-6NM #3-16

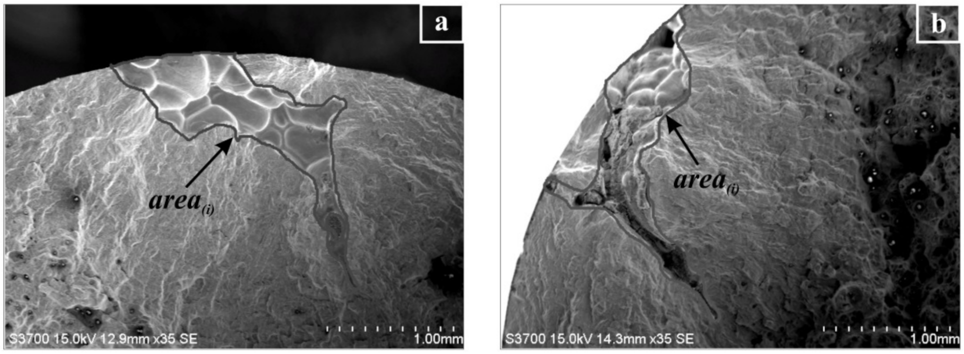

CA-6NM #3-21A

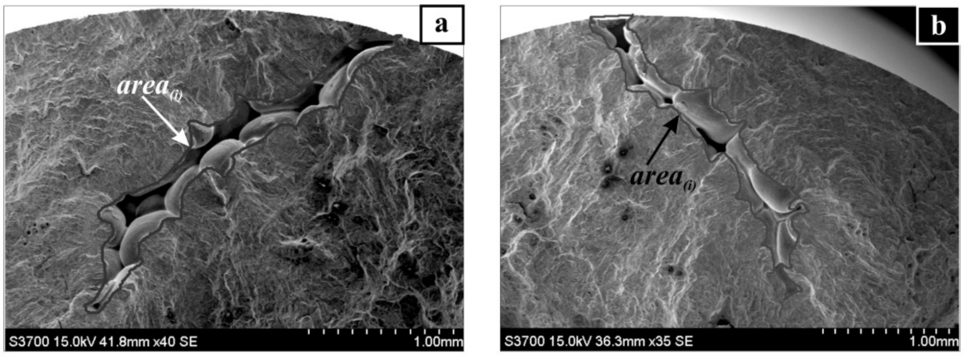

CA-6NM #3-9

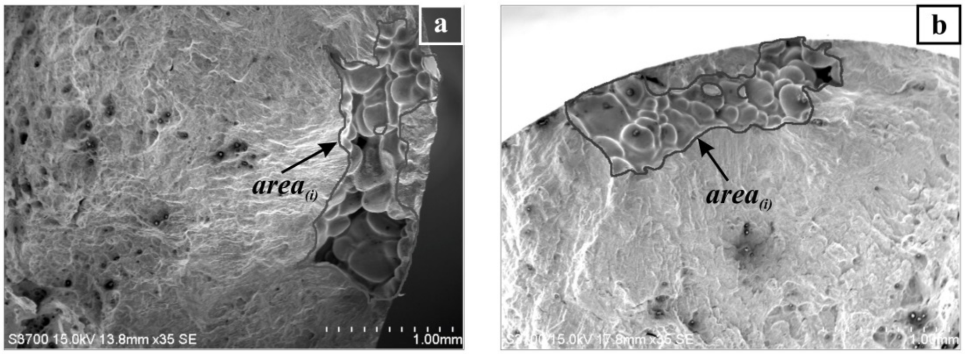

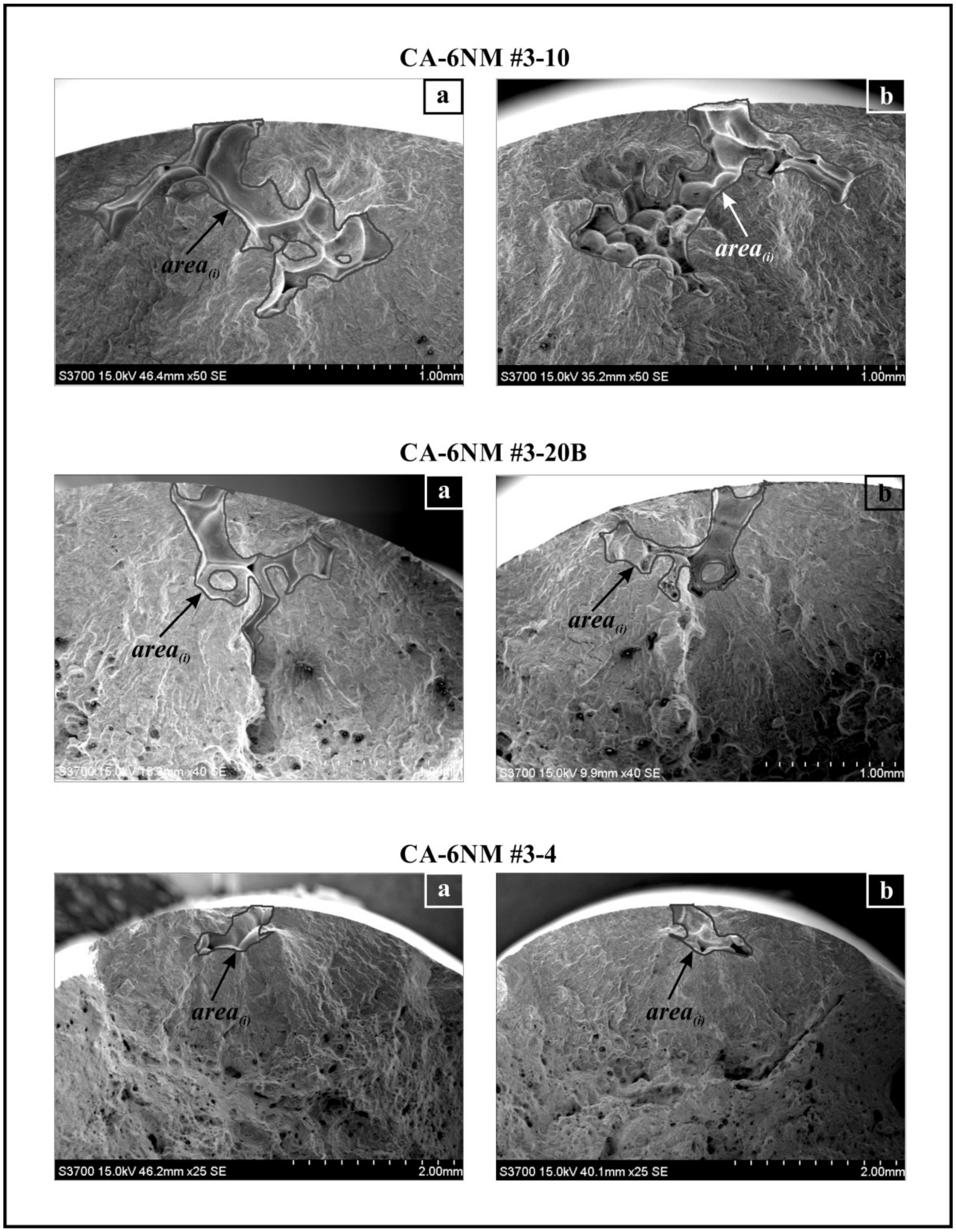
CA-6NM #3-10
a
area(i)
S3700 15.0kV 46.4mm x50 SE
1.00mm
b
area(i)
S3700 15.0kV 35.2mm x50 SE
1.00mm
CA-6NM #3-20B
a
area(i)
b
area(i)
S3700 15.0kV 9.9mm x40 SE
1.00mm
CA-6NM #3-4
a
area(i)
S3700 15.0kV 46.2mm x25 SE
2.00mm
b
area(i)
S3700 15.0kV 40.1mm x25 SE
2.00mm

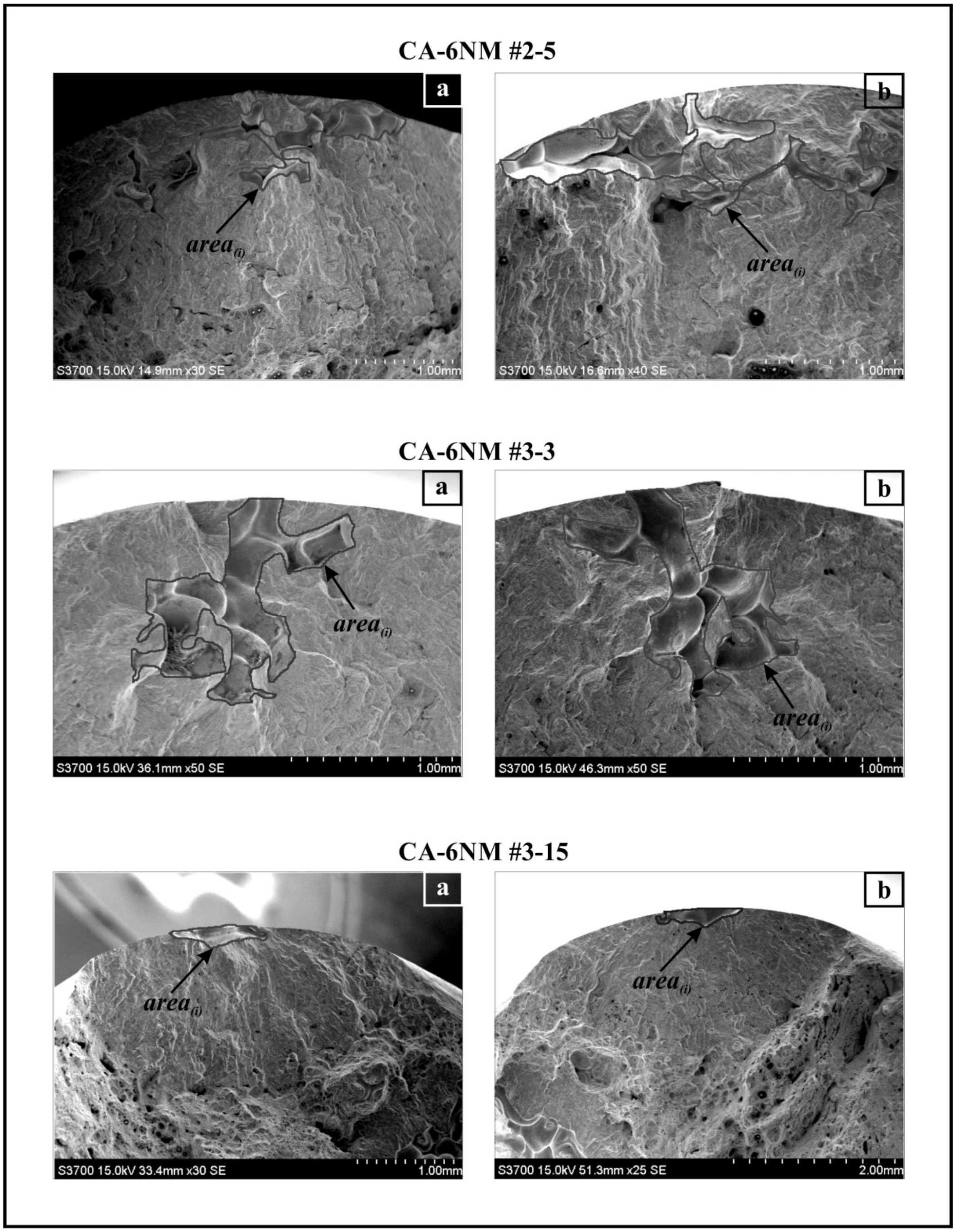
CA-6NM #2-5
a
area$_{(i)}$
S3700 15.0kV 14.9mm x30 SE
1.00mm
b
area$_{(i)}$
S3700 15.0kV 16.6mm x40 SE
1.00mm
CA-6NM #3-3
a
area$_{(i)}$
S3700 15.0kV 36.1mm x50 SE
1.00mm
b
area$_{(i)}$
S3700 15.0kV 46.3mm x50 SE
1.00mm
CA-6NM #3-15
a
area$_{(i)}$
S3700 15.0kV 33.4mm x30 SE
1.00mm
b
area$_{(i)}$
S3700 15.0kV 51.3mm x25 SE
2.00mm

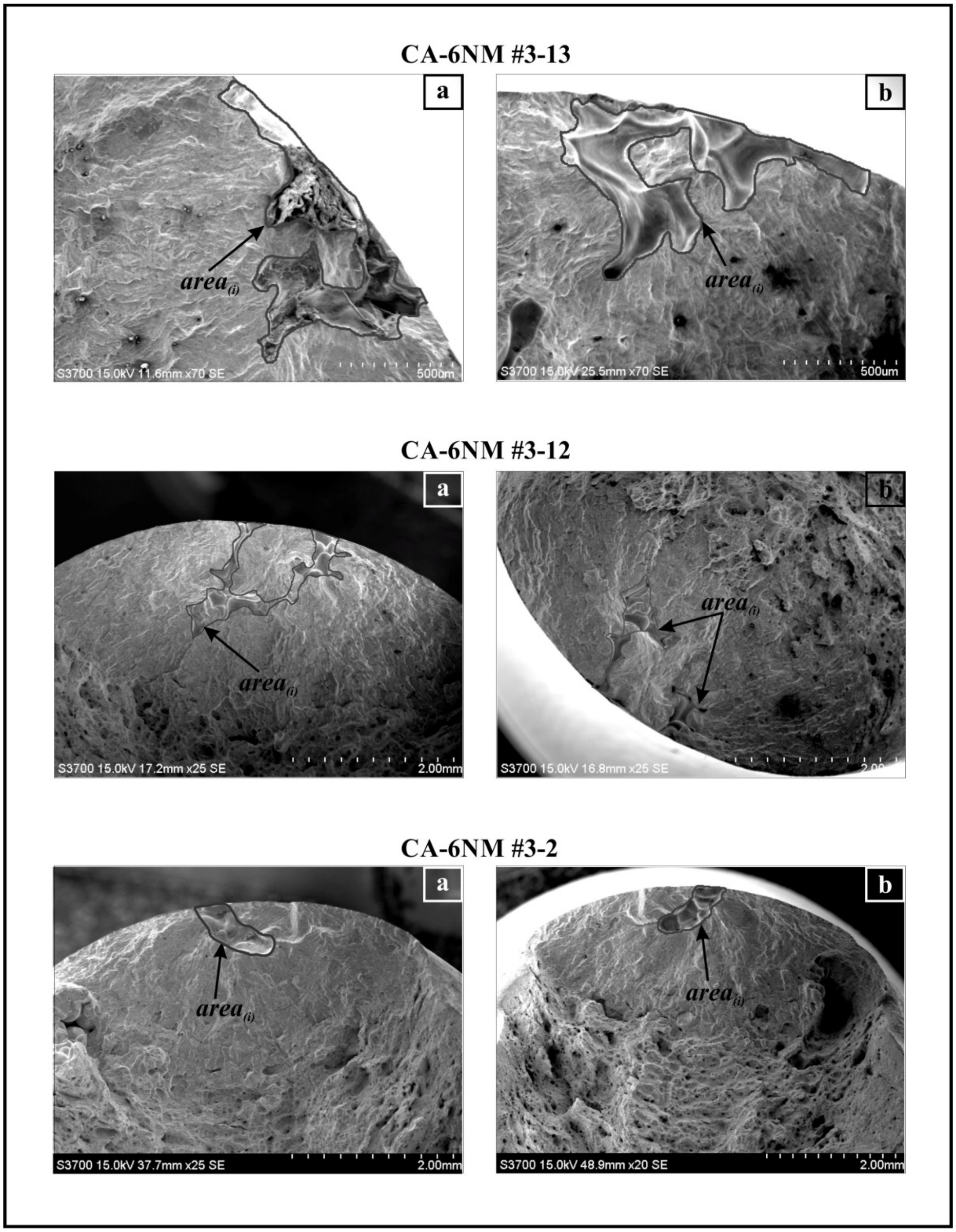
CA-6NM #3-13
a
area(i)
S3700 15.0kV 11.6mm x70 SE
500um
b
area(i)
S3700 15.0kV 25.5mm x70 SE
500um
CA-6NM #3-12
a
area(i)
S3700 15.0kV 17.2mm x25 SE
2.00mm
b
area(i)
S3700 15.0kV 16.8mm x25 SE
CA-6NM #3-2
a
area(i)
S3700 15.0kV 37.7mm x25 SE
2.00mm
b
area(i)
S3700 15.0kV 48.9mm x20 SE
2.00mm

CA-6NM #3-8

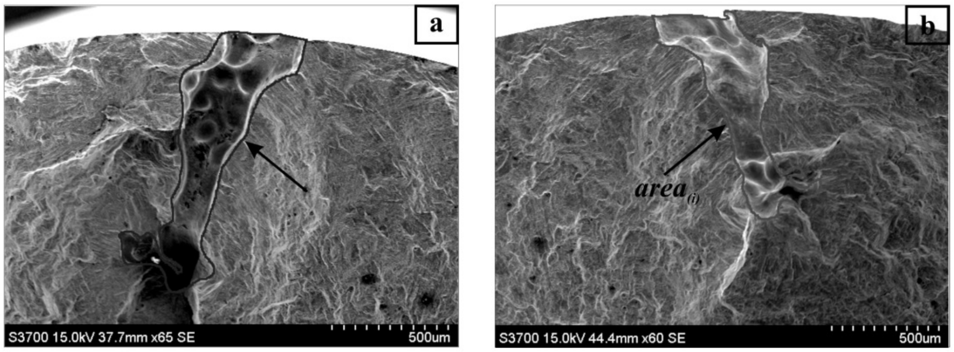

CA-6NM #3-21B

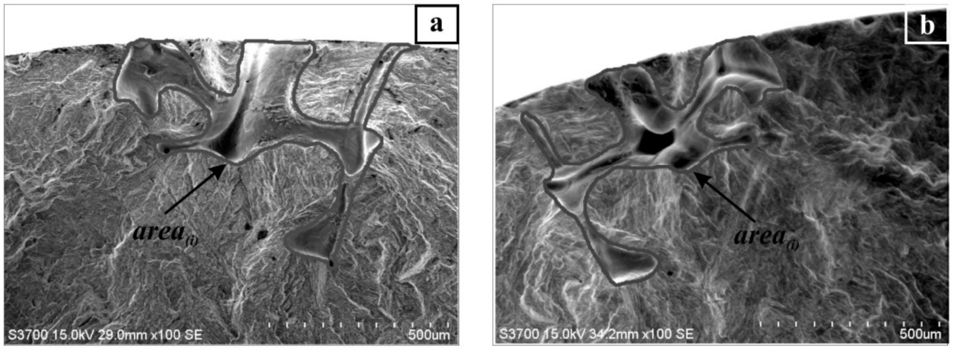

CA-6NM #3-6

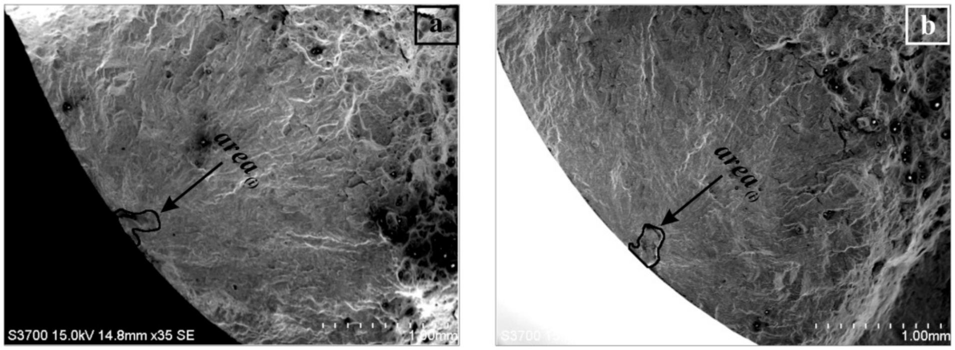

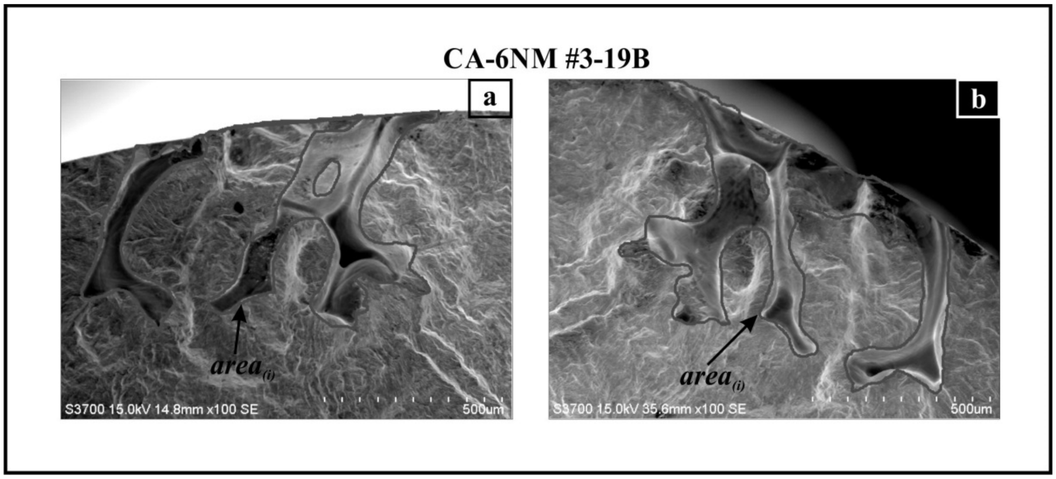
CA-6NM #3-19B
a
area$_{(i)}$
S3700 15.0kV 14.8mm x100 SE
500um
b
area$_{(i)}$
S3700 15.0kV 35.6mm x100 SE
500um

FIGURE II SHOWING THE VARIATION OF *Y(a)* FACTOR DURING FATIGUE CRACK PROPAGATION FOR 22 CA-6NM FATIGUE SAMPLES

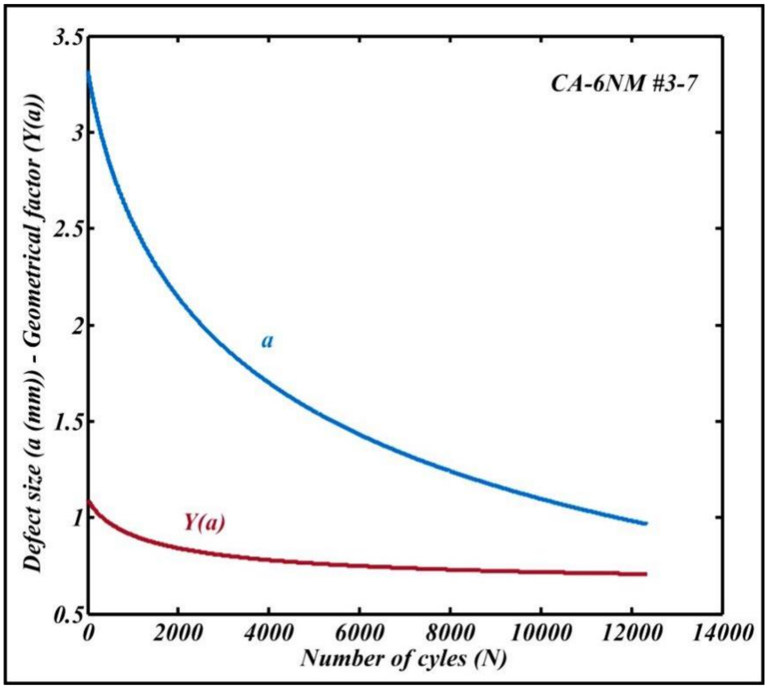

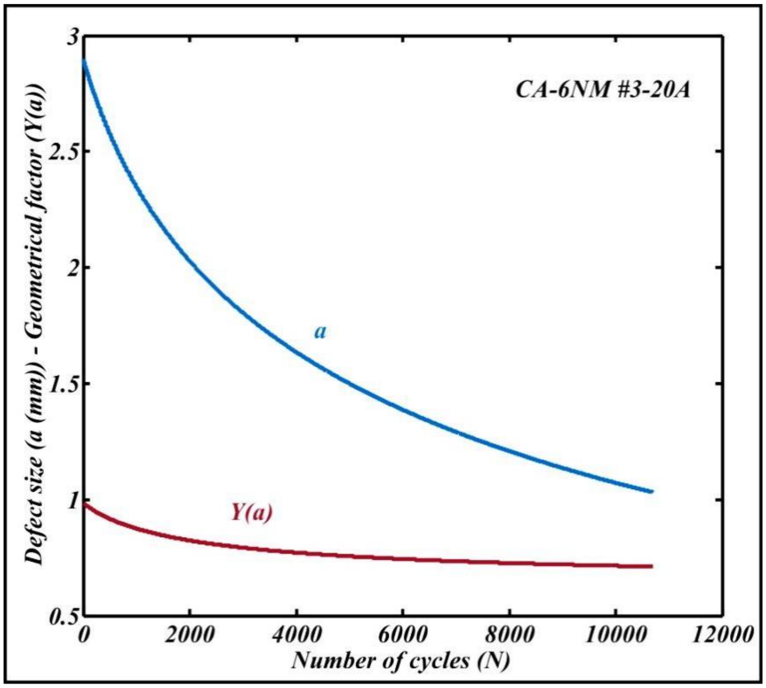

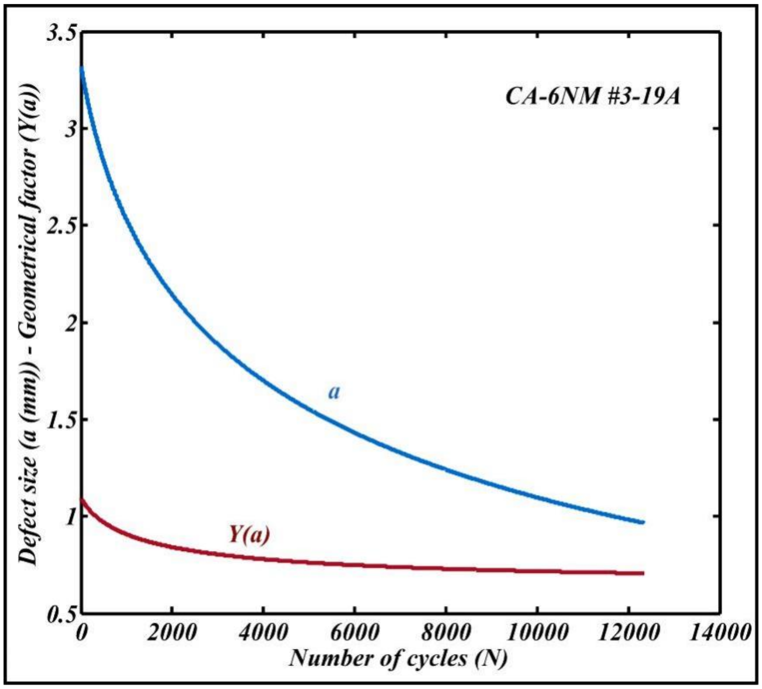
CA-6NM #3-19A
a
Y(a)
Defect size (a (mm)) - Geometrical factor (Y(a))
Number of cycles (N)
3.5
3
2.5
2
1.5
1
0.5
0
2000
4000
6000
8000
10000
12000
14000

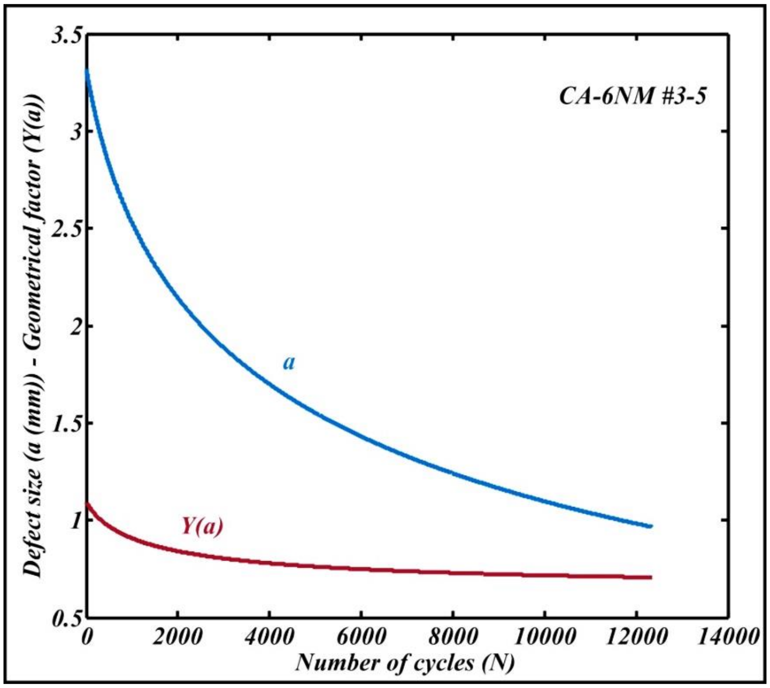
CA-6NM #3-5
a
Y(a)
Defect size (a (mm)) - Geometrical factor (Y(a))
Number of cycles (N)
3.5
3
2.5
2
1.5
1
0.5
0
2000
4000
6000
8000
10000
12000
14000

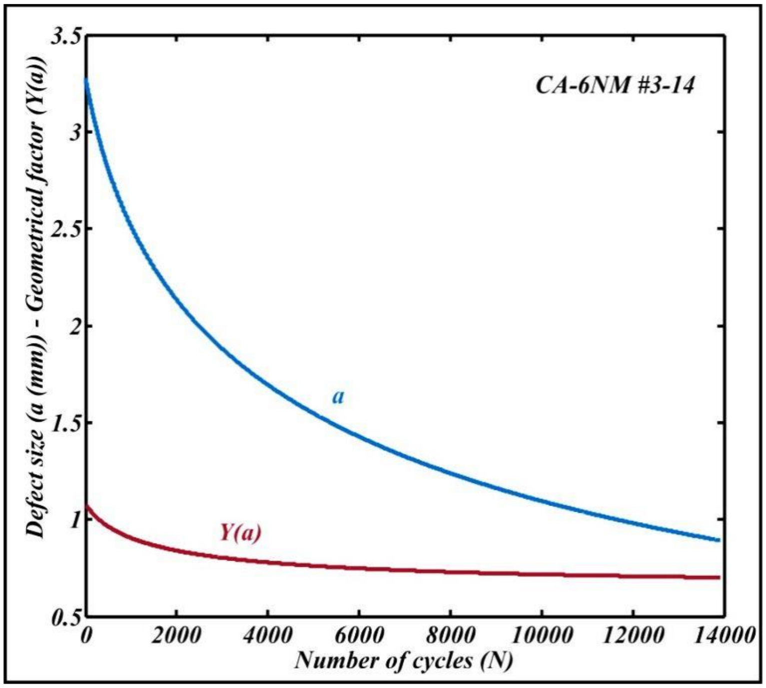
CA-6NM #3-14
Defect size (a (mm)) - Geometrical factor (Y(a))
Number of cycles (N)
a
Y(a)
3.5
3
2.5
2
1.5
1
0.5
0
2000
4000
6000
8000
10000
12000
14000

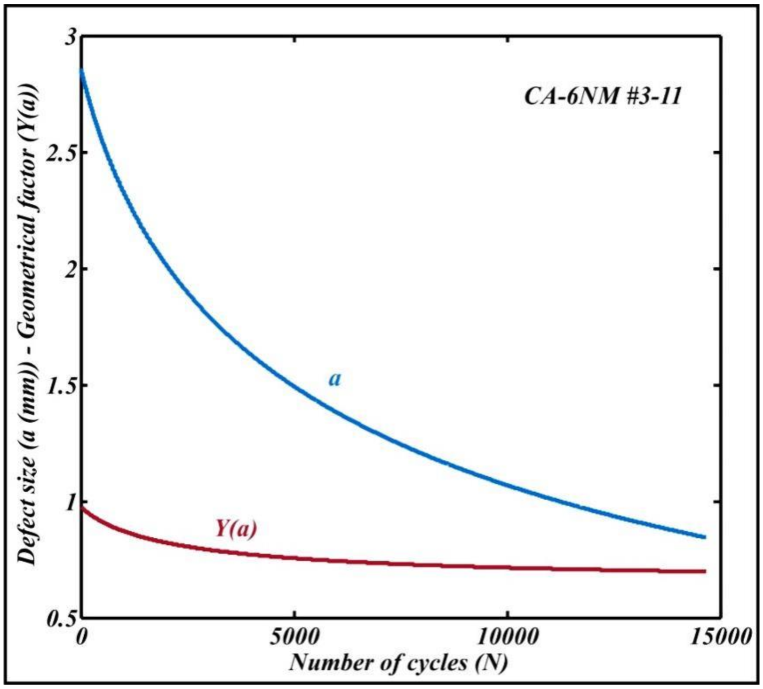
CA-6NM #3-11
Defect size (a (mm)) - Geometrical factor (Y(a))
Number of cycles (N)
a
Y(a)
3
2.5
2
1.5
1
0.5
0
5000
10000
15000

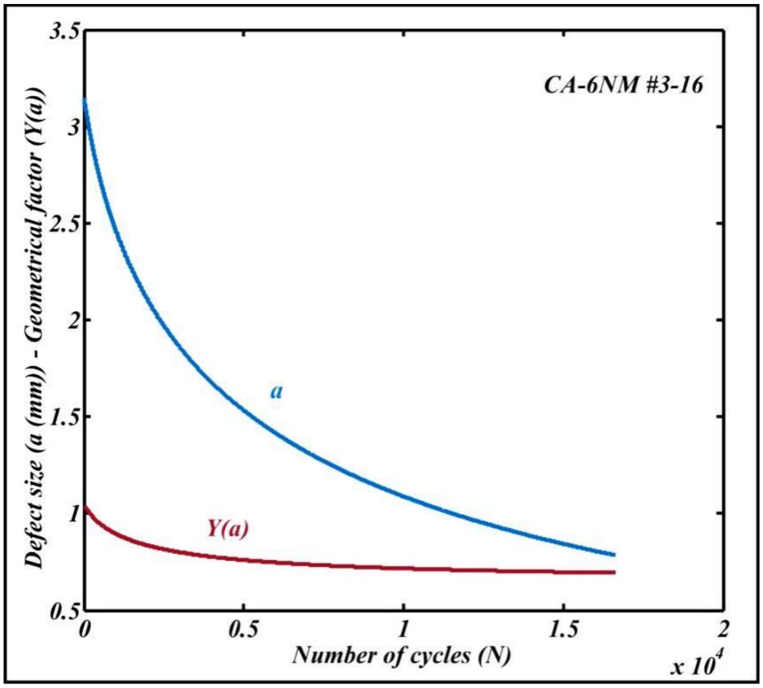
CA-6NM #3-16
Defect size (a (mm)) - Geometrical factor (Y(a))
3.5
3
2.5
2
1.5
1
0.5
a
Y(a)
0
0.5
1
1.5
2
Number of cycles (N)
x 10^4

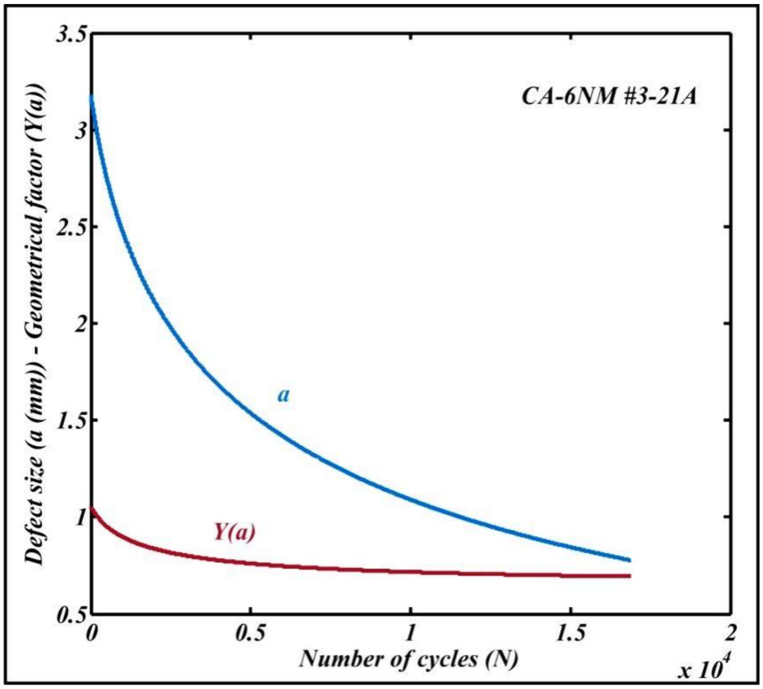
CA-6NM #3-21A
Defect size (a (mm)) - Geometrical factor (Y(a))
3.5
3
2.5
2
1.5
1
0.5
a
Y(a)
0
0.5
1
1.5
2
Number of cycles (N)
x 10^4

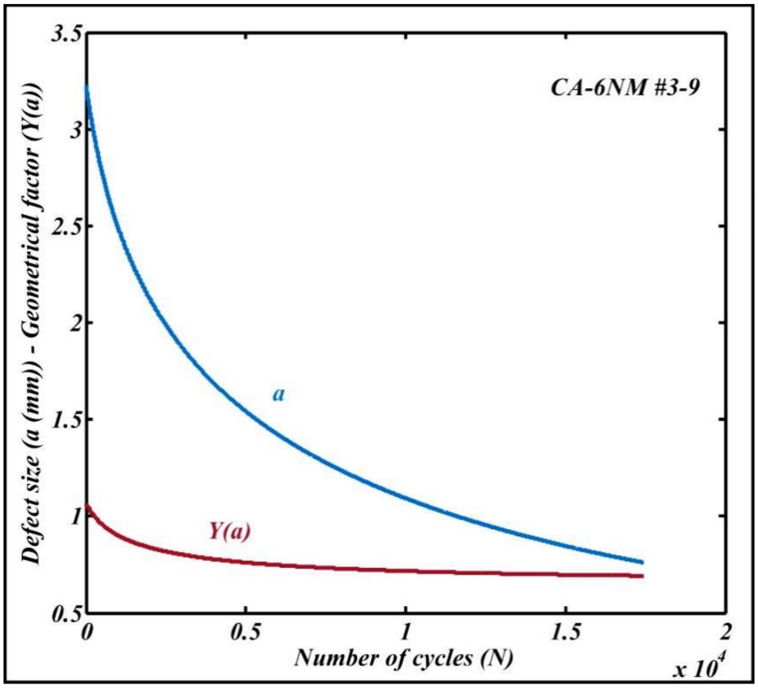
CA-6NM #3-9
Defect size (a (mm)) - Geometrical factor (Y(a))
Number of cycles (N)
x 10^4
a
Y(a)
3.5
3
2.5
2
1.5
1
0.5
0
0.5
1
1.5
2

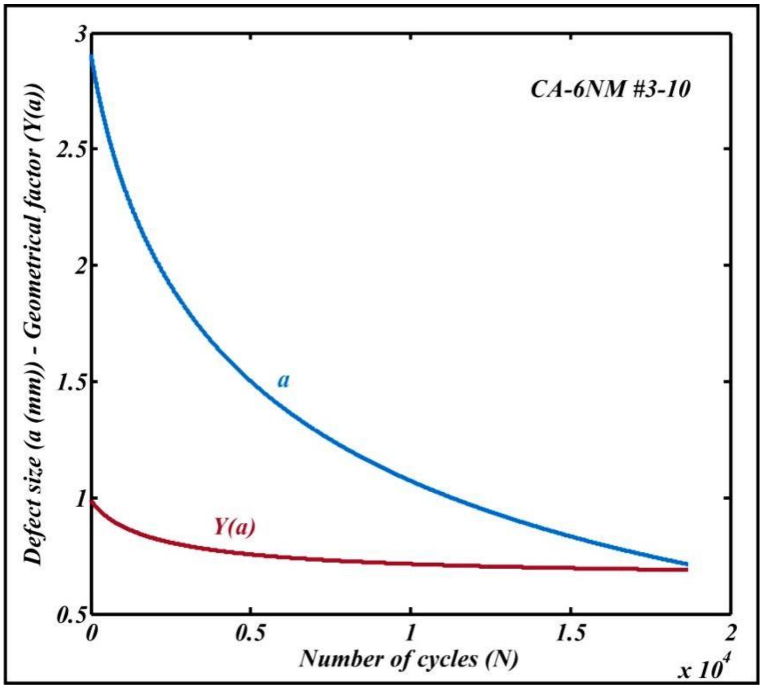
CA-6NM #3-10
Defect size (a (mm)) - Geometrical factor (Y(a))
Number of cycles (N)
x 10^4
a
Y(a)
3
2.5
2
1.5
1
0.5
0
0.5
1
1.5
2

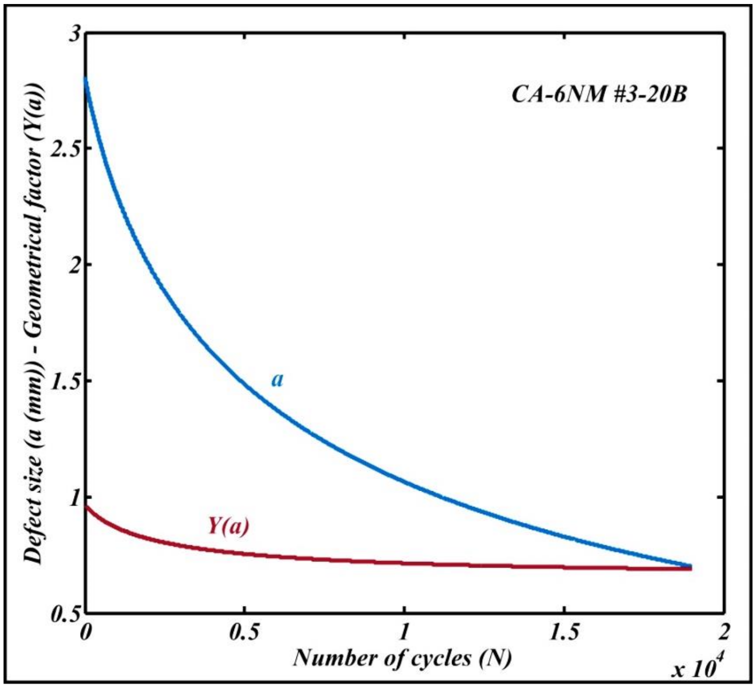
CA-6NM #3-20B
a
Y(a)
Defect size (a (mm)) - Geometrical factor (Y(a))
Number of cycles (N)
x 10^4
0.5
1
1.5
2
2.5
3
0
0.5
1
1.5
2

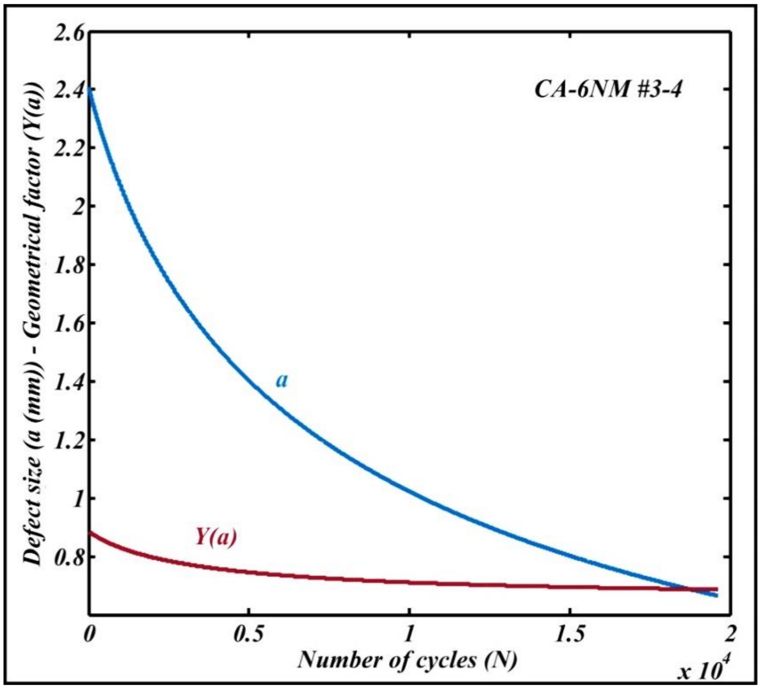
CA-6NM #3-4
a
Y(a)
Defect size (a (mm)) - Geometrical factor (Y(a))
Number of cycles (N)
x 10^4
0.8
1
1.2
1.4
1.6
1.8
2
2.2
2.4
2.6
0
0.5
1
1.5
2

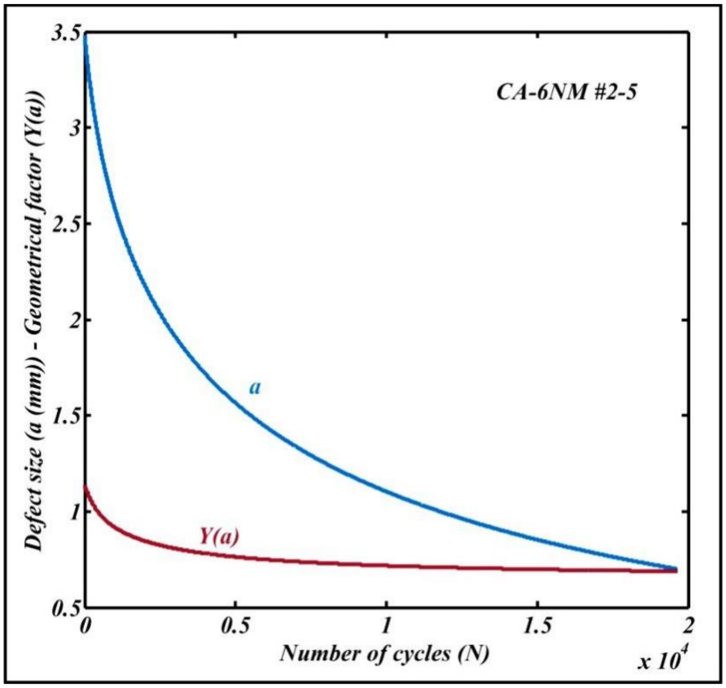
CA-6NM #2-5
a
Y(a)
Defect size (a (mm)) - Geometrical factor (Y(a))
Number of cycles (N)
x 10^4
3.5
3
2.5
2
1.5
1
0.5
0
0.5
1
1.5
2

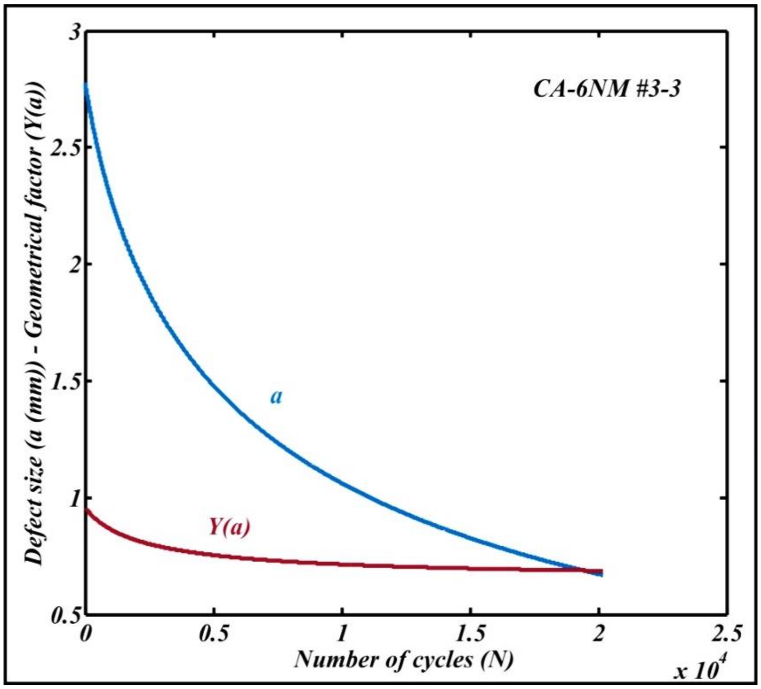
CA-6NM #3-3
a
Y(a)
Defect size (a (mm)) - Geometrical factor (Y(a))
Number of cycles (N)
x 10^4
3
2.5
2
1.5
1
0.5
0
0.5
1
1.5
2
2.5

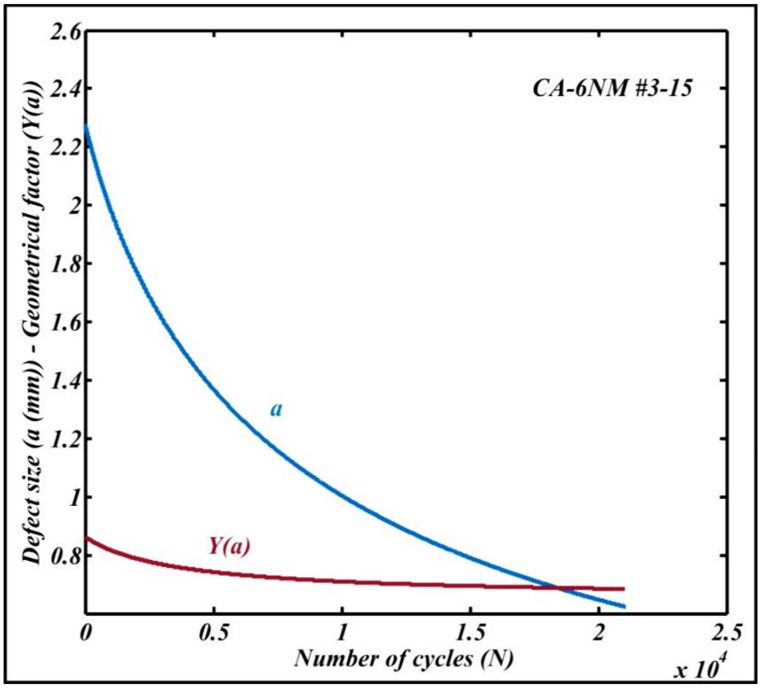
CA-6NM #3-15
a
Y(a)
Defect size (a (mm)) - Geometrical factor (Y(a))
Number of cycles (N)
x 10^4
2.6
2.4
2.2
2
1.8
1.6
1.4
1.2
1
0.8
0
0.5
1
1.5
2
2.5

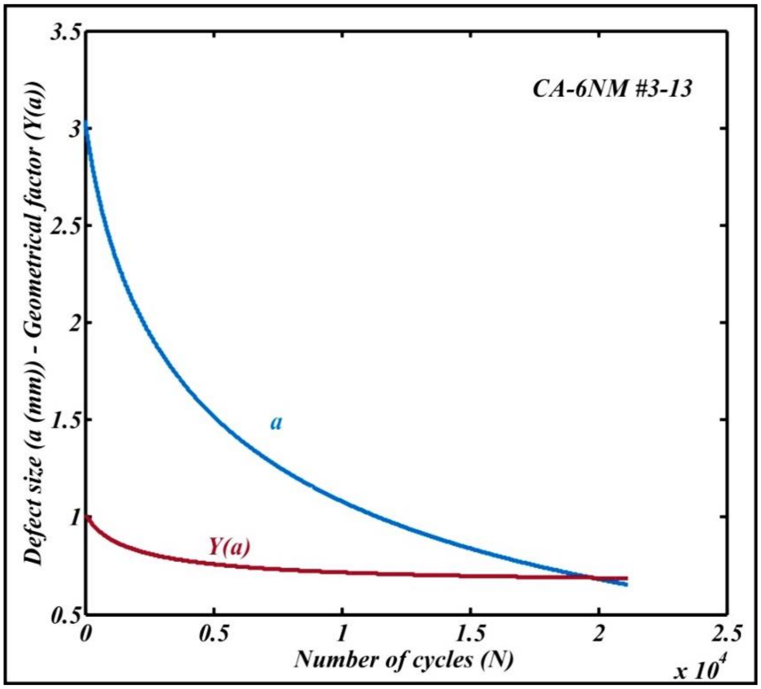
CA-6NM #3-13
a
Y(a)
Defect size (a (mm)) - Geometrical factor (Y(a))
Number of cycles (N)
x 10^4
3.5
3
2.5
2
1.5
1
0.5
0
0.5
1
1.5
2
2.5

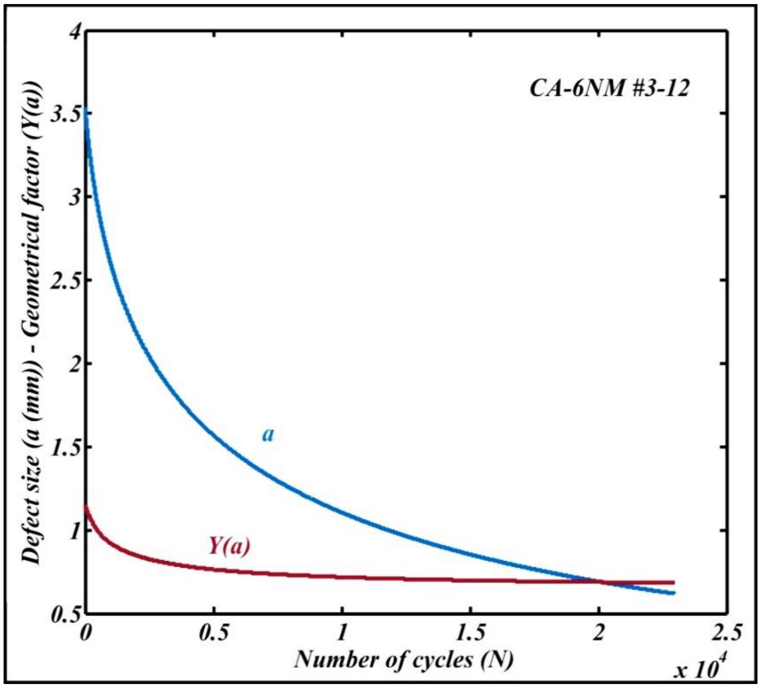
CA-6NM #3-12
Defect size (a (mm)) - Geometrical factor (Y(a))
Number of cycles (N)
x 10^4
a
Y(a)
0.5
1
1.5
2
2.5
3
3.5
4
0
0.5
1
1.5
2
2.5

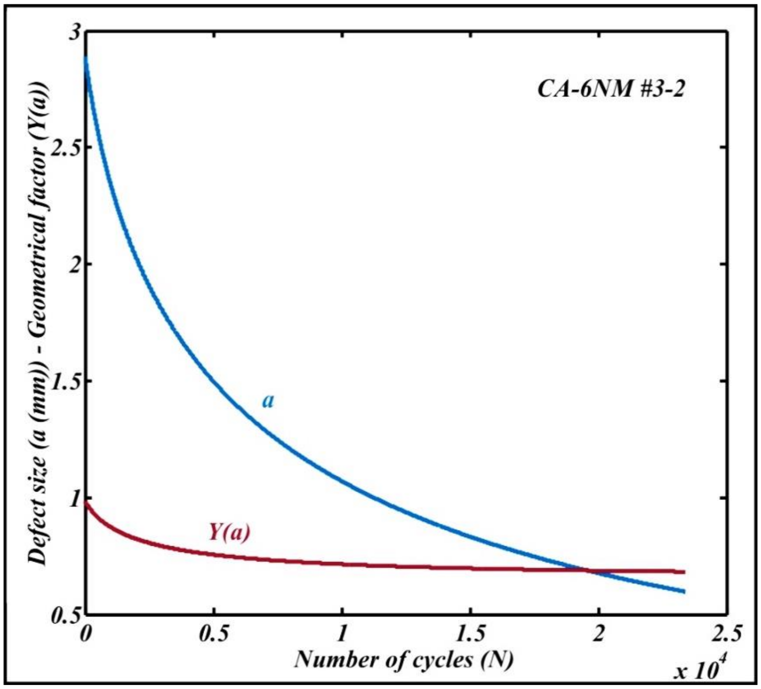
CA-6NM #3-2
Defect size (a (mm)) - Geometrical factor (Y(a))
Number of cycles (N)
x 10^4
a
Y(a)
0.5
1
1.5
2
2.5
3
0
0.5
1
1.5
2
2.5

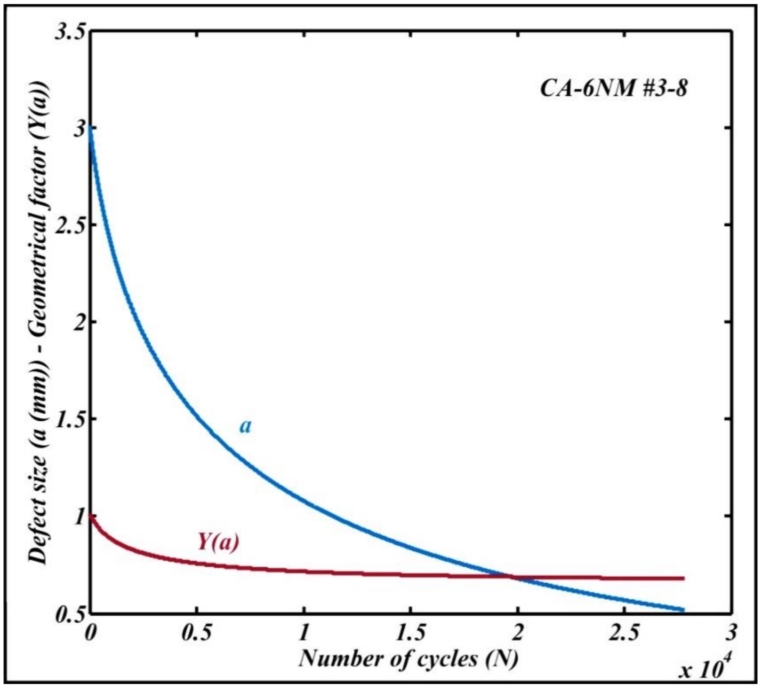
CA-6NM #3-8
Defect size (a (mm)) - Geometrical factor (Y(a))
3.5
3
2.5
2
1.5
1
0.5
a
Y(a)
0
0.5
1
1.5
2
2.5
3
Number of cycles (N)
x 10^4

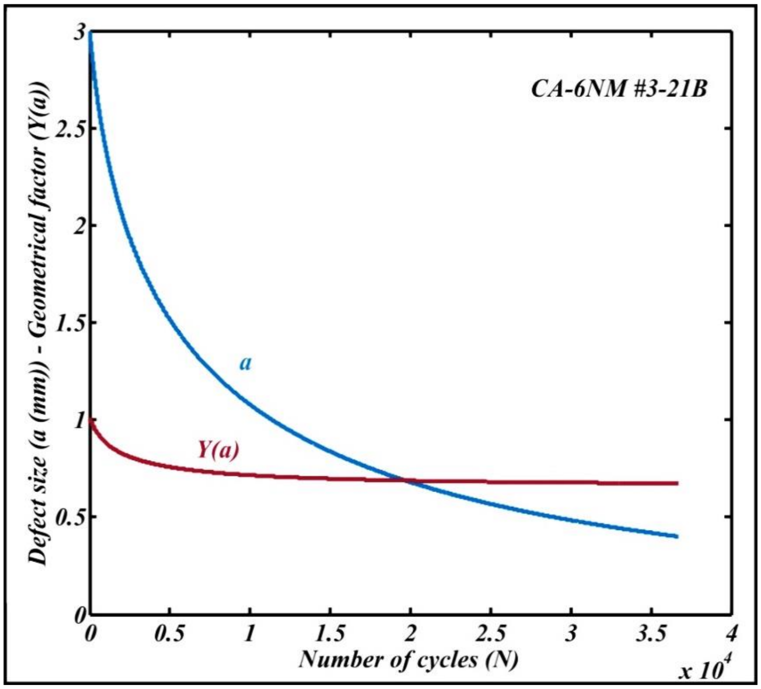
CA-6NM #3-21B
Defect size (a (mm)) - Geometrical factor (Y(a))
3
2.5
2
1.5
1
0.5
0
a
Y(a)
0
0.5
1
1.5
2
2.5
3
3.5
4
Number of cycles (N)
x 10^4

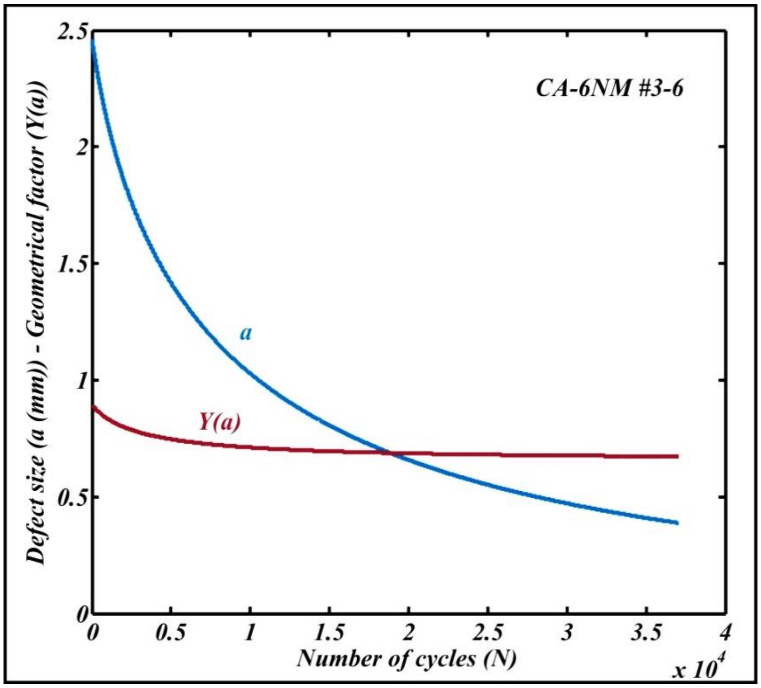
CA-6NM #3-6
a
Y(a)
Defect size (a (mm)) - Geometrical factor (Y(a))
Number of cycles (N)
x 10^4
0
0.5
1
1.5
2
2.5
3
3.5
4

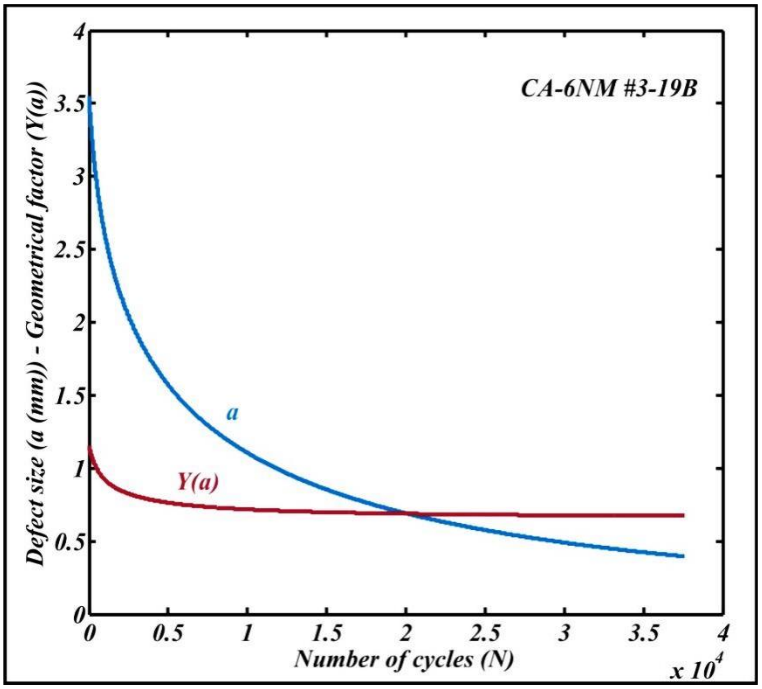
CA-6NM #3-19B
a
Y(a)
Defect size (a (mm)) - Geometrical factor (Y(a))
Number of cycles (N)
x 10^4
0
0.5
1
1.5
2
2.5
3
3.5
4

BIBLIOGRAPHY

Ammar, H. (2006). *Effect of casting imperfections on the fatigue properties of Aluminum-Silicon casting alloys.* (Doctoral thesis, Université du Québec à Chicoutimi, Chicoutimi, Canada).

ASM International. (2008). *Casting*. Vol. 15. ASM Handbook Committee. Materials Park, OH: ASM International.

ASM International. (2002). *Failure Analysis and Prevention*. Vol. 11. ASM Handbook Committee.

ASM International. (2009). *Casting design and performance.* Materials Park, OH: ASM International.

ASTM International. (2006). *Standard Specification for Castings, Iron-Chromium, Iron-Chromium-Nickel, Corrosion Resistant, for General Application.* ASTM Standard A743/A 743M - 06(2006)

ASTM International. (2014). *Standard Specification for Steel Castings Suitable for Pressure Service.* (2014). ASTM Standard A487/A487M - 14(2014)

ASTM International. (2004). *Standard Reference Radiographs for Steel Castings Up to 2 in. [51 mm] in Thickness,* ASTM Standard E446 – 98 (Reapproved 2004). West Conshohocken, PA: ASTM International.

ASTM International. (2004). *Standard Reference Radiographs for heavy-walled (2 to 4½ -in (51 to 114-mm)) steel castings,* ASTM Standard E186 – 98 (Reapproved 2004). West Conshohocken, PA: ASTM International.

ASTM International. (2007). *Standard Practice for Conducting Force Controlled Constant Amplitude Axial Fatigue Tests of Metallic Materials,* ASTM Standard E466 – 07, West Conshohocken, PA: ASTM International.

Bacaicoa, I., Wicke, M., Luetje, M., Zeismann, F., Brueckner-Foit, A., Geisert, A. & Fehlbier, M. (2017). Characterization of casting defects in a Fe-rich Al-Si-Cu alloy by microtomography and finite element analysis. *Engineering Fracture Mechanics,* 183, 159-169.

Behal, V. G. & Melilli, A. S. (1982). *Stainless Steel Casting. ASTM STP 756,* Philadelphia: American Society for Testing and Materials.

Bilmes, P. D., Solari, M. & Llorente, C. L. (2001). Characteristics and effects of austenite resulting from tempering of 13Cr–NiMo martensitic steel weld metals. *Materials Characterization*, 46(4), 285-296.

Björkblad, A. (2008). *Fatigue assessment of cast components: influence of cast defects.* (Doctoral thesis, KTH Royal Institute of Technology, Stockholm, Sweden).

Boromei, I., Ceschini, L., Morri, Al., Morri, An., Nicoletto. G. & Riva. E. (2010). Influence of the solidification microstructure and porosity on fatigue strength of Al-Si-Mg casting alloys. *Metallurgical Science and Technology,* 28 (2nd ed.), 18-24.

Briggs, C. W. (1969). *The effect of internal shrinkage discontinuities on the fatigue and impact properties of cast steel.* Ohio: Steel Founders' Society of America.

Briggs, C. W. (1966). *The effect of surface discontinuities on the fatigue properties of cast steel sections.* Ohio: Steel Founders' Society of America.

British Standards. (2005). *Guide to methods for assessing the acceptability of flaws in metallic structures.* BSI-BS 7910. London.

Brobély, A., Mughrabi, H., Eisenmeier G. & Höppel H. W. (2002). A finite element modelling study of strain localization in the vicinity of near-surface cavities as a cause of subsurface fatigue crack initiation. *International Journal of Fracture,* 115, 227-232.

Broek, D. (1988). *The Practical Use Of Fracture Mechanics* (1st ed.) [Kluwer Academic Publishers]. DOI: 10,1007/978-94-009-2558-8

Buffière, J. -Y, Maire, E., Adrien, J., Masse, J. -P. & Boller, E. (2010). In Situ Experiments with X ray Tomography: An Attractive Tool for Experimental Mechanics. *Experimental Mechanics,* 50, 289-305.

Campbell, J. (2011). *Complete Casting Handbook: Metal Casting Processes, Metallurgy, Techniques and Design* (1st ed.). Waltham, MA: Butterworth-Heinemann.

Cao, X. B., Zhao, J., Fan, J. H., Zhang, M. H., Shao, G. J. & Hua, Q. (2014). Influence of casting defects on fatigue behaviour of A356 aluminum alloy. *International Journal of Cast Metals Research,* 27(6), 362-368.

Carlo, J. M., Barbeitos, M. S. & Lasker, H. R. (2011). Quantifying complex shapes: Elliptical Fourier analysis of octocoral sclerites. *Biological Bulletin,* 220(3), 224-237. DOI: 10.1086/BBLv220n3p224

Cheng, J., Hort, N., Kainer, K. U. & Kwak, S. (2013). Effect of internal defects on tensile properties of A356 casting alloys. *22nd International Conference on Metallurgy and Materials, 2013, Brno, Czech Republic, May 15-17, 2013.*

Committee, Steel Founders' Society of America. *Steel Casting Handbook.* (2004). Supplement 8 High Alloy Data Sheets Corrosion Series.

Crane, R. L.& Matikas, T. E. (1998). Nondestructive testing, In Kutz, M. (2nd ed.). *Mechanical Engineer's Handbook,* (pp. 729-760). John Wiley & Sons, Inc.

Dabayeh, A. (1998). *The role of casting defects in the fatigue behavior of notched cast Aluminum alloys.* (Doctoral thesis, University of Waterloo, Waterloo, Canada).

Davis, J. R. (2000). Alloy digest sourcebook: Stainless steels. *Introduction to stainless steels.* (pp. 1-6). Materials Park, OH: ASM International.

Denys, R. (2008). Interaction between material properties, inspection accuracy and defect acceptance levels in strain based pipeline design, In Pluvinage, G. & Elwany, M. H. *Safety, Reliability and Risks Associated with Water, Oil and Gas Pipelines,* (pp. 45-64). Springer.

Dowling, N. E. (2013). *Mechanical Behavior of Materials, Engineering Methods for Deformation, Fracture, and Fatigue* (4th ed.). Pearson Education.

Duckworth, W. E. & Ineson, E. (1963). The effects of externally introduced alumina particles on the fatigue life of En24 steel. *In: Clean steel 77, Iron Steel Inst.,* 87-103.

Ferreño, D., Álvarez, J. A., Ruiz, E., Méndez, D., Rodríguez, L. & Hernández, D. (2011). Failure analysis of a Pelton turbine manufactured in soft martensitic stainless steel casting. *Engineering Failure Analysis,* 18, 256-270.

Ferreira. T. & Rasband, W. (2012). *ImageJ User Guide IJ 1.46r.* (Revised ed.).

Flores, M., Urquiza, G. & Rodríguez, J. M. (2012). A fatigue analysis of a hydraulic Francis turbine runner. *World Journal of Mechanics,* 2, 28-34. DOI:10.4236/wjm.2012.21004

Forman, R. G. & Shivakumar, V. (1986). Growth Behavior of Surface Cracks in the Circumferential Plane of Solid and Hollow Cylinders. *Fracture Mechanics: Seventeenth Volume,* In Underwood, J. H., Chait, R., Smith, C. W., Wilhelm, D. P., Andrews, W.A. & Newman, J. C. (Eds.). 17. (pp. 59-74). ASTM STP 905, Philadelphia.

Forman, R. G., Shivakumar, V., Mettu, S. R. & Newman, Jr. J. C. (1998). Fatigue Crack Growth Computer Program 'NASGRO' Version 3.00, Reference Manual. JSC-22267B, NASA/Lyndon B. Houston, TX: Johnson Space Center.

Fredriksson, H. & Åkerlind U. (2006). *Materials Processing During Casting*. ISBN: 0-470-01514-4

Gao, Y. X., Yi, J. Z., Lee, P. D. & Lindley, T. C. (2004). The effect of porosity on the fatigue life of cast aluminium-silicon alloys. *Fatigue & Fracture of Engineering Materials & Structures,* 27, 559-570.

Ginzel, E. A., Thomson, R. & Ginzel, R. K. (2011). A qualification process for phased-array UT using DNV RP-F118 Guidelines. *e-Journal of Nondestructive Testing (NDT) (NDT.net Journal),* 8, 1-12. ISSN: 1435-4934

Glasbey, C. A, Horgan, G. W. & Wiley, J. (1994). *Image Analysis for the Biological Sciences.* Farnborough, Hampshire: National Remote Sensing Centre Ltd.

Gosh, A. (2001). Segregation in cast products. *Sadhana (Indian Academy of Sciences),* 26(1), 5-24. DOI: 10.1007/BF02728476

Griffith, A. A. (1921). The phenomena of rupture and flow in solids. *Philosophical Transactions of the Royal Society of London,* A221, 163-198.

Hardin, R. & Beckermann, C. (2012). Effect of porosity on deformation, damage, and fracture of cast steel. *Supplemental Proceedings: Materials Properties, Characterization, and Modeling TMS (The Minerals, Metals & Materials Society),* 2, 217-224.

Hellier, C. J. (2013). *Handbook of nondestructive evaluation* (2nd ed.). New York, NY, USA: McGraw-Hill Companies, Inc.

Hertzberg, R. W. (1996). *Deformation and Fracture Mechanics of Engineering Materials* (4th ed.). John Wiley & Sons, Inc.

Huth, H. J. (2005). *Fatigue design of hydraulic turbine runners.* (Doctoral thesis, Norwegian University of Science and Technology (NTNU), Trondheim, Norway).

Inglis, C. E. (1913). Stress in a plate due to the presence of cracks and sharp corners. *Trans. Inst. Nav. Archit,* London 55, 219-230.

Irwin, G. R. (1957). Analysis of stresses and strain near the end of a crack traversing a plate. *Transactions of the ASME Series E: Journal of Applied Mechanics,* 24(3), 361-364.

Iwabuchi, Y. (1987). Temper embrittlement of type l3Cr-4Ni cast steel. *Transactions of the Iron and Steel Institute of Japan,* 27(3), 211-217.

Iwabuchi, Y. & Sawada, S. (1982). Metallurgical characteristics of a large hydraulic runner casting of type 13Cr–Ni stainless steel. In Behal, V. G. & Melilli, A. S. (Eds), *Stainless steel casting ASTM STP 756,* 332-354. Philadelphia: American Society for Testing and Materials.

Iwabuchi, Y. (2003). Factors affecting on mechanical properties of soft martensitic stainless steel casting. *JSME International,* 46(3), 441-446.

Jayet-Gendrot, S., Gilles, P. & Migne´, C. (2000). Behavior of duplex stainless steel casting defects under mechanical loadings. *Nuclear Engineering and Design,* 197, 141-153.

Kim, J. Y., Lee, J. H. & Nahm, S. H. (2006). Statistical analysis of casting defects in microstructure for understanding the effect on fatigue property of 17-4PH stainless steel. *Key Engineering Materials,* 321-323, 1503-1506.

Kim, J. W., Kim, Y. S. & Park, C. Y. (2002). Failure analysis of cracking at volute tongues of feedwater pump castings. *Engineering Failure Analysis*, 9, 17-30.

Kjølle, A. (2001). *Hydropower in Norway.* Trondheim: Norwegian University of Science and Technology.

Kubota, T. & Tanaka, O. (1984). Recent Quality Control Of 13Cr-4Ni Cast Steel Runner. *Fuji Electric Review.* 30(4), 151-157.

Kumar, G. R., Raman, S. G. S. & Pathak, S. D. (2004). Generation of Kitagawa-Takahashi type plots for SA 333 grade 6 ferritic steel. *Transactions of the Indian Institue of Metals,* 57(5), 521-524.

Larson, J. A. & Fisher, R. (1979). The effect of heat treatment and melt practice on the impact properties of CA-6NM steel. *AFS Trans,* 63, 113-126.

Li, P., Lee, P. D., Maijer, D. M. & Lindley, T. C. (2009). Quantification of the interaction within defect populations on fatigue behavior in an aluminum alloy. *Acta Materialia,* 57, 3539-3548. DOI: 10.1016/j.actamat.2009.04.008

Liu, W., Zhai, W. H. & Zhao, J. F. (2016). Influence of shrinkage porosity on fatigue performance of iron castings and life estimation method. *Research & Development, China Foundry,* 13(1), 47-53.

Llewellyn, D. & Hudd, R. (1998). Stainless steels. III (Eds), *Steels: Metallurgy and applications.* (pp. 291-379). Woburn, MA: Butterworth-Heinemann.

Lozev, M. G., Spencer, R. L. & Hodgkinson, D. (2005). Optimized inspection of thin-walled pipe welds using advanced ultrasonic techniques. *Journal of Pressure Vessel Technology,* 127, 237-43.

Marrow, T. J., Buffière, J. –Y, Withers, P. J., Johnson, G. Engelberg, D. (2004). High resolution X-ray tomography of short fatigue crack nucleation in austempered ductile cast iron. *International Journal of Fatigue,* 26, 717-725.

Martz, H. E. Jr. & Logan, C. M. (2002). Radiography. In Shull, P. J., (Ed.), *Nondestructive evaluation: Theory, techniques, and applications.* (pp. 470-618). New York: Marcel Dekker Inc.

Mathis, R. (1987). Initiation and early growth mechanisms of corrosion fatigue cracks in stainless steels. *Journal of Material Science,* 22, 907-914.

McDowell, D. L., Gall, K., Horstemeyer, M. F. & Fan, J. (2003). Microstructure-based fatigue modelling of cast A356-T6 alloy. *Engineering Fracture Mechanics,* 70, 49-80.

McMaster, R. L. (1959). *The nondestructive testing handbooks* (2nd ed.). Columbus, OH: American society for nondestructive testing.

Meimandi, S., Vanderesse, N., Thibault, D., Bocher, P. & Viens, M. (2017). Macro-defects characterization in cast CA-6NM martensitic stainless steel. *Materials Characterization,* 124, 31-39.

Miedlar, P. C., Berens, A. P., Gunderson, A & Gallagher, J. P. (2002). Section 11.3: Selected Stress Intensity Factor Cases. *Analysis and Support Initiative for Structural Technology (ASIST) - USAF Damage Tolerant Design Handbook.* Dayton, OH: University of Dayton Research Institute.

Moore, H. D. (1981). *Materials and Processes for NDT Technology.* The American Society for Nondestructive Testing (ASNT). ISBN: 0-931403-06-5

Mu, P., Nadot, Y., Nadot-Martin, C., Chabod, A., Serrano-Munoz , I. & Verdu, C. (2014). Influence of casting defects on the fatigue behavior of cast aluminum AS7G06-T6. *International Journal of Fatigue,* 63, 97-109.

Murakami, Y. (2002). Chapter 2: Stress Concentration, *Metal fatigue: effects of small defects and non-metallic inclusions* (1st ed.). (pp. 11-24). Oxford: Elsevier Science Ltd.

Murakami, Y. & Endo, M. (1994). Effects of defects, inclusions and inhomogeneities on fatigue strength. *International Journal of Fatigue,* 16(3), 163-182.

Nadot, Y., Mendez, J., Ranganathan, N. & Beranger, A. S. (1999). Fatigue life assessment of nodular cast iron containing casting defects. *Fatigue & Fracture of Engineering Materials & Structures,* 22(4), 289-300.

Nicholas, T. (2006). Chapter 5: Notch Fatigue. In Nicholas T (1st ed.), *High Cycle Fatigue: A Mechanics of Materials Perspective.* (pp. 213-254). Oxford: Elsevier Science Ltd.

Nicoletto, G., Anzelottia, G. & Konečná, R. (2010). X-ray Computed Tomography vs. Metallography for Pore Sizing and Fatigue of Cast Al-alloys. *Procedia Engineering,* 2, 547-554.

Nicoletto, G., Konečná, R. & Fintova, S. (2012). Characterization of microshrinkage casting defects of Al-Si alloys by X-ray computed tomography and metallography. *International Journal of Fatigue,* 41, 39-46. DOI: 10.1016/j.ijfatigue.2012.01.006

Ødegard, J. A. & Pedersen, K. (1984). (Report No. 940811). Warrendale, PA: Society of Automotive Engineers.

Outokumpu stainless steel AB. (2013). *Handbook of stainless steel.* Espoo, Finland: Outokumpu Oyj.

Paris, P. C, M. P. Gomez & W. E. Anderson. (1961). A rational analytical theory of fatigue. *The Trend of Engineering,*13, 9-14.

Pehlke, R. D. (1988). Formation of Porosity during Solidification of Cast Metals. *Foundry Processes: Their Chemistry and Physics.* (pp. 427-445). Warren, MICH, USA.

Saeed, R. A., Galybin, A. N. & Popov, V. (2010). Modelling of flow-induced stresses in a Francis turbine runner. *Advances in Engineering Software,* 41, 1245-1255.

Schijve, J. (1977). *Internal fatigue cracks growing in vacuum* (Report-RL 240). Delft: Delft University of Technology, Department of Aerospace Engineering.

Schindelin, J., Arganda-Carreras, I., Frise, E., Kaynig, V., Longair, M., Pietzsch, T. et al. (2012). Fiji: an open-source platform for biological-image analysis. *Nature Methods,* 9(7), 676-682.

Schneider, C. A., Rasband, W. S. & Eliceiri, K. W. (2012). NIH Image to ImageJ: 25 years of image analysis. *Nature Methods,* 9, 671-675.

Serrano-Munoz, I., Buffière, J. –Y. & Verdu, C. (2018). Casting defects in structural components: Are they all dangerous? A 3D study. *International Journal of Fatigue*, 117, 471-484.

Sigl, K. M., Hardin, R. A., Stephens, R. I. & Beckermann, C. (2004). Fatigue of 8630 cast steel in the presence of porosity. *International Journal of Cast Metals Research,* 17(3), 130-146. DOI: 10.1179/136404604225020588

Skallerud, B., Iveland, T. & Härkegård, G. (1993). Failure life assessment of Aluminium alloys with cast defects. *Engineering Failure Mechanics,* 44(6), 857-874.

Small, K. B., Englehart, D. A. & Christman, T. A. (2008). Guide to etching special alloys. *Advanced Materials & Processes,* 32-37.

Song, Y. Y., Ping, D. H., Yin, F. X., Li X. Y. & Li, Y. Y. (2010). Microstructural evolution and low temperature impact toughness of a Fe–13%Cr–4%Ni–Mo martensitic stainless steel. *Materials Science and Engineering A,* 527, 614-618.

Stefanescu, D. M. (2009). *Science and engineering of casting solidification* (2nd ed.). Columbus, OH: Springer.

Stephens, R. I., Fatemi, A., Stephens, R. R. & Fuchs, H. O. (2001). *Metal fatigue in Engineering* (2nd ed.). John Wiley & Sons, Inc.

Stiénon, A., Fazekas, A., Buffière, J. –Y., Vincent, A., Daguier, P. & Merchi, F. (2009). A new methodology based on X-ray micro-tomography to estimate stress concentrations around inclusions in high strength steels. *Materials Science and Engineering A,* 513-514, 376-383.

Tabatabae, B. A., Ashrafizadeh, F. & Hassanli, A. M. (2011). Influence of retained austenite on the mechanical properties of low carbon martensitic stainless steel castings. *ISIJ International,* 51(3), 471-475.

Taylor, D. (1988). *Fatigue Thresholds*. Trinity College, Dublin: Butterworth.

Thibault, D., Gagnon, M. & Godin, S. (2015). The effect of materials properties on the reliability of hydraulic turbine runners. *International Journal of Fluid Machinery and Systems,* 8(4), 254-263. DOI: 10.5293/IJFMS.2015.8.4.254

Thibault, D., Bocher, P., Thomas, M., Lanteigne, J., Hovington, P. & Robichaud, P. (2011). Reformed austenite transformation during fatigue crack propagation of 13%Cr–4%Ni stainless steel. *Materials Science and Engineering A,* 528, 6519-6526.

Thomas, B. G. (2000). Chapter 14: Metals Processing, *Structure, processing, and properties of engineering materials*. In J. Adams, USA: Addison Wesley.

Tokuda, A., Kumada, Y. & Nakagawa, K. (1970). Development and results of a trail production of 13% Cr base cast stainless steel propeller for ships. *JSW Technical Review,* 27(3), 142-152.

Tupper, B. & Boudier, T. (2009). Fourier shape analysis. Retrieved from http://imagejdocu.tudor.lu/doku.php?id=plugin:analysis:fourier_shape_analysis:start/

Veritas D. N. (2010). Pipe girth weld AUT system qualification and project specific procedure validation, *Recommended practice DNV-RP-F118,* 1-17.

Vincent, M., Nadot, Y., Nadot-Martin, C. & Dragon, A. (2016). Interaction between a surface defect and grain size under high cycle fatigue loading: Experimental approach for Armco iron. *International Journal of Fatigue,* 87, 81-90.

Wang, P., Lu, S. P., Xiao, N. M., Li, D. Z. & Li, Y. Y. (2010). Effect of delta ferrite on impact properties of low carbon 13Cr–4Ni martensitic stainless steel. *Materials Science and Engineering A,* 527, 3210-3216.

Wang, Q. G., Apelian, D. & Lados, D. A. (2001). Fatigue behavior of A356-T6 aluminum cast alloys. Part I. Effect of casting defects. *Journal of Light Metals,* 1, 73-84.

Wang, Q. G. & Jones, P. E. (2007). Prediction of Fatigue Performance in Aluminum Shape Castings Containing Defects. *Metallurgical and Materials Transactions B,* 38B, 615-621.

Yang, Z., Kang, J. & Wilkinson, D. S. (2015). Characterization of Pore Defects and Fatigue Cracks in Die Cast AM60 Using 3D X-ray Computed Tomography. *Metallurgical and Materials Transactions B,* 46B, 1576-1585.

Yi, J. Z., Gao, Y. X., Lee, P. D., Flower, H. M. & Lindley, T. C. (2003). Scatter in Fatigue Life Due to Effects of Porosity in Cast A356-T6 Aluminum-Silicon Alloys. *Metallurgical and Materials Transactions A,* 34A, 1879-1890.

Zhang, W., Liu, H., Wang, Q. & He, J. (2017). A Fatigue Life Prediction Method Based on Strain Intensity Factor. *Materials,* 10(7): 689, 1-14.

Zhu, X., Yi, J. Z. Jones, J. W. & Allison, J. E. (2007). A Probabilistic Model of Fatigue Strength Controlled by Porosity Population in a 319-Type Cast Aluminum Alloy: Part I. Model Development. *Metallurgical and Materials Transactions A,* 38A, 1111-1122.